Hafssaa Latioui

Light Tunneling, Topological Effects and Light-Matter Interactions in Wire Metamaterials

UNIVERSIDADE D COIMBRA

UNIVERSIDADE D
COIMBRA

Hafssaa Latioui

Light Tunneling, Topological Effects and Light-Matter Interactions in Wire Metamaterials

VOLUME 1

Tese no âmbito do doutoramento em Engenharia Electrotécnica e de Computadores, especialidade de Telecomunicações, orientada pelo Professor Doutor Mário Gonçalo Mestre Veríssimo Silveirinha e apresentada ao Departamento de Engenharia Electrotécnica e de Computadores da Faculdade de Ciências e Tecnologia da Universidade de Coimbra.

Outubro de 2018

Dedications

I dedicate this work

to my very dear Father and to the flower of my life: my sweet and adorable Mother,

For the flawless love they have for me
For everything they devoted to me and still devote

Thank you for your prayers and encouragement.

May God keep you healthy.

to my brothers Ahmed and Abdelilah, and my beautiful sister Meriem,

For their support and affection

I love you very much.

to my family.

to all my friends.

to all who have lighted my way.

Acknowledgement

Thanks to God for blessing me, always giving me the full strength to go forward and surround me with people whose love balance me out and just make me happy.

The past four years, building up my PhD thesis, has been a fascinating journey of my study abroad, which could not have been fulfilled without the support of admirable people that I would like to seize the chance to address them my warm thanks.

First and foremost, I would like to express my very deepest heartful gratitude to my supervisor Professor Mário Silveirinha for his extraordinary guidance and endlessly support. I feel extremely fortunate to be a PhD student of such a great and exceptional person. His genius, precious expertise and passion in his research domain give me strong motivation into this work! Professor, you have fully supported me and always had patient and super guidance and enthusiastic encouragement, I'm GREATLY THANKFUL to you for all my life!

I would also like to take this opportunity to thank the ERASMUS MUNDUS programme of the European Union – Al-Idrisi II for giving me the opportunity to study abroad, and to acknowledge their financial support during my three first years of PhD.

I would love to express my very profound gratitude to my Very Beloved Parents, Brothers, Sister, Family and Closed Friends for their absolute love and their encouragement. This accomplishment would have never been possible without your continuous support and encouragement! I UNBELIEVABLY LOVE YOU. The hardest part about my studying abroad was to live far from you my Parents.

I would like to express my warm gratitude to Tiago Morgado. He was like a co-supervisor during my first year of PhD, where he helped me very much with the first journal paper. Professor, you know what makes me more feel very grateful to you is that whenever I asked your help you were ready to help. I would like also to thank very much David for all his help during my first year of PhD where he particularly facilitate my integration. My warm thanks go also to Sylvain. Thank you all specially for the lunch times we shared.

I take advantage of these few lines to say thank you to the Department of Electrical and Computer Engineering of the University of Coimbra in its professoral and academic body for the quality of education and for the great comfortable investigation atmosphere. I would like to warmly thank Professor Henrique Silva with whom I took two doctoral classes during my first year of PhD that were very benefical for me.

Thank you to the members of the jury for honoring me by their presence and for their appreciation to evaluate this work.

I can not end this thanks without expressing my gratitude to all those who, from near or far, have contributed to the success of this work.

Abstract

The electromagnetic properties of naturally occurring materials do not always provide enough flexibility to obtain a desired electromagnetic response. The development of metamaterials has surpassed this limitation and opened the door to independently control and access new and exotic electromagnetic properties and functionalities, not directly available in Nature, relying on subwavelength artificial "atoms". The idea of expanding the properties-spectrum of natural materials crafting artificial matter versions was put forward by V. G. Veselago in 1967, and since then the research field of "metamaterials" has dramatically evolved. New materials have emerged from this research field exhibiting extraordinary optical properties, such as negative refraction and optical magnetism. They are being exploited for a broad range of applications, spanning telecommunications, sensing and biomedicine, photovoltaics and solar cells, amongst others, over different frequency domains. Among the variety of media belonging to the class of metamaterials, a subclass has attracted significant attention due to its unique potentials in the manipulation of electromagnetic fields: "wire metamaterials". In their simplest version, such materials are formed by optically dense arrays of aligned metal rods embedded into a dielectric host matrix.

Through a combination of analytical modeling and numerical simulation, the main objective of this thesis is to investigate novel wave phenomena in wire metamaterial based platforms, as well as their prospective applications. The thesis focuses on four different problems/effects: (i) the subwavelength imaging and near-field transport by a multi-wire endoscope; it is shown that

a wire medium endoscope can be quite robust to the effect of bending and allow for the near field transport with a deeply subwavelength resolution provided the total length of the bent wires satisfies the Fabry-Pérot condition. (ii) It describes a novel counterintuitive phenomenon of an anomalous light tunneling by two interlaced wire meshes; this effect is due to the destructive interference of the scattering by the two interlaced 3D wire meshes, which leads to a Fano-type resonance. (iii) It unveils a transparency effect with a topological origin; a mixture of two topologically distinct material phases, for example a metamaterial formed by metallic wire grid embedded in a magnetized plasma, may be “transparent” to electromagnetic waves in a spectral range wherein the individual material phases are strongly reflecting. (iv) It reports a mechanism to have exotic optical manipulations and lateral (recoil) forces on small particles placed nearby a reciprocal translation invariant substrate. The problems analyzed here can have applications in medical imaging, angular filtering and sensing, and in optical sorting and particle delivery.

Keywords

Metamaterials, Wire Metamaterials, Multi-wire endoscope, Spatial dispersion, Extreme anisotropy, FP resonance, Subwavelength imaging, Interlaced wire meshes, Light tunneling anomaly, Fano-resonance, Gyrotropy, Nonreciprocity, Topological material, Reciprocity theorem, Optical force, Lateral force.

Resumo

As propriedades eletromagnéticas dos materiais existentes na natureza nem sempre oferecem a flexibilidade suficiente para se obter uma resposta electromagnética desejada. O desenvolvimento dos metamateriais superou essa limitação e abriu a porta a novas e por vezes exóticas propriedades electromagnéticas, não diretamente disponíveis na Natureza. A ideia de expandir o espectro das propriedades de materiais naturais criando versões artificiais foi proposta por V. G. Veselago em 1967, e desde então o campo de investigação dos "metamateriais" evoluiu drasticamente. Novos materiais emergiram deste campo de pesquisa exibindo propriedades ópticas extraordinárias, como refracção negativa e magnetismo óptico. Estes materiais têm sido explorados para uma vasta gama de aplicações, abrangendo, entre outras, telecomunicações, sensores e biomedicina, células solares e fotovoltaicas, em diferentes domínios de frequência. Entre a variedade de estruturas pertencentes à classe dos metamateriais, uma subclasse tem atraído atenção significativa devido ao seu potencial único na manipulação de campos electromagnéticos: os metamateriais de fios metálicos (*wire metamaterials*). Na sua versão mais simples, tais materiais são formados por um agregado opticamente denso de fios metálicos alinhados embedidos num material dieléctrico.

Através de uma combinação de modelagem analítica e simulação numérica, o objetivo principal desta tese é investigar novos fenómenos ondulatórios em plataformas baseadas em *wire metamaterials*, bem como suas potenciais aplicações. A tese tem como foco quatro problemas/efeitos diferentes: (i) "imaging" sub-λ (λ representa o comprimento de onda) e o transporte de campo próximo por um endoscópio formado por um agregado de fios metálicos;

é mostrado que um endoscópio formado por um “wire medium” pode ser bastante robusto a flexões e permite o transporte de campo próximo com uma resolução profundamente sub-comprimento de onda, desde que o comprimento total dos fios dobrados satisfaça a condição de Fabry-Pérot. (ii) Descreve um novo fenómeno contra-intuitivo de tunelamento anómalo da luz por duas redes de fios metálicos entrelaçadas; este efeito é devido à interferência destrutiva da difusão da luz pelas duas redes de fios 3D entrelaçadas, que conduz a uma ressonância do tipo Fano. (iii) Revela um efeito de transparência com uma origem topológica; uma mistura de duas fases topologicamente distintas, por exemplo, um metamaterial formado por um grelhas metálicas embedidas num plasma magnetizado, pode ser “transparente” à propagação de ondas electromagnéticas numa gama espectral onde as fases individuais do material são fortemente reflectoras. (iv) Relata um mecanismo para ter manipulações ópticas exóticas e forças laterais em pequenas partículas colocadas na proximidade de um substrato recíproco invariante para translações. Os problemas analisados na tese têm potenciais aplicações em imagiologia médica, em sensores, e na separação/entrega óptica de partículas.

Palavras-chave

Metamateriais, *Wire Metamaterials*, Endoscópio *Multi-wire*, Dispersão Espacial, Anisotropia Extrema, Ressonância FP, *Imaging* sub-λ, Redes metálicas entrelaçadas, Anomalia de tunelamento da luz, Ressonância Fano, Girotropia, Não reciprocidade, Material topológico, Teorema da reciprocidade, Força óptica, Força lateral.

Preface

This dissertation is the result of work carried out under the supervision of Professor Mário Silveirinha, at Instituto de Telecomunicações – Coimbra and Department of Electrical and Computer Engineering of the Faculty of Sciences and Technology of the University of Coimbra between September 2014 and September 2018. The originality of this thesis is sustained in a series of journal and conference papers that have been published while I was studying for my PhD. Except where explicit reference is made to the work of others, the work contained in this dissertation is my own.

List of Symbols

j	Imaginary unit $\sqrt{-1}$
i	Imaginary unit $\sqrt{-1}$
ω	Angular frequency
t	Time
$\overline{\varepsilon}$	Permittivity tensor
c	Speed of light in vacuum
ε_0	Permittivity of space
ε_h	Relative permittivity of the dielectric host
k_0	Wave number in free space
k_h	Wave number in the dielectric host
k_p	Plasma wave number
γ_0	Free-space propagation constant
η_0	Impedance of free space
η_h	Intrinsic impedance of the host medium
λ_0	Wavelength in free-space
l_0	Dimensionless slow wave factor
ω_p	Plasma frequency
k	Wave number
a	Lattice period
r	Wire radius
θ^{inc}	Incidence angle
$\left(k_x, k_y, k_z\right)$	Components of the wave vector
$\left(x, y, z\right)$	Cartesian position coordinates
$\left(\hat{\mathbf{u}}_x, \hat{\mathbf{u}}_y, \hat{\mathbf{u}}_z\right)$ $\left(\hat{\mathbf{x}}, \hat{\mathbf{y}}, \hat{\mathbf{z}}\right)$	Unity vectors
$\mathbf{k}$	Wave vector
$\mathbf{k}^{inc}$	Incident wave vector
$\mathbf{k}_{\|\|}$	Transverse wave vector
$\mathbf{E}$	Electric field vector
$\mathbf{H}$	Magnetic field vector
$\mathbf{J}_c$	Averaged electric current density
T	Transmission coefficient
R	Reflection coefficient
$\mathbf{E}^{TM,TEM}$	The electric field associated with a TM (TEM) plane wave
$\mathbf{H}^{TM,TEM}$	The magnetic field associated with a TM (TEM) plane wave
$\varepsilon_{m,i}$	The relative permittivity of the metal for the *i*-th wire mesh

$r_{w,i}$	The radii of the wires for mesh *i*
$k_{p,i}$	Plasma wave number of wire mesh *i*
$\omega_{p,ef}$	The effective plasma frequency
$\varepsilon_t(\omega)$	Transverse permittivity
$\varepsilon_l(\omega)$	Longitudinal permittivity
$\varepsilon_{t,i}(\omega)$	Transverse permittivity of *i*-th wire mesh
σ_i	Conductivity of wire mesh *i*
δ_i	Skin depth of the metal for the *i*-th wire mesh
$\mathbf{1}$	3x3 unity matrix
$\mathbf{1}_t$	3x3 transverse unity matrix
$\mathbf{B}_0$	Bias magnetic field
ω_c	Cyclotron frequency
ε_{ef}	The equivalent permittivity of a gyrotropic material
γ_g	Propagation constant in the gyrotropic medium
Γ	Plasma collision frequency
ω_{pe}	The plasma frequency for electrons
ω_{ph}	The plasma frequency for holes
ω_{ce}	The cyclotron frequency for electrons
ω_{ch}	The cyclotron frequency for holes
ε_s	Static permittivity
m_e^*	The effective masses of electrons
m_h^*	The effective masses of holes
n	Concentration of electrons/holes
$\mathbf{p}_e$	Electric dipole moment
$\mathbf{p}_m$	Magnetic dipole moment
$\mathbf{E}^{inc}$	The incident electric field
$\mathbf{E}^s$	The “scattered” electric field
Φ_0	The Hertz potential
$\mathbf{E}_t^{inc}$	Transverse incident electric field
$\mathbf{E}_t^s$	Transverse “scattered” electric field
$\mathbf{R}(\omega, k_x, k_y)$	Reflection matrix for the electric field
$\mathbf{R}^H(\omega, k_x, k_y)$	Reflection matrix for the magnetic field
$\mathbf{k}_{\|}, \mathbf{k}_t$	Transverse wave vector
$\mathbf{C}_{\text{int}}$	Interaction coefficient tensor

$\mathscr{F}_i$	Time-averaged force acting on the dipole along the *i*-th direction
$\mathscr{F}_0$	Normalizing factor with units of force
$\mathbf{Y}^{\pm}$	Admittance matrices (plane waves propagating along the $\pm z$)
α_0	Tilt angle of the optical axis
α_e	Tilt angle of the electric dipole moment
α_m	Tilt angle of the magnetic dipole moment
θ_e	Phase of the electric dipole
θ_m	Phase of the magnetic dipole

List of Mathematical Notations

$\lfloor\ \rfloor$	Jump discontinuity across the interface
$\cdot$	Dot product
$\times$	Cross product
$\otimes$	Tensor product
$\lvert\ \rvert$	Absolute value
∇	The Gradient operator
∂_i	Partial derivative with respect to *i*
*	Complex conjugate

List of figures

Contents

CHAPTER 1 : General Introduction

I. General Introduction

I.1 Background - Literature Overview

Research in advanced materials is a cutting-edge topic driving modern technologies forward. Understanding and manipulating the electromagnetic material response can have a significant impact across a multitude of disciplines and lead to applications over the whole frequency spectrum including telecommunication networks, and imaging and sensing systems.

Over the last decades, the technological progress in several different areas has placed challenging demands related to the electromagnetic properties of materials. Crucially, the palette of materials directly available in Nature does not always provide enough flexibility to obtain the desired electromagnetic response. Motivated by the continuous development in nanotechnology and nanoscience, the answer to this limitation arrived in the form of artificial structured media. Specifically, a recent development in material science goes by the name of metamaterials, which consist of dielectric or metallic inclusions properly tailored in shape and size and arranged in a regular lattice.

This new type of artificial composite media with exotic material properties gives us a way to control waves almost arbitrarily. Indeed, electromagnetic metamaterials can be designed to interact with light in specific ways; the bulk optical electromagnetic properties of metamaterials depend not only on the composition but mainly on underlying geometric resonances and near-field coupling between the invented subwavelength building blocks [1]. Since their first realization, these nanostructured media have received increasing attention and have led to

novel devices with capabilities beyond the ordinary across much of the electromagnetic spectrum.

Over the past decade, metamaterial technologies have matured to enable a number of unusual phenomena such as negative refractive index [2], optical magnetism [3], giant chirality [4–6], near zero parameters [7], bianisotropy [8], and strong spatial dispersion [9]. The metamaterial technology led to the realization of a wide range of novel microwave devices including antennas [10,11], phase-shifters [12], couplers [13], broadband compact power-dividers [14], with peculiar electromagnetic properties.

An important and broad class of artificial electromagnetic materials attracting considerable attention are the wire metamaterials; they consist of dense arrays of metallic wires embedded within an isotropic dielectric host [15-25]. The high optical contrast between the metal and the dielectric and the wires geometry (the wires are typically long and thin in terms of the wavelength) lead to the unusual properties of wire metamaterials: extreme optical anisotropy and strong spatial dispersion [26-27]. Wire metamaterials can have important applications at microwave, terahertz, and optical frequencies [15, 25, 27-39]. Most importantly, wire metamaterials allow us to transport and manipulate a complex near-field distribution with deeply subwavelength details from microwaves up to the mid-infrared range. Other interesting applications are the realization of high-impedance surfaces, the suppression of guided modes to reduce the mutual coupling in printed antenna arrays, the design of ultra-compact waveguides, waveguiding with no conductive contact between the metal pieces, in magnetic resonance imaging (MRI), and in the correction of chromatic aberrations, just to name a few.

Moreover, wire arrays have, in general, an hyperbolic-type dispersion in the infrared domain, which opens a number of opportunities in terms of light-matter interactions; for example, a strong enhancement of the Purcell factor [28], a giant near-field radiative heat transfer [29-30], or an ultra-strong and ultra-broadband Cherenkov emission [31-32]. A hyperbolic-type response also enables a negative refraction effect which has applications in light focusing with flat lenses [33-34].

Research on wire metamaterials has majestically unveiled novel physical effects and applications. In this thesis, I demonstrate how wire metamaterials can be used in medical imaging [37], light tunneling, angular filtering and sensing [38], topological phase transitions [39], and unusual optical manipulations of nano-particles. The relevant electromagnetic problems are thoroughly analyzed and discussed from a theoretical perspective using analytical models, and subsequently, numerically validated.

I.2 Significance And Thesis Statement

The study of wire metamaterials has a long history. Significant progress in the study of this special class of metamaterials has been achieved during the last decade. Wire metamaterials are recognized to be very promising in view of their rather simple fabrication technologies. In this thesis, I aim to contribute to and build on the vast existing literature and study new exotic phenomena in wire media and their prospective applications.

The dissertation mainly focuses on answering four open problems, which I will motivate with four questions. The first one refers to the wire-medium lens and is as follows: has a multi-

wire endoscope a good tolerance to the internal bending/disruption effects so that it can be used in sub-wavelength imaging applications, in particular in medical endoscopy?. The second problem concerns three-dimensional connected metallic wire metamaterials. These structures are typically completely opaque to light propagation and have an electromagnetic response analogous to that of a free-electron gas. Does more metal lead to stronger reflections? By investigating the electromagnetic response of two interlaced wire networks, I find that it may enable a surprising tunneling effect that may have application in sensing and angular filtering. The third question is as follows: does any interesting effect arise when two topologically different materials are combined to form a metamaterial? I show that by mixing two distinct topological material phases it is possible to create unusual conditions for wave propagation in a spectral range wherein the two phases are impenetrable by light. I propose a metamaterial realization of the studied system based on a wire medium. The last problem is related to the optical manipulation of small particles above a smooth substrate. Can we take advantage of the anisotropy or bianisotropy of a reciprocal substrate to obtain a nontrivial optical lateral force? Surprisingly, I find that for linearly-polarized electric dipoles the optical lateral force invariably vanishes, independent of the anisotropy (e.g., tilted optical axes) or chirality of the substrate. I propose a new mechanism to have non-trivial lateral forces on linearly-polarized particles with nontrivial electric and magnetic responses, standing above a tilted wire medium.

I.3 Organization of the Thesis

The thesis is organized into 6 main chapters, with the first one being this introduction. Next, I briefly describe the contents of the remaining chapters.

In the second chapter, an application of wire media for medical imaging is proposed: the multi-wire endoscope. In order to provide sufficient elementary background to this study, I begin by introducing the near-field imaging using wire media and I review the wire media homogenization model. I then study the transmission and reflection properties of the bent wire medium lens for different possible interconnections and bending angles scenarios. Moreover, I perform full wave simulations confirming and validating the potentials in near-field transport of the investigated multiwire endoscope.

In chapter III, I propose an application of wire-media for sensing and angular filtering: the interlaced wire meshes. I start the chapter by discussing the electromagnetic response of the elementary single 3D wire mesh, highlighting that it is analogous to that of a free-electron gas. Then I numerically investigate the coupling between two wire meshes and find that it may lead to the emergence of a longitudinal propagating state in the low frequency limit that can be excited by an incoming plane wave. Then I develop a theoretical model for the wave scattering problem by two interlaced wire meshes taking into account plasmonic and loss effects. Counterintuively, I find that by interlacing the two wire meshes it is possible to “tunnel” light through the wire medium. It is shown that the physical origin of the light tunneling anomaly is a sub-radiant Fano-type resonance that enables the *cancellation of the scattering* by the two interlaced wire mediums. The effect is also explained with an effective medium theory that models the interlaced wire medium as a spatially dispersive continuum.

In Chapter IV, I predict an anomalous “transparency effect” in a composite material formed by two topologically distinct fully-reflecting phases. I propose a realistic physical

implementation of the suggested system relying on the metamaterial concept. First, I briefly introduce some fundamental and basic concepts used in this chapter. After this, I introduce the proposed two phase topological metamaterial. Then, I examine the transmission properties of the proposed topological metamaterial and demonstrate that it is characterized by a low-frequency transparency window in a spectral range wherein the two phases are strongly reflecting. I craft a novel composite material, a metallic wire grid embedded in a magnetized plasma, to implement the suggested structure. Detailed numerical simulations confirm that the proposed system enables an anomalous wave tunneling at extremely low frequencies. It is also argued that some natural materials, such as semiconductors, may enable similar effects.

In chapter V, I theoretically study the lateral (recoil) forces acting on generic dipole type particles nearby a reciprocal translation-invariant substrate. I start by proving that, surprisingly, reciprocity forbids optical lateral forces when the particle is a single linearly polarized atom independent of the anisotropy or bianisotropy of the substrate. I propose a novel mechanism to obtain lateral recoil forces using magneto-electric dipolar emitters above a uniaxial dielectric half-space with tilted optical axes, e.g. a tilted wire medium.

Finally, the main conclusions about the thesis achievements are recapitulated in the final chapter.

I.4 Main Contributions/Thesis by Publications

I.4.1 Journal Publications

[J1] Hafssaa Latioui and Mário G. Silveirinha, “Near-field transport by a bent multi-wire endoscope”, *J. Appl. Phys.*, **120**, 063103, 2016.

[J2] Hafssaa Latioui and Mário G. Silveirinha, "Light tunneling anomaly in interlaced wire meshes", *Phys. Rev. B*, **96**, 195132, 2017.

[J3] Hafssaa Latioui and Mário G. Silveirinha, "Topologically induced transparency in a two-phase metamaterial", *Appl. Phys. Lett.*, **113**, 131106, 2018.

[J4] Hafssaa Latioui and Mário G. Silveirinha, "Lateral optical forces on linearly-polarized emitters near a reciprocal substrate", (submitted, Oct. 2018).

I.4.2 Conference Proceeding Publications

[C1] Hafssaa Latioui, Mário G. Silveirinha, "Multi-wire endoscopes for near-field transport", *4th Annual Conference of COST Action MP1204 & SMMO2016 Conference*, March 21-24, 2016, Lisbon – Portugal (with oral presentation).

[C2] Hafssaa Latioui, Mário G. Silveirinha, "Anomalous light tunneling through two interlaced 3D metallic wire meshes", *The 7th International Conference on Metamaterials, Photonic Crystals and Plasmonics, META'16*, July 25-28, 2016, Malaga (Invited talk).

[C3] Hafssaa Latioui, Mário G. Silveirinha, "Electromagnetic "Transparency" in a material with two distinct topological phases", *11.^{o} Congresso do Comité Português da URSI,* November 24, 2017, Lisbon – Portugal (with oral presentation). With second place best student paper award.

[C4] Hafssaa Latioui, Mário G. Silveirinha, ""Electromagnetic transparency" in a two-phase topological material", *XII Iberian Meeting on Computational Electromagnetics 2018*, May 18, 2018, Coimbra – Portugal (with oral presentation).

[C5] Hafssaa Latioui, Mário G. Silveirinha, "Lateral optical forces on linearly-polarized emitters near a reciprocal substrate", *12th International Congress on Artificial Materials for Novel Wave*

Phenomena – Metamaterials 2018, Aug. 27th – Sept. 1st, 2018, Espoo, Finland. 2º prize of the student paper competition.

Awards

Hafssaa Latioui, Mário G. Silveirinha, "Electromagnetic "Transparency" in a material with two distinct topological phases", "The second place best student paper award", *11.º Congresso do Comité Português da URSI,* November 24, 2017, Lisbon, Portugal.

Hafssaa Latioui, Mário G. Silveirinha, "Lateral optical forces on linearly-polarized emitters near a reciprocal substrate", "The 2º prize of the student paper competition", *12th International Congress on Artificial Materials for Novel Wave Phenomena – Metamaterials 2018*, Aug. 27th – Sept. 1st, 2018, Espoo, Finland.

References

[1] V. M. Shalaev, "Optical negative-index metamaterials", *Nature Photon*, **1**, 41–48, 2007.

[2] W. Cai and V. Shalaev, "Optical Metamaterials: Fundamentals and Applications", Springer, 2009.

[3] W. Cai, U. K. Chettiar, H. K. Yuan et al., "Metamagnetics with rainbow colors", *Optics Express*, **15**, 3333–3341, 2007.

[4] N. Liu, H. Liu, S. Zhu, and H. Giessen, "Stereometamaterials", *Nature Photonics*, **3**, 157–162, 2009.

[5] E. Plum, X. X. Liu, V. A. Fedotov, Y. Chen, D. P. Tsai, and N. I. Zheludev, "Metamaterials: optical activity without chirality", *Phys. Rev. Lett.*, **102**, 113902, 2009.

[6] E. Plum, V. A. Fedotov, A. S. Schwanecke, N. I. Zheludev, and Y. Chen, "Giant optical gyrotropy due to electromagnetic coupling", *Appl. Phys. Lett.*, **90**, 223113, 2007.

[7] A. Alù, M. G. Silveirinha, A. Salandrino, and N. Engheta, "Epsilon-near-zero metamaterials and electromagnetic sources: tailoring the radiation phase pattern", *Phys. Rev. B*, **75**, 155410, 2007.

[8] X. Chen, B. I. Wu, J. A. Kong, and T. M. Grzegorczyk, "Retrieval of the effective constitutive parameters of bianisotropic metamaterials", *Phys. Rev. E*, **71**, 046610, 2005.

[9] J. Elser, V. A. Podolskiy, I. Salakhutdinov, and I. Avrutsky, "Nonlocal effects in effective-medium

response of nanolayered metamaterials", *Appl. Phys. Lett.*, **90**, 191109, 2007.

[10] C. Caloz, T. Itoh, "Novel microwave devices and structures based on the transmission line approach of meta-materials", *IEEE MTT-S International Microw. Symposium Digest*, **1**, 195-198, 2003.

[11] F. Qureshi, M. Antoniades, G.V. Eleftheriades, "A compact and low-profile metamaterial ring antenna with vertical polarization", *IEEE Antenna Wireless Prop. Lett.*, **4**, 333-336, 2005.

[12] M. Antoniades, G.V. Eleftheriades, "Compact linear lead/lag metamaterial phase shifters for broadband applications", *IEEE Antennas Wireless Propagation Lett.*, **2,** 103-106, 2003.

[13] C. Caloz, A. Sanada, T. Itoh, "A novel composite right-/left-handed coupled-line directional coupler with arbitrary coupling level and broad bandwidth", *IEEE Trans. Microwave Theory Techniques*, **52**, 980-992, 2004.

[14] M. Antoniades, G.V. Eleftheriades, "A broadband series power divider using zero-degree metamaterial phase-shifting lines", *IEEE Microwave Guided Wave Lett.,* **15**, 808-810, 2005.

[15] W. Rotman, "Plasma simulation by artificial dielectrics and parallel-plate media", *IRE Trans. Antennas Propag.*, **10**, 82-95, 1962.

[16] J. B. Pendry, A.J. Holden, W. J. Stewart, and I. Youngs, "Extremely low frequency plasmons in metallic mesostructures", *Phys. Rev. Lett.*, **76**, 4773-4776 , 1996.

[17] S. I. Maslovski, S. A. Tretyakov, and P. A. Belov, "Wire media with negative effective permittivity: A quasistatic model", *Microwave Opt. Technol. Lett.*, **35**, 47-51, October, 2002.

[18] P. A. Belov, R. Marqués, S. I. Maslovski, I. S. Nefedov, M. Silveirinha, C. R. Simovsky and S. A. Tretyakov, "Strong spatial dispersion in wire media in the very large wavelength limit," *Phys. Rev. B*, **67**, 113103, 2003.

[19] M. G. Silveirinha, C. A. Fernandes, "Homogenization of 3D- Connected and Non-Connected Wire Metamaterials", *IEEE Trans. on Microwave Theory and Tech.*, **53**, p. 1418 - 1430, 2005.

[20] M. G. Silveirinha, "Nonlocal homogenization model for a periodic array of epsilon-negative rods", *Phys. Rev. E*, **73**, 046612, 2006.

[21] S. I. Maslovski, M. G. Silveirinha, "Nonlocal permittivity from a quasistatic model for a class of wire media", *Phys. Rev. B*, **80**, 245101, 2009.

[22] M. G. Silveirinha, C. A. Fernandes, "Nonresonant structured material with extreme effective parameters", *Phys. Rev. B*, **78**, 033108(1-4), 2008.

[23] M. G. Silveirinha, "Artificial plasma formed by connected metallic wires at infrared frequencies", *Phys. Rev. B*, **79**, 035118(1-15), 2009.

[24] G. W. Hanson, E. Forati, and M. G. Silveirinha, "Modeling of spatially-dispersive wire media: transport representation, comparison with natural materials, and additional boundary

conditions", *IEEE Trans. on Antennas and Propagat.*, **60**, 4219, 2012.

[25] E. Forati, G. W. Hanson, "Scattering from Isotropic Connected Wire Medium Metamaterials: Three-, Two-, and One-Dimensional Cases", *IEEE Trans. on Antennas and Propagation*, **61**, 3564-3574, 2013.

[26] C. R. Simovski, P. A. Belov, A. V. Atrashchenko, Y. S. Kivshar, "Wire metamaterials: physics and applications", *Adv. Mater.*, **24**, 4229-4248, 2012.

[27] P. A. Belov, Y. Hao and S. Sudhakaran, "Subwavelength microwave imaging using an array of parallel conducting wires as a lens", *Phys. Rev. B*, **73** 033108, 2006.

[28] P. A. Belov and M. G. Silveirinha, "Resolution of subwavelength transmission devices formed by a wire medium", *Phys. Rev. E*, **73**, 056607, 2006.

[29] P. Ikonen, C. Simovski, S. Tretyakov, P. Belov P and Y. Hao, "Magnification of subwavelength field distributions at microwave frequencies using a wire medium slab operating in the canalization regime", *Appl. Phys. Lett.*, **91**, 104102, 2007.

[30] P. A. Belov, G. K. Palikaras, Y. Zhao, A. Rahman, C. R. Simovski, Y. Hao and C. Parini, "Experimental demonstration of multiwire endoscopes capable of manipulating near-fields with subwavelength resolution", *Appl. Phys. Lett.*, **97**, 191905, 2010.

[31] G. Shvets, S. Trendafilov, J. B. Pendry, A. Sarychev, "Guiding, Focusing, and Sensing on the Subwavelength Scale Using Metallic Wire Arrays", *Phys. Rev. Lett.*, **99**, 053903, 2007.

[32] P. A. Belov, Y. Zhao, S. Tse, P. Ikonen, M. G. Silveirinha, C. R. Simovski, S. Tretyakov, Y. Hao, and C. Parini, "Transmission of images with subwavelength resolution to distances of several wavelengths in the microwave range", *Phys. Rev. B*, **77**, 193108, 2008.

[33] M. G. Silveirinha, P. A. Belov, and C. R. Simovski, "Subwavelength imaging at infrared frequencies using an array of metallic nanorods", *Phys. Rev. B*, **75**, 035108, 2007.

[34] M. G. Silveirinha, P. A. Belov and C. R. Simovski, "Ultimate limit of resolution of subwavelength imaging devices formed by metallic rods", *Opt. Lett.*, **33,** 1726, 2008.

[35] T. A. Morgado, J. S. Marcos, M. G. Silveirinha, S. I. Maslovski, "Experimental verification of full reconstruction of the near-field with a metamaterial lens", *Appl. Phys. Lett.* **97**, 144102, 2010.

[36] B. D. F. Casse , W. T. Lu , Y. J. Huang , E. Gultepe , L. Menon , S. Sridhar, "Super-resolution imaging using a three-dimensional metamaterials nanolens", *Appl. Phys. Lett.*, **96** , 023114, 2010.

[37] H. Latioui and M. G. Silveirinha, "Near-field transport by a bent multi-wire endoscope", *J. Appl. Phys.*, **120**, 063103, 2016.

[38] H. Latioui and M. G. Silveirinha, "Light tunneling anomaly in interlaced wire meshes", *Phys. Rev. B*, **96**, 195132, 2017.

[39] H. Latioui and M. G. Silveirinha, “Topologically induced transparency in a two-phase metamaterial”, *Appl. Phys. Lett.*, **113**, 131106, 2018.

CHAPTER 2 :

Application of Multi-Wire Endoscopes for Medical Imaging

II. Application of Multi-Wire Endoscopes for Medical Imaging

II.1 Introduction

As discussed in the general introduction, WM has a long history and many significant achievements in its study were made in the recent years. One of the interesting proposals related to the uniaxial wire medium is the use of this artificial material to make multi-wire endoscopes for subwavelength imaging, light concentration, magnification and demagnification [1-3]. Such multi-wire endoscopes can have many applications, for instance, it has been suggested that in the microwave range tapered wire medium endoscopes may be useful to improve the performance of MRI systems [4], and more generally in medical endoscopy. For such applications, it is essential that the endoscope is flexible so that it can be used to examine the interior of a body cavity. With this motivation in mind, we investigate next the impact of bending and the effect of an internal disruption of a multi-wire endoscope in sub-wavelength imaging applications. Has the endoscope a good tolerance to the bending/disruption effects or will these deformations distort significantly the transported image?

A realistic multi-wire endoscope is formed by a finite array of metallic wires. Because such a configuration does not enable an analytical treatment, first we consider a simplified model wherein the number of wires is infinite and the structure is periodic. Moreover, we suppose that the endoscope is bent only at a single plane. At the bending points, the wires can be either connected or disconnected (the rupture case). The study is based on the effective-medium model (EMM) of wire media which takes into account the spatial dispersion effects and requires additional boundary conditions (ABC) on all interfaces. The analytical methods previously

developed to characterize the wave propagation in wire media are extended here to the case in which two distinct wire arrays meet at different angles. We develop an analytical spatially dispersive model to characterize the scattering by a bent wire medium slab and derive novel additional boundary conditions to describe the behavior of the macroscopic electromagnetic fields at the interface of two tilted wire mediums for arbitrary tilt angles and arbitrary lengths of wires in both media. We discuss in detail the conditions required to achieve a nearly perfect image transport using a bent wire medium lens, and discuss the importance of ensuring that the wires remain unbroken at the points wherein they are bent. Our analytical theory is successfully validated with full-wave numerical simulations.

The chapter is organized as follows. In section II.2, we briefly introduce the near field imaging with wire media. In section II.3 the homogenization approach used to model the wave scattering by a bent wire medium slab is introduced, and the needed additional boundary conditions are derived. In section II.4, we discuss the extreme anisotropy approximation. In section II.5 the transmission and reflection properties of the bent wire medium lens are examined for different interconnections and bending angles, using both the theoretical and full-wave simulations. In section II.6, we present full wave simulations that illustrate the potentials of bent multi-wire endoscopes in imaging applications. The conclusions are drawn in section II.7. The electromagnetic fields are assumed monochromatic with a time dependence of the form $e^{j\omega t}$.

II.2 Near Field Imaging with Wire Media – Canalization regime

One of the key applications of wire media (WM) is in subwavelength imaging, particularly in

the realization of imaging devices that produce flawless images. Conventional lenses cannot provide resolution better than half of the wavelength of radiation, and hence features smaller than half-wavelength are invariably lost in the image (diffraction limit). Indeed, typical lenses operate only with the far-field of the source, which is formed by propagating spatial harmonics. The information related to the near field (subwavelength details) of the source is transported by evanescent spatial harmonics, which exhibit exponential decay in all natural materials as well as in free space. Recently, several techniques have been put forward to realize imaging with super-resolution in different ranges of the electromagnetic spectrum. The most significant and promising approaches include perfect lenses [7], hyperlenses, restoring the near field image of the object without the far-field [8-11], and stimulated emission depletion fluorescence microscopes [12]. Another option is based on the use of wire media, which may be designed to transport and restore the evanescent spatial harmonics and overcome the diffraction limit. For example, it was shown in [13-16] that an array of parallel metallic wires, i.e. a bulk material with extreme optical anisotropy, may be designed to manipulate and canalize a complex near field distribution (up to terahertz frequencies) with super-resolution based on the canalization regime: the “wire medium lens”. This lens provides unique opportunities to transport the subwavelength details of the source without significant distortion to nearly unlimited distances, with good tolerance to material losses, and a fairly large bandwidth (around 15%) [17]. More recently, it was demonstrated that arrays of wires may be also used to magnify and demagnify the subwavelength details of an image [18], by tapering the array of wires with their divergent or convergent arrangement: the tapered wire medium lens.

II.3 The scattering problem

In the following, we quickly review the homogenization (effective medium model) of the simple wire medium considering the nonlocal model, which takes into account the spatial dispersion. Then, we present the analytical model to characterize the scattering by a bent wire medium slab formed by an infinite number of wires. We formulate two novel additional boundary conditions, to model the behavior of the macroscopic electromagnetic fields at the interface of two tilted wire mediums, required to solve the scattering problem.

II.3.1 Review of the Wire Medium Homogenization

The standard WM is a metamaterial formed by a regular 2D lattice of ideally thin conducting wires (small radii compared to the lattice period and the wavelength) and usually described at low frequencies as a uniaxial material whose relative permittivity dyadic can be written as,

$$\frac{\bar{\varepsilon}}{\varepsilon_0} = \varepsilon_h \left(\hat{\mathbf{u}}_x \hat{\mathbf{u}}_x + \hat{\mathbf{u}}_y \hat{\mathbf{u}}_y + \varepsilon_z \hat{\mathbf{u}}_z \hat{\mathbf{u}}_z \right) = \varepsilon_h \left(\mathbf{I}_t + \varepsilon_z \hat{\mathbf{u}}_z \hat{\mathbf{u}}_z \right) \tag{2.1}$$

where ε_h is the relative permittivity of the host medium, and the wires are directed along the *z*-direction.

The description of this medium by means of a local dispersive uniaxial dielectric tensor is not complete, leading to results that do model incorrectly the propagation of electromagnetic waves at any frequency. It was theoretically demonstrated that in the general case of oblique propagation, the axial permittivity ε_z strongly depends on the wavevector $\mathbf{k}$ even at low frequencies $\lambda \gg a$.

Spatial dispersion is a nonlocal effect that the electric polarization at a certain position is determined not only by the electric field at that position, but also by the fields in its

neighborhood [19–21]. An immediate consequence of spatial dispersion is that the permittivity of the underlying medium becomes wave vector dependent. Due to spatial dispersion, additional waves may appear in the nonlocal medium [22]. This may be understood as a consequence of extra degrees of freedom in the system, coming from the dependence of the permittivity on the wave vector. For a given frequency, there may exist two different wave vectors that satisfy the same dispersion relation. The phenomenon of wave splitting can therefore be observed in the medium [23].

The simple wire medium of PEC wires is characterized by strong *spatial dispersion* and was described by the dielectric function (2.1) with $\varepsilon_t = \varepsilon_h$ and a *nonlocal* axial component,

$$\varepsilon_z = 1 - \frac{k_p^2}{k^2 - k_z^2} \tag{2.2}$$

with $k = \omega / c\sqrt{\varepsilon_h} = \sqrt{\varepsilon_h} k_0$ is the wave number of the host medium. The constant k_p is the wave number corresponding to an equivalent "plasma frequency" ω_p that gives grounds to call the wire medium as "artificial plasma". k_z is the *z*-component of the wave vector $\mathbf{k}$. Different formulas are available for the plasma frequency, for example [24-26],

$$k_p^2 = \frac{2\pi}{a^2 \ln\left(a/\left(2\pi r\right) + 0.5275\right)} \tag{2.3}$$

For the axial propagation with $k = k_z$, the axial component of permittivity approaches infinity, physically meaning that the axially propagating waves are transverse ($E_z = H_z = 0$). Thus, wire media form a class of metamaterials that exhibit strong spatial dispersion in the very large wavelength. Strong spatial dispersion in an electrically dense wire medium appears due to the

electrically long length of the wires in the axial direction.

The most important consequences of this spatial dispersion, i.e. the dependence on $\mathbf{k}$, are the flat isofrequency contours of the transverse electromagnetic (TEM) eigenmodes. These eigenmodes propagate along the wires with a velocity equal to the speed of light in the host material. These waves are essentially transmission-line modes since, for them, the wire medium is a multiwire transmission line. Flat isofrequency contours are inherent to local uniaxial media with extreme optical anisotropy, namely media characterized by the permittivity tensor $\frac{\bar{\varepsilon}}{\varepsilon_0} = \varepsilon_h \left(\mathbf{I}_t + \infty \hat{\mathbf{u}}_z \hat{\mathbf{u}}_z \right)$.

II.3.2 Geometry

A realistic multi-wire endoscope is formed by a finite number of metallic wires. Because such a structure does not allow for an analytical analysis, first we focus on a problem wherein the number of wires is infinite and the structure is periodic. Moreover, we assume that the endoscope is bent only at a single plane. The geometry of such bent wire medium is as pictured in Fig. 2.1a. Each section of this structure consists of a rectangular lattice of parallel metallic wires oriented along a direction $\hat{\mathbf{u}}_{\alpha 1}$ ($\hat{\mathbf{u}}_{\alpha 2}$) and with length L_1 (L_2), as illustrated in Fig. 2.1b. The wires are parallel to the (*yoz)* plane, so that $\hat{\mathbf{u}}_{\alpha 1} = \sin\alpha_1 \hat{\mathbf{y}} + \cos\alpha_1 \hat{\mathbf{z}}$ and $\hat{\mathbf{u}}_{\alpha 2} = \sin\alpha_2 \hat{\mathbf{y}} + \cos\alpha_2 \hat{\mathbf{z}}$, being α_1 and α_2 the angles of each wire array with respect to the *z*-direction (note that $\alpha_2 < 0$ in Fig. 2.1b). The wires are embedded in a dielectric host with relative permittivity ε_h, have radius r_w and are spaced by the distance a along the $\hat{\mathbf{x}}$ and $\hat{\mathbf{u}}_{p2}$

directions and by the distance $\left(a/\cos(\alpha_2)\right)\cos(\alpha_1)$ along the $\hat{\mathbf{u}}_{p1}$ direction, with $\hat{\mathbf{u}}_{p,i}=\hat{\mathbf{u}}_{\alpha,i}\times\hat{\mathbf{x}}$ (i=1,2).

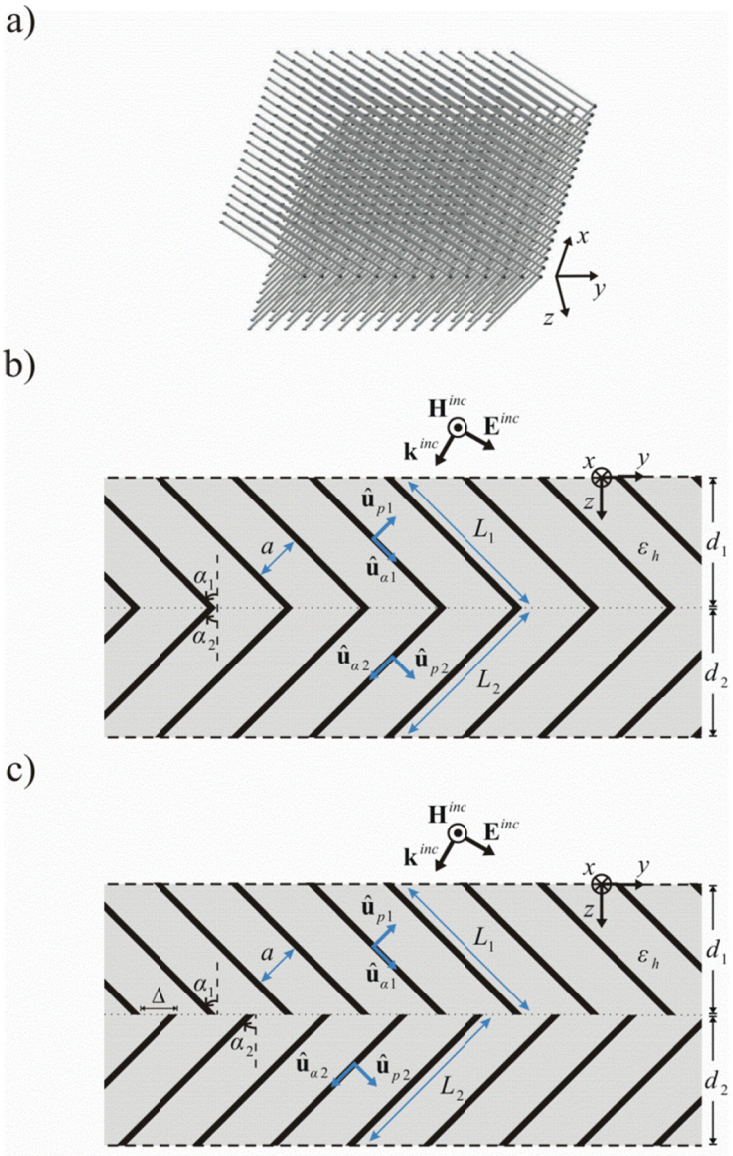

Figure 2.1: (a) Perspective view of the bent wire medium. (b) Geometry of a cut of the bent wire medium in the yoz plane. The structure is periodic along the x and y directions and has a thickness $d=d_1+d_2$. In the top region $\left(0<z<d_1\right)$, the metallic wires are spaced by a distance a and embedded in a host medium with permittivity ε_h. (c) Similar to (b) but for two misaligned and disconnected wire arrays.

The analytical model used to characterize the wave scattering by a bent wire medium builds on the theory of Refs. [27-28] for a single array of metallic wires tilted with respect to the

interface. Each wire medium region can be regarded as an effective medium characterized by the permittivity tensor [29-31],

$$\frac{\bar{\bar{\varepsilon}}}{\varepsilon_0}=\varepsilon_h\left(\hat{\mathbf{u}}_x\hat{\mathbf{u}}_x+\hat{\mathbf{u}}_p\hat{\mathbf{u}}_p+\varepsilon_{\alpha\alpha}\hat{\mathbf{u}}_\alpha\hat{\mathbf{u}}_\alpha\right)\ \text{with}\ \ \varepsilon_{\alpha\alpha}\left(\omega,k_\alpha\right)=1-\frac{\beta_p^2}{\beta_h^2-k_\alpha^2}. \tag{2.4}$$

where $\beta_h=\sqrt{\varepsilon_h}\,\dfrac{\omega}{c}$ is the wave number of the host medium, $k_\alpha=\mathbf{k}\cdot\hat{\mathbf{u}}_\alpha$ is the projection of the wave vector $\mathbf{k}=\left(k_x,k_y,k_z\right)$ onto the direction $\hat{\mathbf{u}}_\alpha$ of the relevant wire array. It is implicitly assumed that the metallic loss is small so that the metal can be assumed a perfect electric conductor (PEC), which is an excellent approximation in the microwave domain up to terahertz frequencies (300GHz-3THz). The permittivity function depends explicitly on the wave vector $\mathbf{k}=j\nabla$, and hence, as already discussed, the uniaxial wire medium has a strongly nonlocal electromagnetic response [29-31]. For a rectangular lattice with dimensions $a\times b$, the plasma wave number β_p, which depends only on the lattice period and the radius of the wires, satisfies [25]:

$$\beta_p^2=\frac{\dfrac{2\pi}{s^2}}{\ln\left(\dfrac{s}{2\pi r_w}\right)+F\left(r\right)} \tag{2.5}$$

with $F\left(r\right)=-0.5\ln r+\pi r/6+\sum_{n=1}^{\infty}\left(\coth\left(\pi nr\right)-1\right)/n$, $s=\sqrt{a\,b}$ and $r=a/b$. For the geometry of Fig. 2.1b the parameter *b* is equal to $\left(a/\cos(\alpha_2)\right)\cos(\alpha_1)$ for the 1st sub-array (in the top region, $0<z<d_1$) and equal to a for the 2nd sub-array (in the bottom region).

II.3.3 The Scattering Coefficients

We are interested in the scenario wherein a transverse magnetic (TM) polarized incident wave illuminates the bent wire medium. The incident magnetic field is directed along the *x*-direction and the incidence plane is the (*yoz)* plane. Because the optical axis of the two wire medium regions lies in the incidence plane, it follows that the magnetic field is of the form $\mathbf{H} = H_x(y,z)\hat{\mathbf{x}}$. Thus, the incident wave can excite only extraordinary waves in the wire medium regions. As is well known [29-31], different from conventional uniaxial materials the uniaxial wire medium supports *two* distinct extraordinary waves, which are usually referred to as the transverse magnetic (TM) mode and the transverse electromagnetic (TEM) mode. This unusual property is a consequence of the nonlocal effects. Supposing that the incident wave vector is of the form $\mathbf{k}^{inc} = k_y\hat{\mathbf{y}} - j\gamma_0\hat{\mathbf{z}}$ with $\gamma_0 = \sqrt{k_y^2 - (\omega/c)^2}$ then the wave vectors associated with the extraordinary modes excited in a wire medium with optical axis along the direction $\hat{\mathbf{u}}_\alpha$ are of the form [27-28]:

$$\mathbf{k}_{TM}^{\pm} = k_y\hat{\mathbf{y}} + k_{z,TM}^{\pm}\hat{\mathbf{z}}, \qquad k_{z,TM}^{\pm} = \pm\sqrt{\varepsilon_h\left(\frac{\omega}{c}\right)^2 - \beta_p^2 - k_y^2}\,. \tag{2.6a}$$

$$\mathbf{k}_{TEM}^{\pm} = k_y\hat{\mathbf{y}} + k_{z,TEM}^{\pm}\hat{\mathbf{z}}, \qquad k_{z,TEM}^{\pm} = \frac{\pm\sqrt{\varepsilon_h}\,\dfrac{\omega}{c} - k_y\sin\alpha}{\cos\alpha}\,. \tag{2.6b}$$

From the previous discussion, the magnetic field can be written in all regions of space as follows:

$$H_x = H_0^{inc} e^{-jk_y y} \times \begin{cases} e^{-\gamma_0 z} + Re^{+\gamma_0 z}, & z \le 0 \\ A_{TM1}^{+} e^{-jk_{z,TM1}^{+} z} + A_{TM1}^{-} e^{-jk_{z,TM1}^{-} z} + A_{TEM1}^{+} e^{-jk_{z,TEM1}^{+} z} + A_{TEM1}^{-} e^{-jk_{z,TEM1}^{-} z}, & 0 \le z \le d_1 \\ A_{TM2}^{+} e^{-jk_{z,TM2}^{+} z} + A_{TM2}^{-} e^{-jk_{z,TM2}^{-} z} + A_{TEM2}^{+} e^{-jk_{z,TEM2}^{+} z} + A_{TEM2}^{-} e^{-jk_{z,TEM2}^{-} z}, & d_1 \le z \le d_1 + d_2 \\ Te^{-\gamma_0 (z-(d_1+d_2))}, & z \ge d_1 + d_2 \end{cases} \quad (2.7)$$

In the above, H_0^{inc} is the complex amplitude of the incident wave, *R* and *T* are the reflection and transmission coefficients, and $A_{TM\,1,2}^{\pm}$ and $A_{TEM\,1,2}^{\pm}$ are the unknown amplitudes of the modes excited in the two wire medium regions. It is implicit that $k_{z,TEM}^{\pm}$ and $k_{z,TM}^{\pm}$ are evaluated with $\alpha = \alpha_1$ ($\alpha = \alpha_2$) in the region $0 \le z \le d_1$ ($d_1 \le z \le d_1 + d_2$), being d_1 and d_2 the thicknesses of the wire medium slabs. The electric field can be found from Eq. (2.7) noting that for a generic plane wave of the form $\mathbf{H} = H_0 \hat{\mathbf{x}} e^{-j\mathbf{k}\cdot\mathbf{r}}$ the corresponding electric field satisfies $\mathbf{E} = -\frac{H_0}{\omega} \bar{\bar{\varepsilon}}^{-1} \cdot (\mathbf{k} \times \hat{\mathbf{x}}) e^{-j\mathbf{k}\cdot\mathbf{r}}$. Hence, the electric field associated with a TEM plane wave is of the form

$$\mathbf{E}_{TEM} = \frac{\eta_h H_0}{\beta_h} \hat{\mathbf{u}}_p \hat{\mathbf{u}}_p \cdot (\hat{\mathbf{x}} \times \mathbf{k}_{TEM}) e^{-j\mathbf{k}_{TEM}\cdot\mathbf{r}}, \quad (2.8a)$$

whereas the electric field associated with a TM plane wave is of the form,

$$\mathbf{E}_{TM} = \frac{\eta_h H_0}{\beta_h} \left(\hat{\mathbf{u}}_p \hat{\mathbf{u}}_p + \frac{1}{\varepsilon_{\alpha\alpha}} \hat{\mathbf{u}}_\alpha \hat{\mathbf{u}}_\alpha \right) \cdot (\hat{\mathbf{x}} \times \mathbf{k}_{TM}) e^{-j\mathbf{k}_{TM}\cdot\mathbf{r}}, \quad (2.8b)$$

with η_h is the intrinsic impedance of the host medium. Noting that the magnetic field in each wire medium region is a superposition of TM and TEM plane waves [Eq. (2.7)], it is straightforward to write the electric field in all space in terms of the unknown coefficients (*R*, *T*, $A_{TM\,1,2}^{\pm}$ and $A_{TEM\,1,2}^{\pm}$).

II.3.4 Additional Boundary Conditions

The scattering problem coefficients *R*, *T*, $A^{\pm}_{TM\,1,2}$ and $A^{\pm}_{TEM\,1,2}$ (Eqs. 2.7 and 2.8) can be formed by enforcing proper boundary conditions at the interfaces $z=0$, $z=d_1$ and $z=d_1+d_2$. The usual Maxwellian boundary conditions imply that the tangential electric and magnetic fields (E_y, H_x) are continuous at the interfaces. Because of the nonlocal effects – particularly, due to the existence of two extraordinary waves – these Maxwellian boundary conditions are insufficient to solve the scattering problem; the unknowns outnumber the independent equations [27,32-34]. This property is explained by the fact that a nonlocal response implies that the material has some internal degrees of freedom, and thus one needs to impose additional boundary conditions (ABCs) on the pertinent internal variables beyond the Maxwellian boundary conditions. In the case of the wire metamaterial, the relevant internal degrees of freedom are the electric current and charge density in the metallic wires [34]. For example, it was demonstrated in Ref. [32] that at an interface $z=z_0$ with a standard dielectric the following ABC must be imposed:

$$\left\lfloor \varepsilon_h(z) E_z \right\rfloor_{z=z_0} = 0 .$$

(2.9)

Here the notation $\lfloor F \rfloor_{z=z_0}$ is defined as $\lfloor F \rfloor_{z=z_0} = F\big|_{z=z_0^+} - F_{z=z_0^-}$ and represents the jump discontinuity across the interface. Hence, the normal component of the electric field multiplied by the host permittivity is continuous at an interface with a dielectric material. This ABC guarantees that the microscopic current flowing along the metallic wires vanishes at the

interfaces [32].

Evidently, the electric current is not required to vanish at the interface of the two wire mediums in Fig. 2.1b ($z = d_1$) because the wires in the two regions are physically connected. Thus, the boundary condition 2.9 is not suitable for the interface at $z = d_1$. Instead, for bent wires it is physically more reasonable to impose that the current and the so-called additional potential φ [31,34] are continuous across the interface. The additional potential is the average potential drop from a given wire to the respective unit cell boundary. It was shown in Ref. [27], that the averaged electric current density can be written as follows:

$$\mathbf{J}_c = \left(-j\mathbf{k}_{\parallel} + \hat{\mathbf{z}} \frac{d}{dz} \right) \times \mathbf{H} - j\omega\varepsilon_0 \varepsilon_h \mathbf{E} \,. \tag{2.10}$$

Here, $\mathbf{k}_{\parallel} = k_y \hat{\mathbf{y}}$ is the projection of the incident wave vector on the interface (parallel to the *xoy* plane). The electric current flowing along the wires is $I_\alpha = \left(\mathbf{J}_c \cdot \hat{\mathbf{u}}_\alpha \right) a \times b$. Thus, the continuity of the current at $z = z_0$ can be expressed as:

$$\cos\alpha_1 \, \mathbf{J}_c \cdot \hat{\mathbf{u}}_{\alpha 1}\big|_{z=z_0^-} = \cos\alpha_2 \, \mathbf{J}_c \cdot \hat{\mathbf{u}}_{\alpha 2}\big|_{z=z_0^+} \,. \tag{2.11}$$

On the other hand, the additional potential may be written in terms of the current density as $\varphi = -\dfrac{1}{j\omega\varepsilon_h \beta_p^2} \dfrac{d}{ds} \left(\mathbf{J}_c \cdot \hat{\mathbf{u}}_\alpha \right)$, being $\dfrac{d}{ds} = \hat{\mathbf{u}}_\alpha \cdot \nabla = \hat{\mathbf{u}}_\alpha \cdot \left(-j\mathbf{k}_{\parallel} + \hat{\mathbf{z}} \dfrac{d}{dz} \right)$ the derivative along the wires direction [31,34]. Thus, the continuity of the additional potential at the interface $z = z_0$ implies that:

$$\frac{1}{\varepsilon_{h1}\beta_{p1}^2} \left(-j\mathbf{k}_{\parallel} \cdot \hat{\mathbf{u}}_{\alpha 1} + \hat{\mathbf{z}} \cdot \hat{\mathbf{u}}_{\alpha 1} \frac{d}{dz} \right) \mathbf{J}_c \cdot \hat{\mathbf{u}}_{\alpha 1}\big|_{z=z_0^-} = \frac{1}{\varepsilon_{h2}\beta_{p2}^2} \left(-j\mathbf{k}_{\parallel} \cdot \hat{\mathbf{u}}_{\alpha 2} + \hat{\mathbf{z}} \cdot \hat{\mathbf{u}}_{\alpha 2} \frac{d}{dz} \right) \mathbf{J}_c \cdot \hat{\mathbf{u}}_{\alpha 2}\big|_{z=z_0^+} \,. \tag{2.12}$$

It should be noted that when the wires are not connected at the interface, i.e. if there is either a shift (figure 2.1c) or a very small gap between the two sets of tilted metallic wires, the current along the wires direction vanishes at the interface $z = z_0$, i.e. one should enforce instead that,

$$\mathbf{J}_c \cdot \hat{\mathbf{u}}_{\alpha 1}\big|_{z=z_0^-} = 0\,, \qquad \mathbf{J}_c \cdot \hat{\mathbf{u}}_{\alpha 2}\big|_{z=z_0^+} = 0\,. \tag{2.13}$$

In summary, one needs to impose exactly ten boundary conditions. Six boundary conditions are related to the continuity of E_y, H_x at the three interfaces. The remaining four boundary conditions are the ABCs. A single ABC [Eq. (2.9)] is enforced at the interfaces $z = 0$ and $z = d_1 + d_2$. On the other hand, at the interface $z = d_1$ two ABCs are required: Eqs. (2.11) and (2.12) if the wires are physically connected, or, alternatively Eq. (2.13) if the wires are disconnected. Hence, in this manner one can obtain a 10×10 linear system that can be numerically solved to find the excited electromagnetic field distribution. It is possible to show that the ABCs together with the standard Maxwellian boundary conditions ensure the continuity of the power flow at an interface [35].

II.4 Extreme Anisotropy Approximation

II.4.1 Effective model

When the metallic wires are densely packed (the limit $a/L \to 0$) it is possible to ignore the effects of the TM wave [28], and hence the wave propagation in the wire medium is determined only by the TEM wave. It is known that the TEM waves effectively experience an infinite permittivity along the wires direction ($\varepsilon_{\alpha\alpha} = \infty$). Hence, in the $a/L \to 0$ limit the wire medium can be regarded as a *local* material with extreme anisotropy described by the

permittivity function [28],

$$\frac{\bar{\varepsilon}}{\varepsilon_0} = \left(\varepsilon_h \hat{\mathbf{u}}_x \hat{\mathbf{u}}_x + \varepsilon_h \hat{\mathbf{u}}_p \hat{\mathbf{u}}_p + \infty \hat{\mathbf{u}}_\alpha \hat{\mathbf{u}}_\alpha \right) . \tag{2.14}$$

Hence, for densely packed wire arrays the spatial dispersion effects can be neglected, and in particular the ABCs are not required to solve the scattering problem.

II.4.2 Transmission Properties

It is possible to obtain a closed analytical formula for the transmission coefficient in the extreme anisotropy limit. Setting the coefficients $A^{\pm}_{TM\,1,2} = 0$ in Eq. (2.7) and imposing the standard Maxwellian boundary conditions it is found that:

$$T = \frac{-8 j \gamma_0 k_0 \sqrt{\varepsilon_h} \cos\alpha_1 \cos\alpha_2}{A}, \tag{2.15a}$$

$$\begin{aligned} A = \sum_{\pm} & \left(k_0 \cos\alpha_1 \pm \left(-j\gamma_0 \sqrt{\varepsilon_h} \right) \right) e^{j k^{\pm}_{z,TEM\,1} d_1} \\ & \times \Big[\left(k_0 \cos\alpha_2 - j\gamma_0 \sqrt{\varepsilon_h} \right) \left(\cos\alpha_2 \pm \cos\alpha_1 \right) e^{j k^{+}_{z,TEM\,2} d_2} \\ & - \left(k_0 \cos\alpha_2 + j\gamma_0 \sqrt{\varepsilon_h} \right) \left(\cos\alpha_2 \pm \left(-\cos\alpha_1 \right) \right) e^{j k^{-}_{z,TEM\,2} d_2} \Big] \end{aligned} . \tag{2.15b}$$

The sum with index "±" is a shorthand notation for the sum of two terms: one with "+" sign and the other with "–" sign.

An array of straight metallic wires can be seen as a set of deeply subwavelength waveguides that perform pixel to pixel imaging. Particularly, when the length of the wires is tuned to satisfy the Fabry-Pérot condition (i.e., $k_h L = n\pi$, with *n* integer and $k_h = \sqrt{\varepsilon_h}\,\omega / c$) the wire array is operated in the so-called canalization regime [36-37], wherein the energy tends to flow along the wires direction with little lateral spreading. This regime enables the transport of a complex near-field distribution from a source plane to an image plane with subwavelength resolution.

Consistent with this property, in the extreme anisotropy limit when $\alpha \equiv \alpha_1 = \alpha_2$ the transmission coefficient reduces to $T_{FP} = -e^{ik_y L \sin\alpha}$ at the Fabry-Pérot resonance $k_h L = \pi$, where $L = L_1 + L_2$. The linear phase variation indicates that the magnetic field at the output plane differs from the magnetic field at the input plane simply by a lateral spatial shift: $H_x^{out}(y) = -H_x^{in}(y - L\sin\alpha)$. Thus, in the extreme anisotropy limit the wire medium ensures the image transport with no distortion.

What happens when two different wire medium regions ($\alpha_1 \neq \alpha_2$) are put together? Can the metamaterial still ensure a perfect near-field transport in the canalization regime (i.e., when the total length of the wires satisfies the Fabry-Pérot condition)? Strictly speaking, the answer is negative. It can be shown that at the Fabry-Pérot resonance ($k_h(L_1 + L_2) = \pi$) Eq. (2.15) reduces to:

$$T_{FP} = \frac{-8\, j\, \gamma_0 k_0 \sqrt{\varepsilon_h} \cos\alpha_1 \cos\alpha_2 e^{j k_y (\sin\alpha_1 L_1 + \sin\alpha_2 L_2)}}{B} \tag{2.16a}$$

$$B = 2\, j\gamma_0 k_0 \sqrt{\varepsilon_h} (\cos\alpha_1 + \cos\alpha_2)^2 + (\cos\alpha_2 - \cos\alpha_1) \sum_{\pm} \pm \left(k_0 \cos\alpha_2 \pm j\gamma_0 \sqrt{\varepsilon_h}\right)\left(k_0 \cos\alpha_1 \pm \left(-j\gamma_0 \sqrt{\varepsilon_h}\right)\right) e^{\pm\left(-2jk_0 \sqrt{\varepsilon_h} L_2\right)} \tag{2.16b}$$

When the optical axis of the wire medium is bent the transmission coefficient [Eq. (2.16)] does not satisfy anymore $|T_{FP}| = 1$ for every k_y, even in the considered idealized extreme anisotropy limit, and in general $|T_{FP}|$ varies with the transverse wave number k_y. Interestingly, it can be checked that when $L_1 = L_2$ the transmission coefficient reduces to:

$$T_{FP,L_1=L_2} = \frac{-2\cos\alpha_1\cos\alpha_2}{\cos^2\alpha_1+\cos^2\alpha_2} e^{jk_y(\sin\alpha_1 L_1+\sin\alpha_2 L_2)}, L_1 = L_2 . \quad (2.17)$$

In this case, the transmission coefficient amplitude becomes independent of k_y, but depends on the tilting angles. In particular, if one of the tilting angles approaches 90º and the other tilting angle is kept near zero the transmission level will drop sharply ($T_{FP,L_1=L_2} \to 0$). However, provided both tilting angles are kept smaller than about 45º the transmission level remains good for all propagating and evanescent waves. This property suggests that the wire metamaterial may be quite robust to the effect of bending. This conclusion will be further substantiated in the next section, where we consider the effects of spatial dispersion and compare the results with full wave simulations.

It is interesting to note that from Eq. (2.11) one has precisely $|T_{FP}| = 1$ when $\alpha_2 = -\alpha_1$. Actually, such a property is completely general and it can be checked that when $\alpha_2 = -\alpha_1$ Eq. (2.16) reduces to $T_{FP,\alpha_1=-\alpha_2} = -e^{+jk_y \sin\alpha(L_1-L_2)}$ with $\alpha = \alpha_1$ even when $L_1 \neq L_2$. Thus, when $\alpha_2 = -\alpha_1$ the metamaterial behaves as an ideal endoscope (in the extreme anisotropy limit) similar to the case of straight wires.

II.5 Near-Field Transport by Multi-Wire Endoscopes - Scattering Characteristics

For realistic wire arrays a/L is finite, and hence the effects of spatial dispersion are non-negligible. Thus, in general the TM wave cannot be neglected and the scattering parameters need to be found using the general theory of Sect.II.3. In the following, we present a detailed numerical study of the reflection and transmission coefficients obtained with such an approach,

and compare the results with full wave simulations. We will discuss the interesting limiting cases of extreme anisotropy and equal tilt angles ($\alpha_1 = -\alpha_2$) and equal lengths $L_1 = L_2$ showing that the magnitude of the transmission coefficient at the Fabry-Pérot condition is independent of the wavenumber k_y and it is close to unity (for all the spectral k_y components of the magnetic field). Even when α_1 is different from $\pm\alpha_2$ the bent endoscope has still a satisfactory response in the canalization regime.

II.5.1 Connected wires

In the first example, we consider a geometry with $\alpha_1 = -\alpha_2 = 45^\circ$, $L_1 = L_2$ and suppose that the wires are connected at the bending point. Furthermore, the wires are embedded in air ($\varepsilon_h = 1$) and the frequency is fixed such that $k_0 a = 0.1$. Figures 2.2 and 2.3 show the amplitudes of the transmission and reflection coefficients as function of the transverse component of the wave vector k_y for different values of the wires length. The solid lines in the figures were obtained with the (nonlocal) analytical model, whereas the discrete symbols were obtained from full wave simulations with CST Microwave Studio [38]. As seen, on the overall there is an excellent correspondence between the two approaches and the analytical results are well supported by full-wave simulations with CST, which validates our theoretical approach. In all the examples of the article $|T|$ and $|R|$ are even functions of k_y and hence the plot range is restricted to positive values of the transverse wave vector.

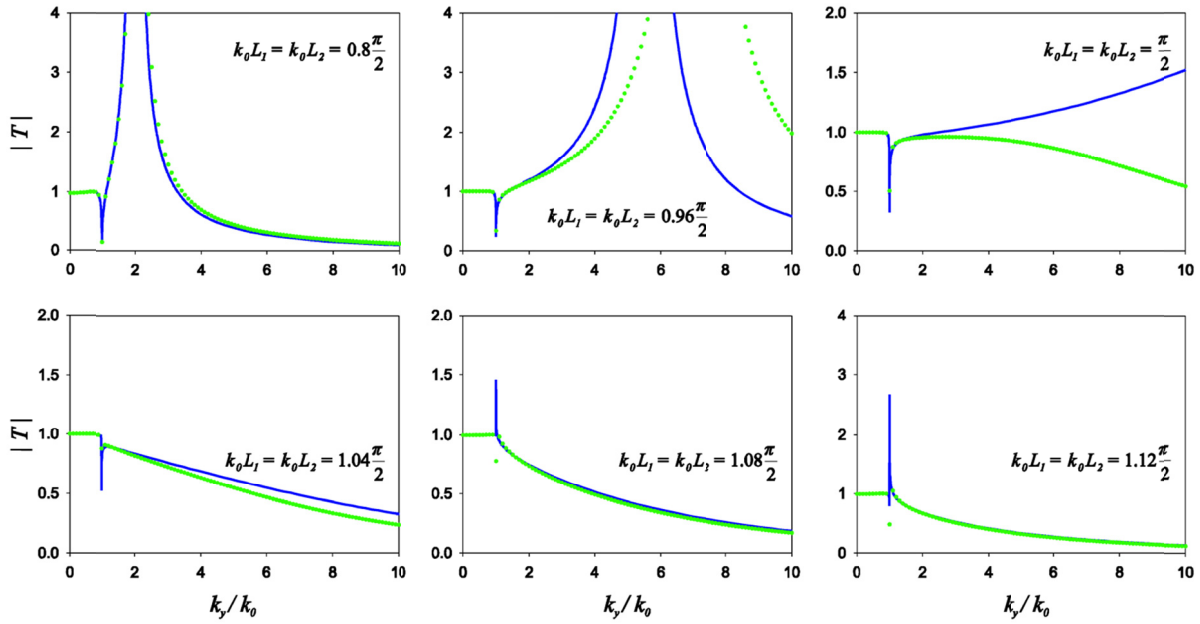

Figure 2.2: Amplitude of the transmission coefficient as function of the normalized transverse wave vector k_y/k_0 for two connected tilted wire mediums and different wire lengths. The normalized frequency is fixed ($k_0a = 0.1$). The host permittivity is $\varepsilon_h = 1$, the wire radii is $r_w = 0.05a$ and the tilting angles are $\alpha_1 = -\alpha_2 = 45°$. The solid lines (blue lines) are calculated using our analytical nonlocal model, and the discrete symbols (green) were obtained using full wave simulations [38].

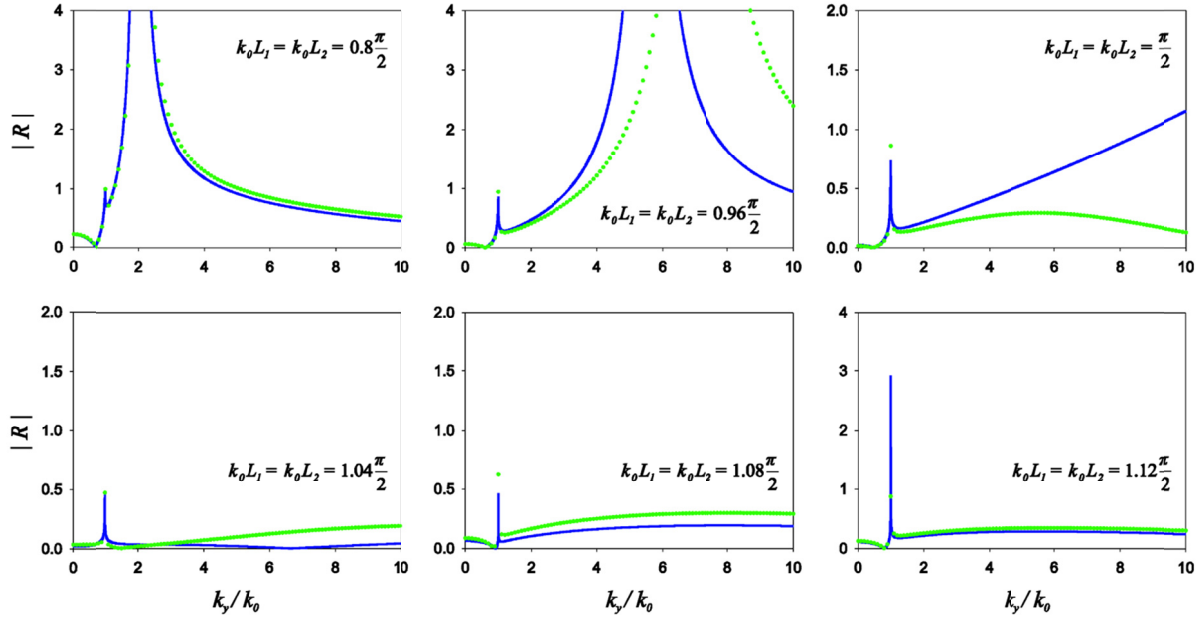

Figure 2.3: Amplitude of the reflection coefficient as function of the normalized transverse wave vector k_y/k_0 for two connected tilted wire mediums and different wire lengths. The geometry is as in Fig. 2.2.

Consistent with the discussion of Sect.II.4, figures 2.2 and 2.3 reveal that when $k_0 L_1 = k_0 L_2 = \pi/2$, i.e. when the total wires length is tuned to satisfy the Fabry-Pérot condition, one has $|T| \approx 1$ and $|R| \approx 0$. Indeed, the behavior of the transfer function of the bent wire medium is qualitatively similar to that of the straight [28,39] wire medium. Thus, similar to the case of a slab with wires normal [39] or tilted [28] with respect to the interface, the bent wire medium can operate in the canalization regime and enable subwavelength imaging. Below the Fabry-Pérot resonance the transmission coefficient always has a pole with a broad resonance. On the other hand, above the Fabry-Pérot resonance there are no relevant resonant features in the transmission coefficient. Note that the extreme anisotropy model predicts that for the present configuration $\left|T_{FP,\alpha_1=-\alpha_2}\right| = 1$, but such a result assumes that $a/L \to 0$. There is some discrepancy between the homogenization results and the full wave simulations when $k_0 L_1 = k_0 L_2 = \pi/2$ because at resonance the system response is more sensitive to small perturbations.

As expected, the reflection and transmission coefficients are sensitive to variations in the electrical length of the wires. For wires with total length larger than half wavelength, the transmission and reflection coefficients for evanescent waves become weaker, similar to the case of straight wires [28,39]. On the other hand, for a total wire length smaller than half wavelength (i.e. below Fabry-Pérot condition), the transmission and reflection coefficients are greatly enhanced due to the excitation of guided modes propagating along the *y* direction of the slab, analogous to the results reported in [28,39] but here for the case of bent wires. Note that the poles of the transfer function determine the natural (surface) waves of the structure.

The excitation of guided waves is generally undesired in the context of near-field transport because it leads to strongly distorted images [39,40].

We did a similar study for the case wherein the tilting angles are $\alpha_1 = 0$ and $\alpha_2 = -45^\circ$ (Figs. 2.4 and 2.5). The main difference compared to the previous case is that the reflection coefficient for the propagating waves is considerably larger for $\alpha_1 = 0$ and $\alpha_2 = -45^\circ$. We also verified (not shown) that at the Fabry-Pérot resonance, the phase of the transmission coefficient varies linearly with k_y with slope $L_2 \sin\alpha_2$. This is consistent with the fact that for $\alpha_1 = 0$ and $\alpha_2 = -45^\circ$ the expected lateral shift of the transported image is $L_2 \sin\alpha_2$.

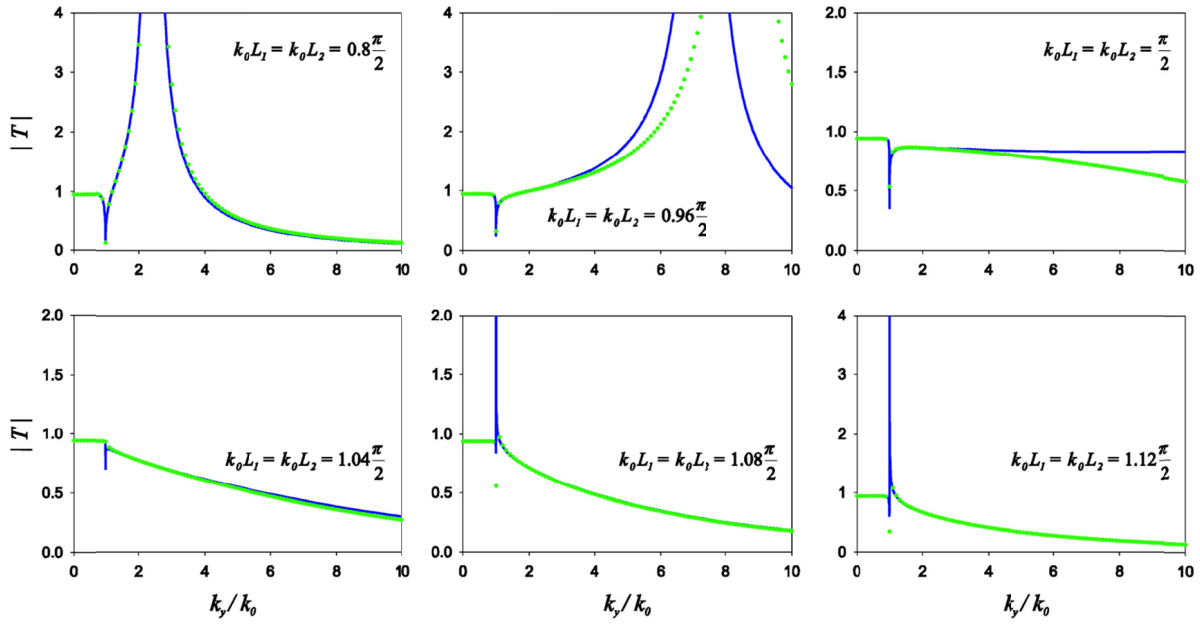

Figure 2.4: Amplitude of the transmission coefficient as function of the normalized transverse wave vector k_y / k_0 for two connected tilted wire mediums with $\alpha_1 = 0°$ and $\alpha_2 = -45°$. The remaining structural parameters and legend are as in Fig. 2.2.

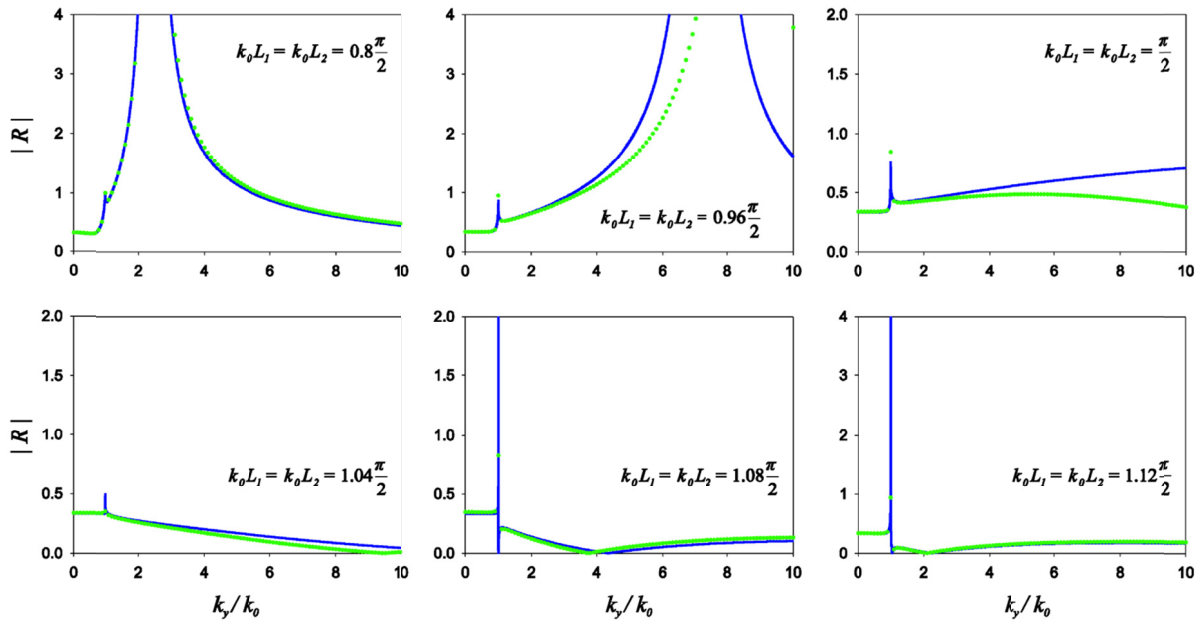

Figure 2.5: Amplitude of the reflection coefficient as function of the normalized transverse wave vector k_y/k_0 for two connected tilted wire mediums and different wire lengths. The geometry is as in Fig. 2.4.

An important point is that because of the nonlocal effects even when the total wires length satisfies the Fabry-Pérot condition, the transmission coefficient is close to unity only for a limited range of spatial harmonics. To estimate the resolution for which the bent wire medium operates with tolerable distortion we use the half-intensity criterion [39]. This criterion predicts a resolution equal to $\Delta = \pi / k_y^{\max}$, being $k_y^{\max}$ the largest k_y for which $1/\sqrt{2} \le |T| \le \sqrt{2}$. For the configuration with $\alpha_1 = -\alpha_2 = 45^\circ$ ($\alpha_1 = 0$ and $\alpha_2 = -45^\circ$) we find from the numerical CST simulations that $k_y^{\max} = 8.1k_0$ ($k_y^{\max} = 7.3k_0$). Thus, the imaging resolution is $\Delta \simeq \lambda_0/16.2$ for $\alpha_1 = -\alpha_2 = 45^\circ$ and $\Delta = \lambda_0/14.6$ for $\alpha_1 = 0$ and $\alpha_2 = -45^\circ$. In both cases, the minimum resolution is comparable to the lattice period ($a \approx \lambda_0/63$) [41], specifically $\Delta \sim 4a$.

II.5.2 Disconnected wires

It is interesting to study the impact of cutting the metallic wires at the bending point, so that the geometry is modified as sketched in Fig. 2.1c (misaligned wire arrays). Is the ohmic connection of the two wire arrays at the bending point crucial to have a good subwavelength imaging transport? To answer this question we calculated the transmission and reflection coefficients for $\alpha_1 = -\alpha_2 = 45^\circ$ when the two sets of wires are misaligned (Fig. 2.6). As seen, the response of the wire medium device becomes drastically different when the wire arrays are disconnected. In particular, the transmission coefficient exhibits a strongly resonant behavior in the vicinity of the Fabry-Pérot resonance, and hence the structure cannot be operated in the canalization regime. This property indicates that the ohmic connection between the wires is essential for a reliable near-field transport. We also verified that the system response remains nearly the same as in Fig. 2.6 when the two wire arrays are aligned but separated by a small air gap (not shown).

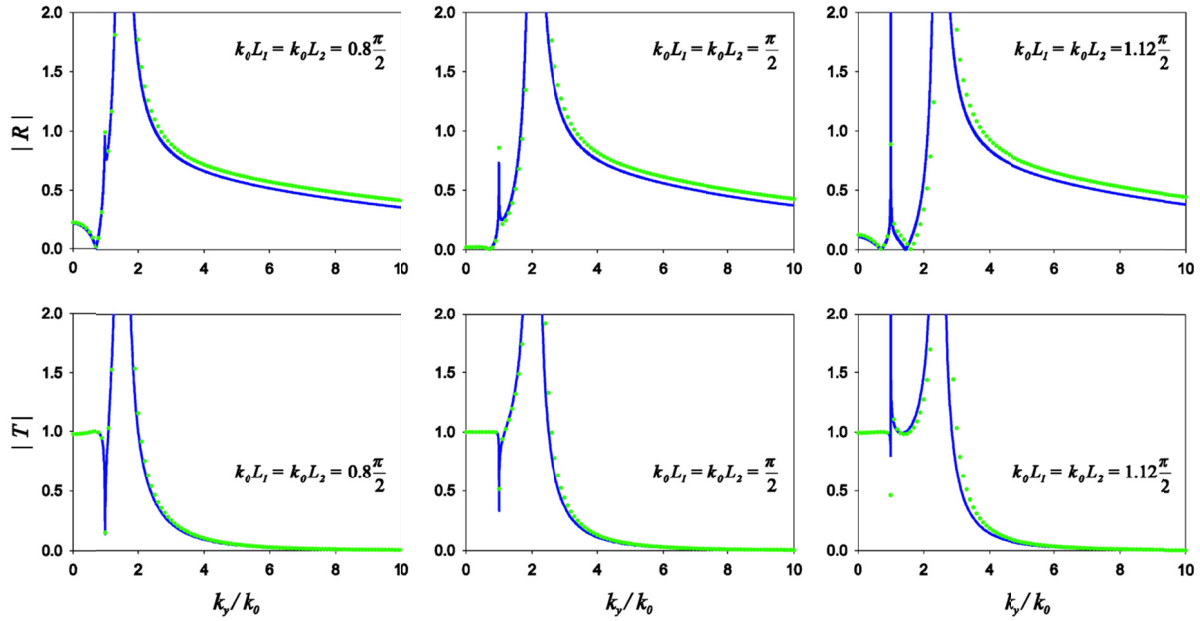

Figure 2.6: Amplitude of the reflection (top row) and transmission (bottom row) coefficients as function of the normalized transverse wave vector k_y / k_0 for two misaligned tilted wire mediums with $\alpha_1 = -\alpha_2 = 45°$ and different wire lengths. The spatial shift between the two wire arrays is $a/\sqrt{2}$. The remaining structural parameters and legend are as in Fig. 2.2.

It is worth underlined that the nonlocal analytical model perfectly captures the response of the metamaterial when the wires are disconnected. As discussed in Sect.II, the ABCs at the plane where the wires meet depend if they are connected or disconnected.

II.5.3 Extreme anisotropy limit

It is relevant to point out that the extreme anisotropy model of Sect.II.4 is a based on a local material response, and hence it is unable to distinguish if the wires are connected or disconnected at the interface. Thus, from this point of view, it is a bit a surprising that the responses for the connected and disconnected cases are qualitatively so different.

To better understand the limits of validity of the extreme anisotropy model, we suppose again that $\alpha_1 = -\alpha_2 = 45^\circ$, $L_1 = L_2$, and that the wires are tuned to satisfy the Fabry-Pérot condition $k_0 \left(L_1 + L_2 \right) = \pi$. According to the extreme anisotropy model for such a configuration $T_{FP,\alpha_1 = -\alpha_2} = -1$. To assess the perturbation caused by the spatial dispersion effects we calculated the transmission coefficient as function of the transverse component of the wave vector k_y (Fig. 2.7) for different values of a / L at the Fabry-Pérot resonance. We considered both the case of connected wires (solid lines) and disconnected wires (dashed lines). In Fig. 2.7, we can see the strong impact both of the non-locality and of broken wires in the transmittance of high spatial harmonics (corresponding to evanescent waves). In fact, the transfer function for disconnected wires is dramatically different from the transfer function for connected wires, as

predicted by the theory. Figure 2.7 shows that as a/L decreases, independent if the wires are connected or disconnected, the transmission coefficient approaches the extreme anisotropy limit. However, the convergence is much faster in the case wherein the wires are connected and for realistic values of a/L the extreme anisotropy model only approximates well the response of the connected configuration.

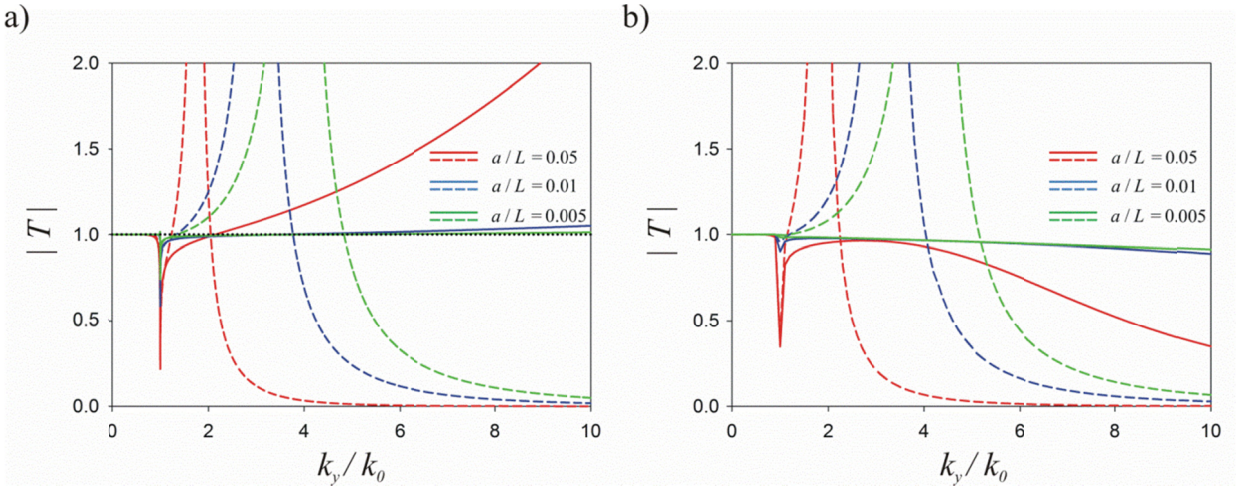

Figure 2.7: Amplitude of the transmission coefficient at the Fabry-Pérot resonance ($k_0(L_1+L_2)=\pi$) as function of the normalized transverse wave vector k_y/k_0 for different values of a/L. The host permittivity is $\varepsilon_h=1$, the wire radii is $r_w=0.05a$, the wires have identical length $L_1=L_2$, and the tilting angles are $\alpha_1=-\alpha_2=45°$. Solid lines: connected wire arrays. Dashed lines: disconnect wire arrays. (i) $a/L=0.05$ (red curves), (ii) $a/L=0.01$ (blue curves), (iii) $a/L=0.005$ (green curves), and (iv) extreme anisotropy, $a/L\to 0$ (black dotted line of panel (a)). (a) Analytical model results, (b) full wave simulation results [38].

II.6 Bent Multi-Wire Endoscope

Finally, to further support the analysis, we numerically simulated the performance of realistic multi-wire endoscopes formed by a finite number of wires using CST Microwave Studio [38]. The endoscopes consist of 20×20 bent wires with equal lengths L_1 and L_2 ($L_1=L_2$) embedded in air.

II.6.1 Configuration I

In the first configuration, the two connected sets of wires are chosen to be mutually perpendicular ($\alpha_1 = -\alpha_2 = 45^\circ$) as illustrated in figures 2.8a and 2.8b. The length of the wires is tuned so that the Fabry-Pérot condition occurs at 1GHz ($L_1 + L_2 = 15cm$). The lattice constant *a* is chosen equal to 10mm.

The image is created by an incoming plane wave ($\mathbf{E}^{inc} = E\hat{\mathbf{y}}$, $\mathbf{H}^{inc} = H\hat{\mathbf{x}}$, with $E/H = -\eta_0$) that illuminates an opaque metallic screen with two narrow slits. The screen is placed at the distance $h = 8\,\mathrm{mm}$ from the front interface of the multi-wire endoscope.

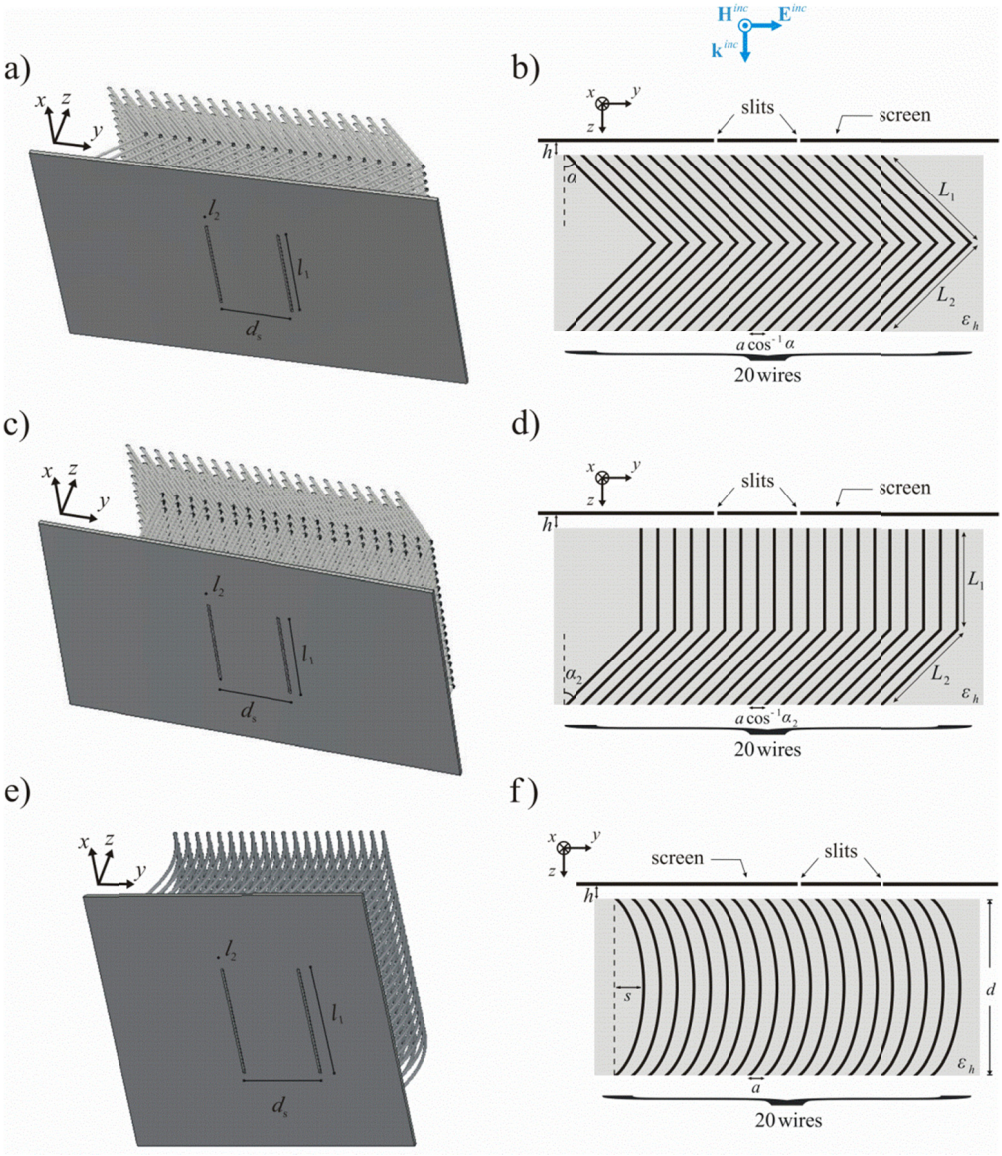

Figure 2.8: Geometry of the bent multi-wire endoscopes formed by 20×20 wires. (a), (c) and (e) perspective views, and (b), (d) and (f) top views. The image is created by an incident plane wave that illuminates an opaque screen with two narrow slits (see panel (b)).

Using CST Microwave Studio [38] we calculated the *y* and *z* components of the electric field (E_x is negligible) at the distance $d = 0.4a$ from the front and back interfaces of the endoscope. The simulated near field distributions at the design frequency are shown in Fig. 2.9. As can be seen, the two slits are clearly distinguished in both the source and image planes.

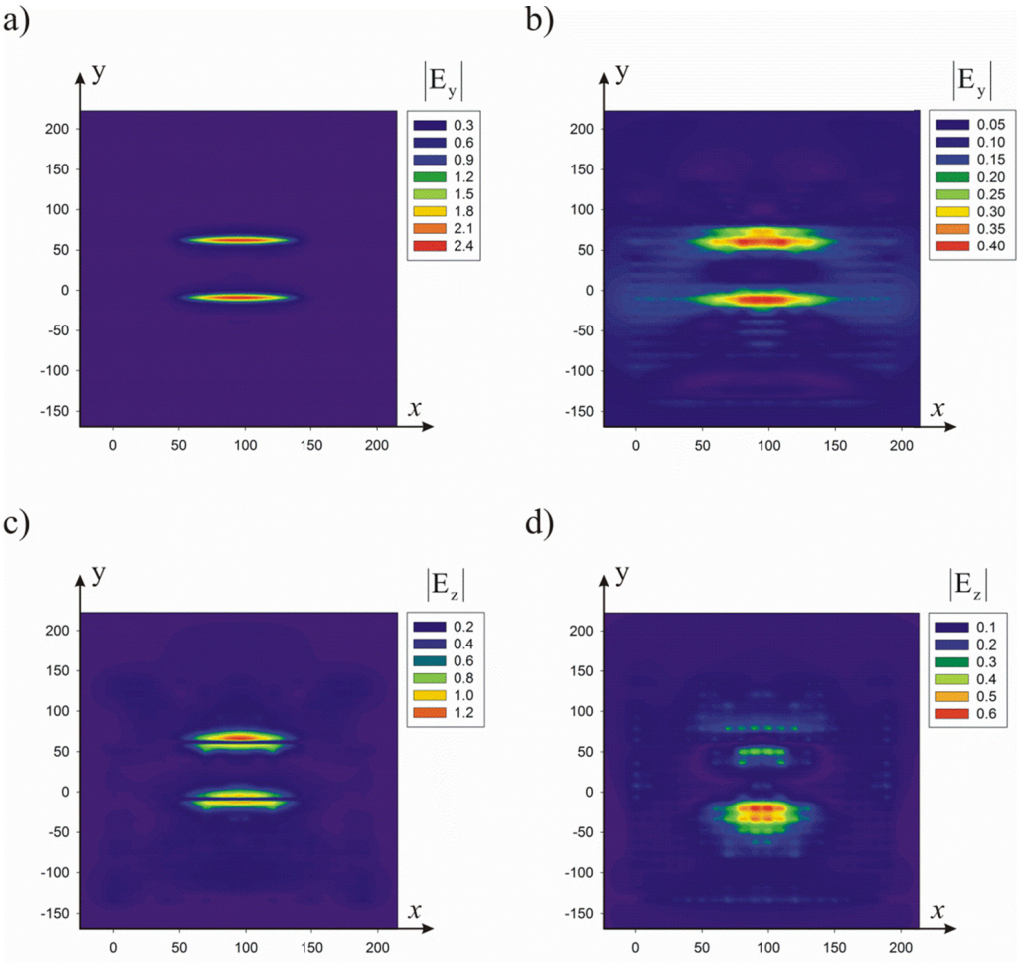

Figure 2.9: Density plot of the tangential $|E_y|$ *and normal* $|E_z|$ *components of the electric field at* 1GHz *for the endoscope with* $\alpha_1 = -\alpha_2 = 45°$. *(a), (c) at distance* $d = 0.4a$ *from the front interface (source plane) and (b), (d) at the distance* $d = 0.4a$ *from the back interface (image plane).*

Figure 2.10 shows how the near-field is guided along the wires from the source to the image plane.

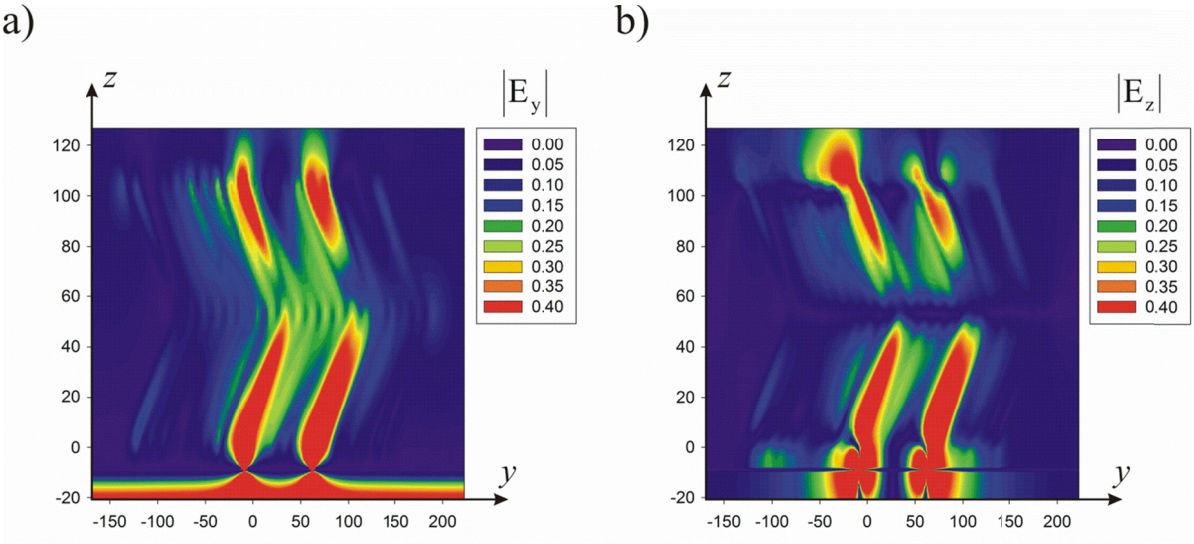

Figure 2.10: Density plot of the tangential $|E_y|$ *and normal* $|E_z|$ *components of the electric field at* 1GHz *at the mid-plane* $x = const.$ *of the endoscope for the example of Fig. 2.9.*

II.6.2 Configuration II

The second configuration is similar to the first one with the first set of wires is perpendicular to the interface ($\alpha_1 = 0^o$) and the second set is tilted by an angle $\alpha_2 = -45^\circ$ (figures 2.8c and 2.8d).

The simulated near field distributions at the design frequency are shown in Fig.2.11. In this configuration, the bent endoscope response is still satisfactory in the canalization regime and the transmitted image is shifted by $L_2 \sin\alpha_2$ due to the effect of bending the wires. Moreover, it is possible to estimate that the width of each "slit" at the image plane as 21.1 mm [for the slit less well discriminated] for the first configuration, and 12.3 mm for the second configuration. Comparing the resolution inferred by the CST simulation with the theoretical prediction $\left(\Delta = \lambda_0 / 16.2 = 18.5\text{mm and } \Delta = \lambda_0 / 14.6 = 20.5\text{mm, respectively}\right)$, it is found that the two values are reasonably consistent (especially for the first configuration), which further supports

our analytical approach.

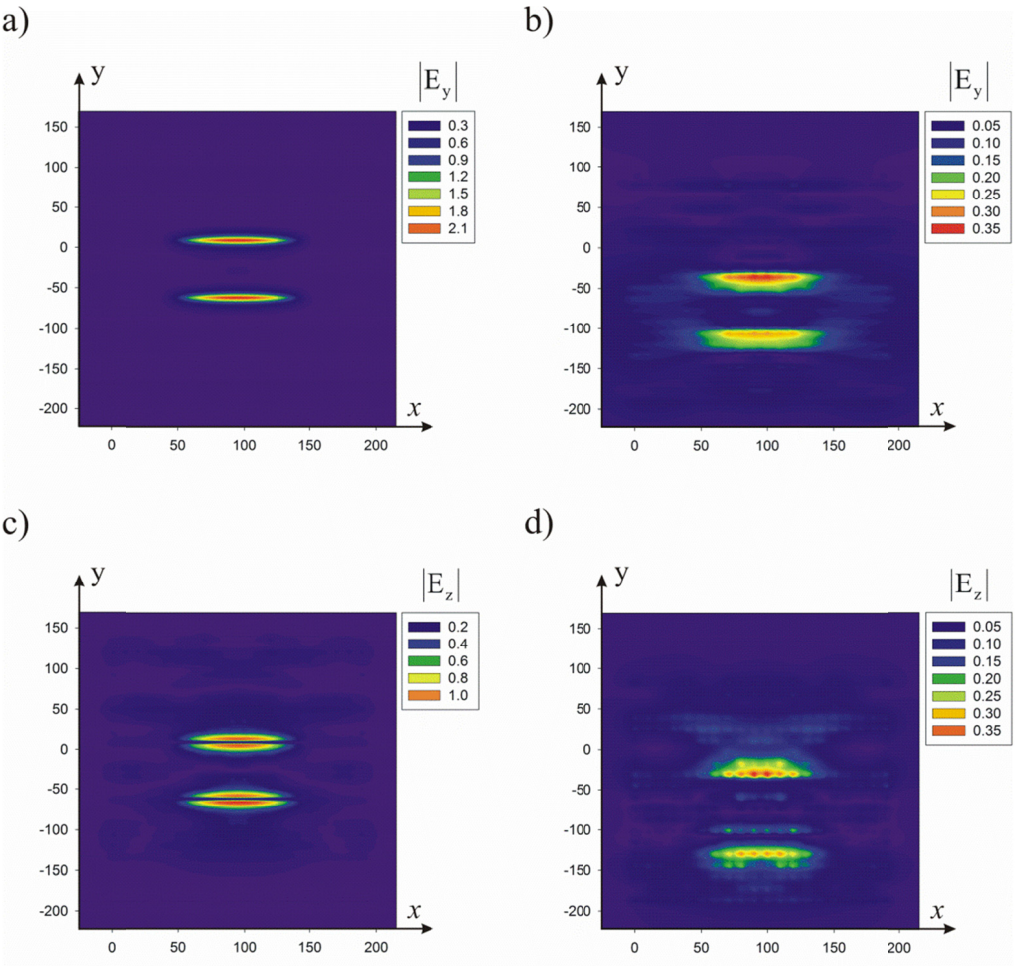

Figure 2.11: Similar to Fig. 2.9 but for an endoscope with the tilting angles $\alpha_1 = 0^o$ *and* $\alpha_2 = -45^o$.

II.6.3 Configuration III

As a final example, we consider a more realistic bent-wire endoscope formed by crescent-shaped wires (see Figs. 2.8e and 2.8f). The simulation parameters are the same as for the previous endoscopes and the bending of each wire is such that $d = 14.4cm$ and $s = 1.8cm$ (see Fig. 2.8f). As seen in Fig. 2.12, even in this example wherein the wires are continuously bent, the two slits are rather well discriminated and the resolution is $\Delta = 20mm$. Most importantly, the results of all simulations confirm that the multi-wire endoscope operated at the Fabry-Pérot

condition has a response quite robust to the effect of bending; further demonstrating their flexibility and the possibility of near-field transport with subwavelength resolution. By scaling the structure, it is in principle possible to obtain similar results at terahertz and infrared frequencies [41-42].

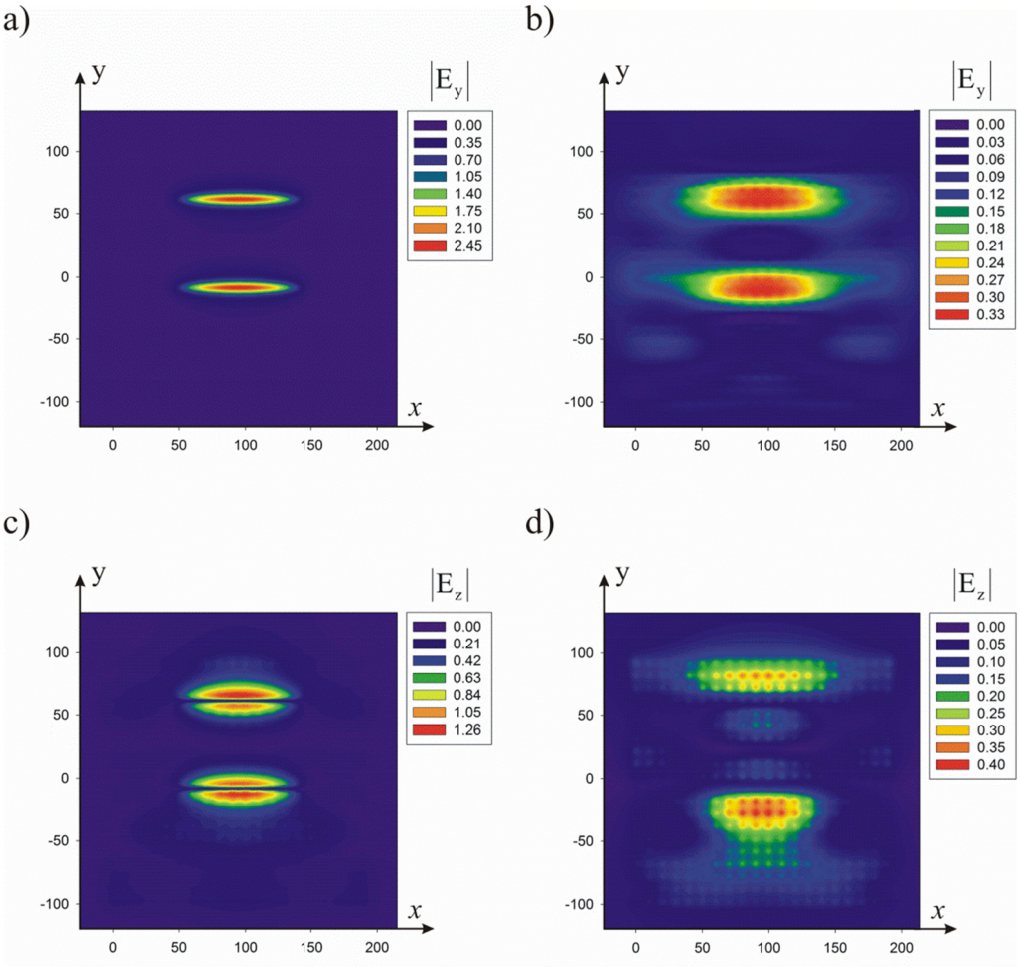

Figure 2.12: Similar to figures 2.9 and 2.11 but for the endoscope with crescent-shaped wires.

II.7 Conclusions

In summary, we investigated the impact of bending a multi-wire endoscope in the context of subwavelength imaging and near-field transport. In a first stage, we developed an analytical spatially dispersive model to characterize the scattering by a bent wire medium slab formed by an infinite number of wires. Two novel additional boundary conditions were formulated to describe the behavior of the macroscopic electromagnetic fields at the interface of two tilted wire mediums. For the case of connected wires, the ABCs impose that the current and the additional potential are continuous. We studied the reflection and transmission by a "bent" wire medium in different configurations and demonstrate that the structure can be quite tolerant and robust to the effect of bending provided the total length of the bent wires satisfies the Fabry-Pérot condition. It was proven that a structure formed by two connected tilted wire mediums can allow for the near field transport with a deeply subwavelength resolution. The presented research extends the results of several previous works [28,39] to the case of bent wires, and proves the possibility of near field transport with such structures based on the canalization principle. In particular, it was highlighted the importance of having a good ohmic contact at the interface to avoid a resonant behavior of the bent multi-wire array. The proposed theory was successfully tested against full wave numerical simulations for different configurations. Finally, to illustrate the applications and potentials of the results, we characterized the performance of realistic multi-wire endoscopes formed by a finite number wires using full wave numerical simulations, further demonstrating their robustness to the effect of bending and the possibility of near-field transport with subwavelength resolution.

References

[1] P. Ikonen, C. Simovski, S. Tretyakov, P. Belov P and Y. Hao "Magnification of subwavelength field distributions at microwave frequencies using a wire medium slab operating in the canalization regime", *Appl. Phys.* Lett. **91**, 104102, 2007.

[2] P. A. Belov, G. K. Palikaras, Y. Zhao, A. Rahman, C. R. Simovski, Y. Hao and C. Parini, "Experimental demonstration of multiwire endoscopes capable of manipulating near-fields with subwavelength resolution", *Appl. Phys. Lett.*, **97**, 191905, 2010.

[3] G. Shvets, S. Trendafilov, J. B. Pendry, A. Sarychev, "Guiding, Focusing, and Sensing on the Subwavelength Scale Using Metallic Wire Arrays", *Phys. Rev. Lett.* **99**, 053903, 2007.

[4] X. Radu, D. Garray, C. Craeye, "Toward a wire medium endoscope for MRI imaging", *Metamaterials* **3**, 90-99, 2009.

[5] Hafssaa Latioui and Mário G. Silveirinha, "Near-field transport by a bent multi-wire endoscope". *J. Appl. Phys.* 120, 063103, 2016.

[6] Hafssaa Latioui, Mário G. Silveirinha, "Multi-wire endoscopes for near-field transport", *4th Annual Conference of COST Action MP1204 & SMMO2016 Conference*, March 21-24, 2016, Lisbon – Portugal (with oral presentation).

[7] T. A. Morgado, J. S. Marcos, M. G. Silveirinha, S. I. Maslovski, "Experimental verification of full reconstruction of the near-field with a metamaterial lens", *Appl. Phys. Lett.* **97**, 144102, 2010.

[8] B. D. F. Casse , W. T. Lu , Y. J. Huang , E. Gultepe , L. Menon , S. Sridhar, "Super-resolution imaging using a three-dimensional metamaterials nanolens", *Appl. Phys. Lett.*, **96** , 023114, 2010.

[9] R.J. King, D. V. Thiel, K. Park, "The synthesis of surface reactance using an artificial dielectric," *IEEE Trans. Antennas Propag.*, **31**, 471, 1983.

[10] M. G. Silveirinha, C. A. Fernandes, J. R. Costa, "Electromagnetic Characterization of Textured Surfaces Formed by Metallic Pins", *IEEE Trans. on Antennas and Propag.*, **56**, 405-415, 2008.

[11] D. Sievenpiper, L. Zhang, R. Broas, N. Alexopolous, and E. Yablonovitch, "High-impedance electromagnetic surfaces with a forbidden frequency band", *IEEE Trans. Microwave Theory Tech.*, **47**, 2059-2074 , 1999.

[12] H.Y. Yang, R. Kim, D. R. Jackson, "Design Consideration for Modeless Integrated Circuit Substrates Using Planar Periodic Patches", *IEEE Trans. Microwave Theory and Tech.*, **48**, 2233, 2000.

[13] R. F. Jimenez Broas, D. F. Sievenpiper, and E. Yablonovitch, "A High-Impedance Ground Plane Applied to a Cellphone Handset Geometry", *IEEE Trans. Microwave Theory and Tech.*, **49**,

1262-1265, 2001.

[14] F. Yang, Y. Rahmat-Samii, "Reflection Phase Characterizations of the EBG ground plane for low profile wire antenna applications", *IEEE Trans. Antennas Propagat.*, **51**, 2691-2703, 2003.

[15] H. Mosallaei and K. Sarabandi, "Antenna Miniaturization and Bandwidth Enhancement Using a Reactive Impedance Substrate", *IEEE Trans. Antennas Propagat.*, **52**, 2403-2414, 2004.

[16] A. P. Feresidis, G. Goussetis, S. Wang, J. C. Vardaxoglou, "Artificial Magnetic Conductor Surfaces and Their Application to Low-Profile High-Gain Planar Antennas", *IEEE Trans. Antennas Propagat.*, **53**, 209-215, 2005.

[17] A. B. Yakovlev, M. G. Silveirinha, O. Luukkonen, C. R. Simovski, I. S. Nefedov, and S. A. Tretyakov, "Characterization of Surface-Wave and Leaky-Wave Propagation on Wire-Medium Slabs and Mushroom Structures Based on Local and Non-Local Homogenization Models", *IEEE Trans. Microwave Theory and Tech.*, **57**, 2700-2714, 2009.

[18] O. Luukkonen, M. G. Silveirinha, A. B. Yakovlev, C. R. Simovski, I. S. Nefedov, and S. A. Tretyakov, "Effects of Spatial Dispersion on Reflection from Mushroom-type Artificial Impedance Surfaces", *IEEE Trans. Microwave Theory and Tech.*, **57**, 2692-2699, 2009.

[19] J. J. Hopfield and D. G. Thomas, "Theoretical and experimental effects of spatial dispersion on the optical properties of crystals", *Phys. Rev.*, **132**, 563–572, 1963.

[20] L. D. Landau, E. M. Lifshitz, and L. P. Pitaevski, "Electrodynamics of Continuous Media", 2nd ed., **8**, 1984.

[21] V. M. Agranovich and V. L. Ginzburg, "Crystal Optics with Spatial Dispersion, and Excitons", (Springer-Verlag, 1984).

[22] S. I. Pekar and O. D. Kocherga, "Crystal Optics and Additional Light Waves", (Benjamin/Cummings, 1983).

[23] A. A. Orlov, P. M. Voroshilov, P. A. Belov, and Y. S. Kivshar, "Engineered optical nonlocality in nanostructured metamaterials", *Phys. Rev. B*, **84**, 045424, 2011.

[24] J. B. Pendry, A.J. Holden, W. J. Stewart, and I. Youngs, "Extremely low frequency plasmons in metallic mesostructures", Phys. Rev. Lett., **76**, 4773-4776, 1996.

[25] P. A. Belov, S. A. Tretyakov, and A. J. Viitanen, "Dispersion and reflection properties of artificial media formed by regular lattices of ideally conducting wires", *J. of Electromagn. Waves and Appl.*, **16**, 1153–1170, 2002.

[26] S. I. Maslovski, S. A. Tretyakov, and P. A. Belov, Wire media with negative effective permittivity: A quasistatic model, Microwave Opt. Technol. Lett., **35**, 47-51, October, 2002.

[27] M. G. Silveirinha, C. A. Fernandes and J. R. Costa "Additional boundary condition for a wire medium connected to a metallic surface", *New J. Phys.*, **10**, 053011, 2008.

[28] T. A. Morgado and M. G. Silveirinha "Transport of an arbitrary near-field component with

an array of tilted wires", *New J. Phys.*, **11**, 083023, 2009.

[29] P. A. Belov, R. Marqués, S. I. Maslovski, I. S. Nefedov, M. Silveirinha, C. R. Simovsky and S. A. Tretyakov, "Strong spatial dispersion in wire media in the very large wavelength limit," *Phys. Rev. B*, **67**, 113103, 2003.

[30] M. G. Silveirinha, "Nonlocal homogenization model for a periodic array of epsilon-negative rods", *Phys. Rev. E*, **73**, 046612, 2006.

[31] S. I. Maslovski, M. G. Silveirinha, "Nonlocal permittivity from a quasistatic model for a class of wire media", *Phys. Rev. B*, **80**, 245101, 2009.

[32] M. G. Silveirinha "Additional Boundary Condition for the Wire Medium", *IEEE Trans. Antennas Propag.*, **54**, 1766–1780, 2006.

[33] M. G. Silveirinha, "Additional boundary conditions for nonconnected wire media", *New. J. Phys.*, **11**, 113016, 2009.

[34] S. I. Maslovski, T.A. Morgado, M. G. Silveirinha, C. S. R. Kaipa, A. B. Yakovlev, "Generalized additional boundary conditions for wire media", *New J. Phys.*, **12**, 113047, 2010.

[35] M. G. Silveirinha, S. I. Maslovski, "Radiation from elementary sources in a uniaxial wire medium", *Phys. Rev. B*, **85**, 155125, 2012.

[36] P. A. Belov, Y. Hao and S. Sudhakaran "Subwavelength microwave imaging using an array of parallel conducting wires as a lens", *Phys. Rev. B*, **73**, 033108, 2006.

[37] P. A. Belov, C. R. Simovski, P. Ikonen, "Canalization of subwavelength images by electromagnetic crystals", *Phys. Rev. B*, **71**, 193105, 2005.

[38] CST Studio SuiteTM 2014 (http://www.cst.com).

[39] P. A. Belov and M. G. Silveirinha, "Resolution of subwavelength transmission devices formed by a wire medium", *Phys. Rev. E*, **73**, 056607, 2006.

[40] A. Rahman, P. A. Belov, M. G. Silveirinha, C. R. Simovski, Y. Hao, C. Parini, "The importance of Fabry-Perot resonance and the role of shielding in subwavelength imaging performance of multiwire endoscopes" *Appl. Phys. Lett.*, **94**, 031104, 2009.

[41] M. G. Silveirinha, P. A. Belov and C. R. Simovski, "Ultimate limit of resolution of subwavelength imaging devices formed by metallic rods", *Opt. Lett.*, **33** 1726, 2008.

[42] C. R. Simovski, P. A. Belov, A. V. Atrashchenko, Y. S. Kivshar, "Wire metamaterials: physics and applications", *Adv. Mater.*, **24**, 4229-4248, 2012.

CHAPTER 3 :

Anomalous Light Tunneling In Interlaced Wire Meshes

III. Anomalous Light Tunneling In Interlaced Wire Meshes

III.1 Introduction

In this chapter, we study the transmission properties of a 3D metallic photonic crystal consisting of two interlaced wire meshes. We investigate the electrodynamics of interlaced 3D metallic meshes and show that it may give rise to the surprising phenomenon of narrow transmission resonances when two opaque wire meshes are combined.

It is well known that metallic grids block the propagation of light when the electric field is aligned with the metal strips [10-17]. This property is explored in many applications, such as in light polarizers and frequency selective surfaces. For example, a regular array of thin parallel metallic wires is typically used as a linear polarizer since only the light oscillations perpendicular to the wires can go through the structure. When the wire grid spans the three directions of space – the so-called three-dimensional (3D) connected wire medium [1,3,18-19] – the corresponding photonic crystal does not support any photonic (light) states in the long wavelength regime. Indeed, a 3D connected wire metamaterial is completely opaque to light propagation and has an electromagnetic response analogous to that of a free-electron gas [3,18]. Hence, intuitively one may expect that when two 3D wire meshes are spatially interlaced (Fig. 3.1a) the full structure should be a better reflector and should scatter light more strongly than the individual components. In fact, common sense suggests that the effects of the individual wire meshes should be “additive” and that the interlaced, i.e. when two meshes are combined, wire structure should, accordingly, block the light propagation more effectively. Surprisingly, we theoretically demonstrate that, even though each individual wire mesh is fully

opaque at low frequencies, the interlaced meshes can be nearly transparent to electromagnetic waves due to a scattering cancellation phenomenon. The results are interpreted in terms of interference between the fields radiated by the interlaced meshes, leading to resonant tunneling by a Fano-type effect. In fact, the light tunneling anomaly can be understood as a Fano resonance that occurs when a longitudinal wave satisfies the Fabry-Pérot condition.

We will focus on the regime in which the metals are very good conductors. Indeed, the reported effect is most surprising when the two wire networks scatter very strongly the incoming wave (which corresponds to the region of the full photonic band gap). Clearly this happens for wires with a large conductivity.

III.2 The single 3D connected wire mesh

Let us consider a single 3D connected wire medium (CWM) as depicted in Fig 3.1a, made of metallic wires with metal dielectric permittivity $\varepsilon_m = \varepsilon_m(\omega)$. The wires have radius r_w, are separated by a distance a along the coordinates-axes directions and embedded in a host dielectric with $\varepsilon_h = 1$.

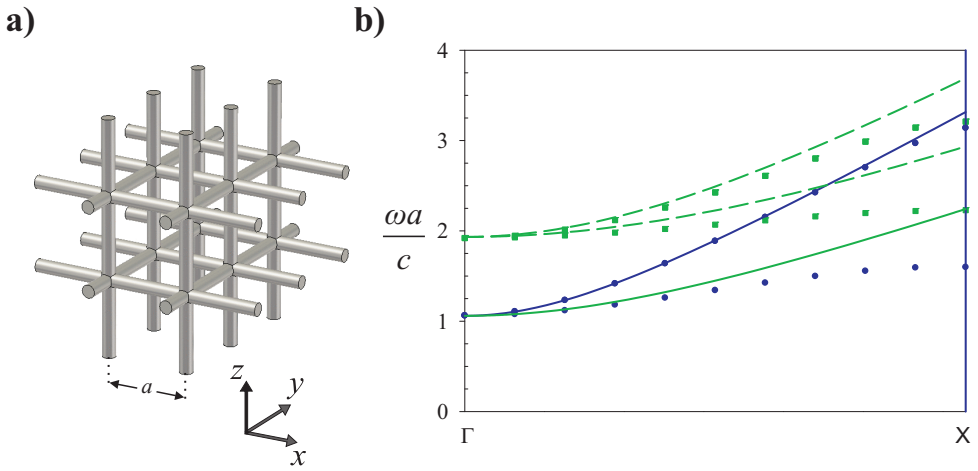

Figure 3.1: (a) Geometry of the single 3D connected wire medium. The wires are spaced by a distance a along the coordinate axes. (b) Band diagram of the electromagnetic modes along the ΓX *direction for each individual wire*

mesh. Solid lines: analytical model; Discrete symbols: full wave simulations [22]. The wires are PEC and are embedded in air. The lattice period is a. *Blue color: wire mesh A with* $r_{w,A} = 0.001a$. *Green color: wire mesh B with* $r_{w,\mathrm{B}} = 0.05a$.

III.2.1 Electromagnetic response

The homogenized permittivity of the medium can be written in terms of transverse ($\varepsilon_t(\omega)$) and longitudinal ($\varepsilon_l(\omega,k)$) components with respect to the wave vector $\mathbf{k}$ as [3],

$$\frac{\bar{\bar{\varepsilon}}}{\varepsilon_0} = \varepsilon_t(\omega)\left(\mathbf{1} - \frac{\mathbf{k}\otimes\mathbf{k}}{k^2}\right) + \varepsilon_l(\omega,k)\frac{\mathbf{k}\otimes\mathbf{k}}{k^2} \tag{3.1}$$

Where

$$\varepsilon_t(\omega) = 1 + \left(\frac{1}{\varepsilon_m - 1}\frac{1}{f_V} - \frac{\omega^2}{c^2 k_p^2}\right)^{-1}, \tag{3.1a}$$

$$\varepsilon_l(\omega,k) = 1 + \left(\frac{k^2}{l_0 k_p^2} + \frac{1}{\varepsilon_m - 1}\frac{1}{f_V} - \frac{\omega^2}{c^2 k_p^2}\right)^{-1}. \tag{3.1b}$$

where $\mathbf{1}$ is the identity dyadic and $\otimes$ denotes the tensor product. $f_V = \pi r_w^2/a^2$ is the volume fraction of the wires, $k_p = (2\pi/a)\Big/\sqrt{\ln\left(a/(2\pi r_w)\right) + 0.5275}$ is the effective plasma wave number and $l_0 = 3\Big/\left(1 + 2k_p^2/\beta_1^2\right)$ is a dimensionless slow wave factor that determines the strength of the nonlocal response [3,18]. The slow wave factor is typically on the order of $l_0 \sim 2$, and is written in terms of a parameter β_1 given by [3,18], $1/\beta_1^2 = 2\left(a/(2\pi)\right)^2 \sum_{n=1}^{\infty}\left[J_0\left((2\pi r_w/a)n\right)\right]^2/n^2$. Note that a local response would require $l_0 \to \infty$; the small value of l_0 highlights that the effective medium is strongly nonlocal.

Equation (3.1) shows that the plane-wave solutions supported by the artificial material can

be classified into transverse modes (with polarization perpendicular to the wave vector k) and a longitudinal mode (with polarization parallel to the wave vector k). Notice that unlike ε_t the longitudinal component ε_l depends on the wave vector and hence the artificial plasma has a nonlocal response. The dispersion characteristic of the transverse modes is given by $k^2 = (\omega/c)^2 \varepsilon_t(\omega)$. By solving $\varepsilon_l(\omega,k)=0$ with respect to k, the dispersion characteristic of the longitudinal mode reads $k^2 = l_0\left[k_0^2 - k_p^2 - \left(k_p^2/(\varepsilon_m - 1)\right)(1/f_v)\right]$.

Let us consider a slab of the considered metamaterial under TM plane-wave incidence. The metamaterial slab is periodic along the x and y directions and has a thickness L along z. The geometry of the problem is as depicted in the inset of Fig. 3.2. We assume that the incident magnetic field is along the x direction. The incoming wave can excite both the transverse and the longitudinal modes in the wire medium, hence an additional boundary condition [20,21] is required to solve the scattering problem. It was demonstrated in Ref. [3] that the transmission coefficient $T = T(\omega,k)$ is given by,

$$T = \sum_{j=1,2}\left[(-1)^j + \left(1 - \frac{1}{\varepsilon_t}\right)\frac{k_y^2}{\gamma_0 k_z^L} f_j\left(\frac{k_z^L L}{2}\right) - \frac{k_z^T}{\gamma_0 \varepsilon_t} f_j\left(\frac{k_z^T L}{2}\right)\right]^{-1} \tag{3.2}$$

with $f_1(x) = \cot(x)$ and $f_2(x) = \tan(x)$

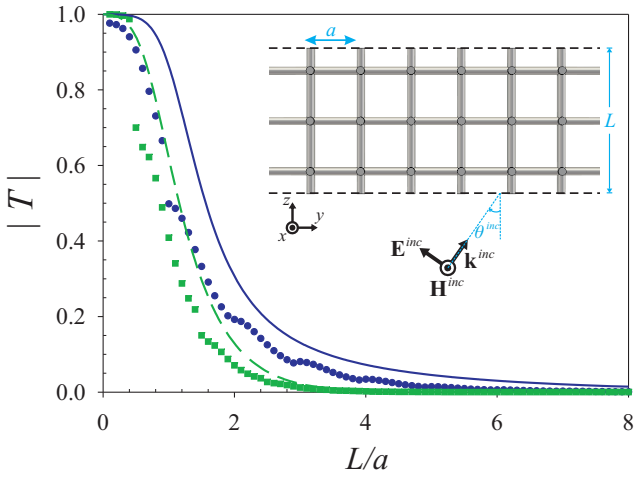

Figure 3.2: Amplitude of the transmission coefficient as function of the normalized thickness for the fixed frequency $\omega a / c = 1.32$ *and incidence angle* 80°. *Blue color: wire mesh A with* $r_{w,A} = 0.001a$. *Green color: wire mesh B with* $r_{w,B} = 0.05a$. *Solid lines: analytical model [3]; Discrete symbols: full wave simulations [22]. The inset shows the geometry of the problem.*

III.2.2 Numerical results

Let us consider two independent 3D metallic wire meshes "A" and "B". The metal is assumed to be a perfect electric conductor (PEC; $\varepsilon_m = -\infty$) and the host material is air ($\varepsilon_h = 1$). The wire radius is $r_{w,A} = 0.001a$ for the wire mesh A and $r_{w,B} = 0.05a$ for the wire mesh B. Figure 3.1b shows the photonic band structure along the ΓX direction calculated with CST Microwave Studio (discrete symbols) and with the analytical model (solid lines). As seen, the individual wire meshes do not support light states in the long wavelength regime [3,18].

We consider the case where a finite slab of the considered metamaterial is illuminated by an incident plane wave polarized as shown in the inset of Fig. 3.2, with the incidence angle $\theta^{\text{inc}} = 80^\circ$. The oscillation frequency is fixed as $\omega a / c = 1.32$. Figure 3.2 depicts the amplitude of the transmission coefficient as function of the normalized thickness L / a for each of the

individual wire meshes. As seen, for a sufficiently thick metamaterial slab the transmission level is rather weak.

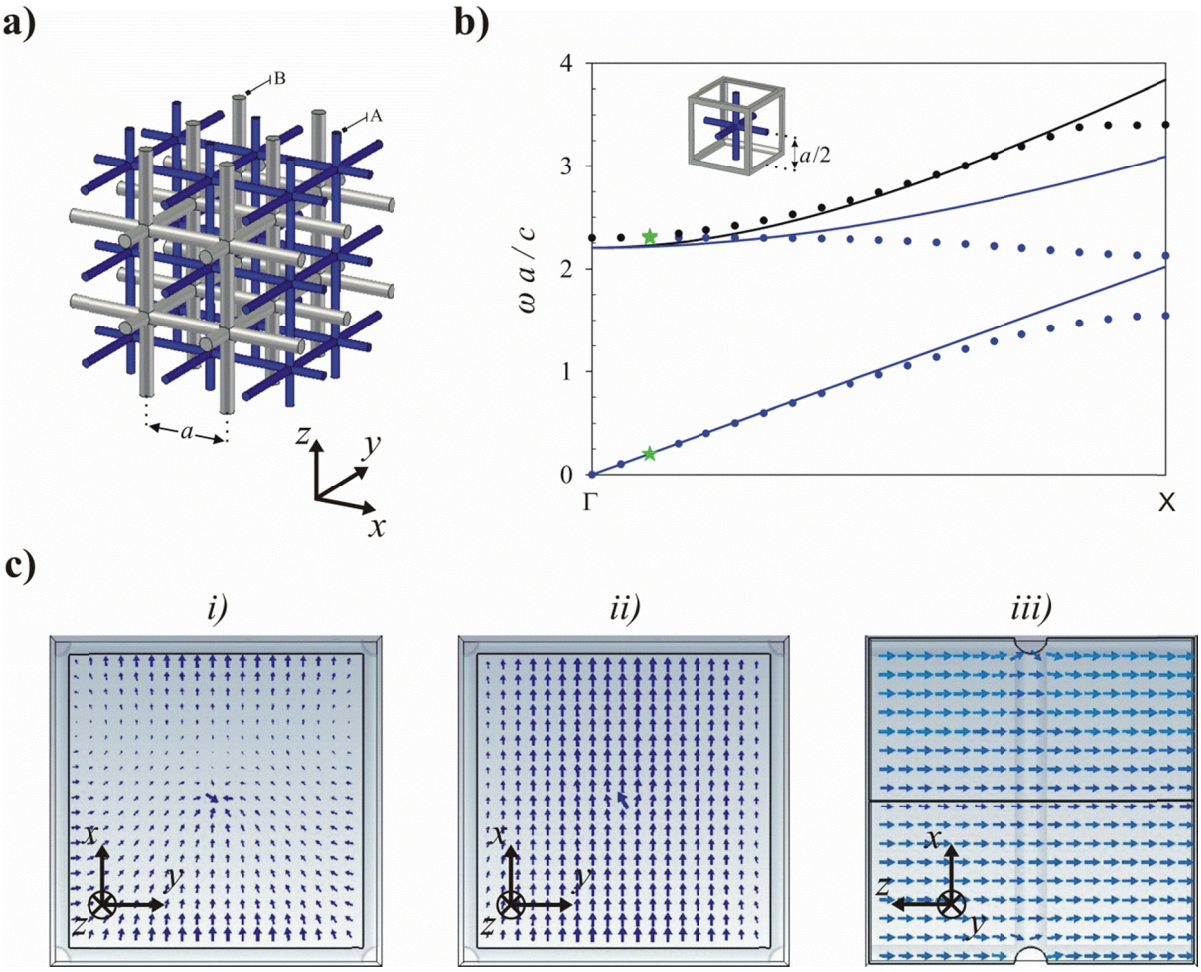

Figure 3.3: (a) Geometry of the interlaced wire meshes. The wires of each network are spaced by a distance a along the coordinate axes. The distance between the two non-connected networks is $a/2$. (b) Band diagram of the electromagnetic modes along the direction ΓX. Solid lines: analytical model; Discrete symbols: full wave simulations. The inset shows the cubic unit cell of the structure. The wires are PEC and are embedded in a dielectric with permittivity $\varepsilon_h = 1$; the radii of the wires are: $r_{w,A} = 0.001a$ and $r_{w,B} = 0.05a$. (c) Electric field profile for i) Low-frequency longitudinal mode at $\omega a / c = 0.20$, ii) High-frequency longitudinal mode at $\omega a / c = 2.30$, iii) One of the degenerate TEM modes at $\omega a / c = 2.32$. The modes are marked with green stars in panel (b).

Note that in this example ω is less than the effective plasma frequency for mesh *B* ($\omega_{p,ef}^{B} \approx 1.93c/a$), but greater than the effective plasma frequency for mesh *A* ($\omega_{p,ef}^{A} \approx 1.06c/a$). Even though the mesh *A* supports propagating modes, the transmission level is negligible

because of the large incidence angle. Indeed, a standard metallic mesh typically blocks very effectively the incoming radiation for grazing incidence, even when the frequency is larger than the effective plasma frequency.

III.3 Interlaced Wire Meshes – Light Tunneling

III.3.1 Photonic band diagram

Figure 3.3b shows the photonic band diagram of the interlaced wire meshes obtained using the eigenmode solver of CST Microwave Studio [22]. For simplicity, we only provide results for the case where the wave vector is directed along the ΓX direction. Each wire mesh is formed by a 3D array of connected metallic wires with lattice constant *a* (Fig. 3.3a). The two wire meshes (*A* and *B*) are disconnected and separated by a distance of $a/2$ along the directions parallel to the coordinate axes (see the inset of Fig. 3.3b). The wires are assumed perfect electric conductors (PEC). The host dielectric is air ($\varepsilon_h = 1$) and the radii of the wires is $r_{w,A} = 0.001a$ for mesh A and $r_{w,B} = 0.05a$ for mesh B.

Strikingly, Fig. 3.3b shows that the interlaced wire medium supports an electromagnetic mode for arbitrarily low frequencies. In contrast, it was shown in section III.2 that the individual meshes *A* and *B* do not support light states in the long wavelength regime. The emergence of low frequency modes in metallic wire arrays with disconnected components was noticed in several previous works [4-7,18,23], and in particular Ref. [23] demonstrated that the number of modes supported by a generic 3D wire mesh with N metallic components is identical to $N-1$. Importantly, as shown in Fig. 3.3c*i*, the low-frequency mode supported by the interlaced wire

medium is longitudinal such that on average the electric field has the same orientation as the wave vector $\mathbf{k}$ [23]. The interlaced wire medium also supports three high frequency modes, specifically two degenerate transverse electromagnetic (TEM) modes and an additional longitudinal mode. The field profiles of these modes are shown in Figs. 3.3c*iii* and 3.3c*ii*, respectively. The high frequency modes only propagate above an effective plasma frequency given by $\omega_{p,ef} \approx 2.3c/a$, and their dispersion and polarization is consistent with what is expected of a (spatially-dispersive) 3D electron gas [18].

III.3.2 Light Tunneling Anomaly

From the previous subsection we see clearly that the coupling between the two wire meshes leads to the emergence of a longitudinal propagating state in the low frequency limit. Can however this mode be excited by an incoming plane wave propagating in air? To answer this question, we used CST Microwave Studio to find the reflection and transmission coefficients for an incident plane wave with magnetic field directed along *x* (transverse magnetic – TM – polarization) as a function of the incidence angle. The plane of incidence is the *yoz* plane and the geometry of scattering problem is as sketched in the inset of Fig. 3.4a.

The normalized frequency is $\omega a/c = 1.32$ and the thickness of the interlaced wire medium slab is $L \approx 6a$. Counterintuitively, the full wave simulations (discrete green symbols in Fig. 3.4a) reveal that the transmission level increases with the incidence angle. Furthermore, startlingly, there is sharp transmission peak near $\theta^{\text{inc}} = 80^{\text{o}}$, corresponding to an anomalous light tunneling through the metal wire meshes. As shown in Sect III.2, the individual metallic meshes block very

effectively the incoming radiation at the same frequency.

III.4 Interlaced Wire Meshes - Theoretical Approach And Validation

Next we introduce the analytical model that uncovers the physical mechanisms underlying the light tunneling anomaly. Let us consider a periodic array with a finite length of two interlaced disconnected metal meshes A and B with lattice constant a. Each independent component by itself is an isotropic connected wire mesh in full three dimensions (Fig 3.3a). The host dielectric is air and the radii of the wires in each mesh is $r_{w,\mathrm{i}}\big|_{i=(A,B)}$.

III.2.1 Effective medium response

Next we characterize the effective medium response of the interlaced wire medium. Following Refs. [3,18,24], for long wavelengths a 3D metallic network can be modeled as an effective medium with dielectric function of equation (3.1), where $\varepsilon_t(\omega)$ is the transverse permittivity and $\varepsilon_l(\omega,k)$ is the longitudinal permittivity. The dielectric function depends explicitly on the wave vector $\mathbf{k} = -i\nabla$, and hence the effective medium response is spatially dispersive. Evidently, the dielectric function has contributions from both networks *A* and *B*. Under the hypothesis that the two networks interact with one another as homogenized media, the two contributions can be additively combined [8,18,24]; i.e. the dielectric function is the sum of two terms: each associated with a different sublattice; the two terms have different dependences on the wave vector. This approximation is more accurate when the physical distance between the two networks is larger; in this study the distance between the networks is the largest possible ($a/2$). Then, from Ref. [3 - Eq. (32)] it is possible to write (supposing

without loss of generality that the host medium is air):

$$\varepsilon_t(\omega) = 1 + \sum_{i=A,B} \left(\frac{1}{\varepsilon_{m,i} - 1} \frac{1}{f_{V,i}} - \frac{\omega^2}{c^2 k_{p,i}^2} \right)^{-1} ; \quad (i = A, B), \tag{3.3a}$$

$$\varepsilon_l(\omega, k) = 1 + \sum_{i=A,B} \left(\frac{k^2}{l_{0,i} k_{p,i}^2} + \frac{1}{\varepsilon_{m,i} - 1} \frac{1}{f_{V,i}} - \frac{\omega^2}{c^2 k_{p,i}^2} \right)^{-1} ; \quad (i = A, B). \tag{3.3b}$$

In the above, $\varepsilon_{m,i} = \varepsilon_{m,i}(\omega)$ (*i=A,B*) is the relative permittivity of the metal for the *i*-th wire mesh.

It is relevant to point out that, provided the meshes are not identical (e.g., if the wire radii are different), the two sub-lattices are not "blended" in the homogenization model. Indeed, in such a case the effective dielectric function [Eq. 3.3a] is the sum of two terms with different dependences on the wave vector. This property allows the two components of the structure to be distinguished in the homogenization model, and we will make use of this feature when enforcing boundary conditions. Thus, the distinction of the two sublattices in the homogenization framework is always possible, except if the two meshes are identical. In such a case, the effective medium does not predict the tunneling phenomenon. Indeed, as we will discuss, the symmetry between the two lattices needs to be broken to excite the Fano resonance.

III.4.2 Dispersion Diagram

The dispersion of the transverse (TEM) modes is determined by $k^2 = (\omega/c)^2 \varepsilon_t(\omega)$. The TEM modes are doubly degenerate and have electromagnetic fields perpendicular to the wave

vector. In the particular case of PEC wires ($\varepsilon_{m,i} = -\infty$) the TEM modes only propagate above the plasma frequency $\omega_{p,ef} = c\sqrt{k_{p,A}^2 + k_{p,B}^2}$, which is thereby larger than the plasma frequencies of the individual wire networks ($\omega_{p,i} = ck_{p,i}$, *i=A,B*). This is consistent with the heuristic idea that the interlaced wire meshes block more effectively the radiation than each individual wire network on its own. On the other hand, the longitudinal waves have a vanishing magnetic field and electric field directed along the wave vector. The dispersion of the longitudinal modes is determined by $\varepsilon_l(\omega,k) = 0$, and, provided the two networks are different (e.g., if $r_{w,A} \neq r_{w,B}$), it can be reduced to a quadratic polynomial equation in the variable k^2. This means that the interlaced wire medium supports *two* longitudinal modes. Figure 3.3b shows that on the overall there is a good agreement between the analytical model (solid lines) and the full wave numerical results (discrete points) (section III.3.1). Furthermore, consistent with the numerically simulated photonic band structure and with Ref. [23], one of the longitudinal modes predicted by our analytical model has no cut-off and propagates for arbitrarily low frequencies.

III.4.3 Scattering Parameters - Additional Boundary Conditions

Next, we build on ideas from previous works [3,8,9,24] and on the theory discussed above to characterize with the analytical model the scattering of an incident electromagnetic plane wave by a finite slab of the interlaced wire metamaterial with thickness L . The geometry of the problem is as sketched in the inset of figure 3.4a.

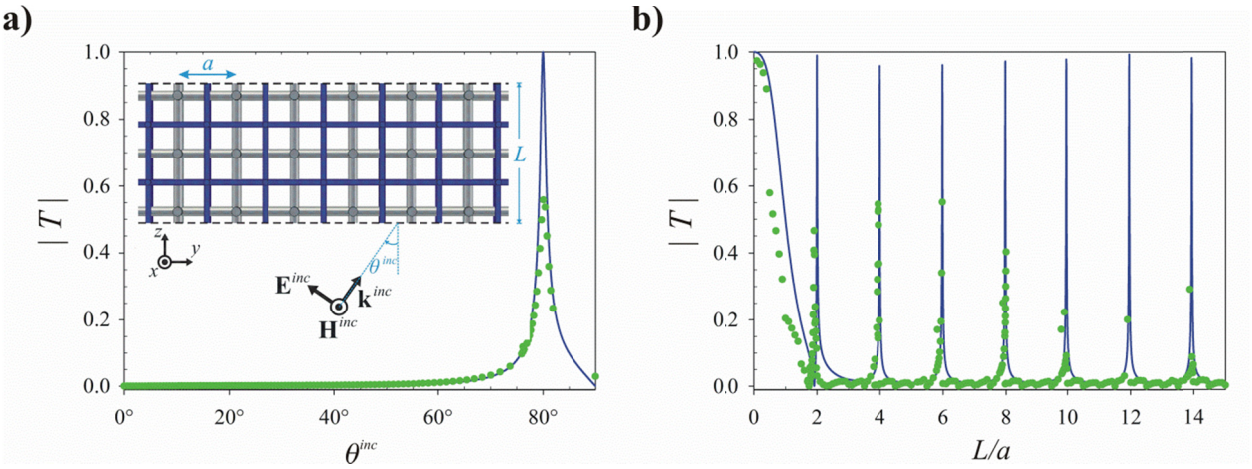

Figure 3.4: (a) Amplitude of the transmission coefficient as function of the incidence angle for the normalized frequency $\omega a / c = 1.32$ and normalized thickness $L / a \approx 6$. The remaining structural parameters are as in Fig. 3.3. (b) Amplitude of the transmission coefficient as a function of the normalized thickness for the fixed frequency $\omega a / c = 1.32$ and incidence angle 80º. The solid lines represent the analytical results, and the discrete symbols the full wave simulations results.

The total magnetic field ($\mathbf{H} = H_x \hat{\mathbf{x}}$) can be expanded in plane waves in all regions of space as follows:

$$H_x = H_0^{inc} e^{ik_y y} \times \begin{cases} e^{ik_z^0 z} + Re^{-ik_z^0 z}, & z \le 0 \\ A_T^+ e^{ik_z^{(T)} z} + A_T^- e^{-ik_z^{(T)} z}, & 0 \le z \le L \\ Te^{ik_z^0 (z-L)}, & z \ge L \end{cases}, \tag{3.4}$$

where H_0^{inc} is the complex amplitude of the incident wave, R and T are the reflection and transmission coefficients, $A_T^{\pm}$ are the unknown amplitudes of the transverse mode in the wire medium, and $k_z^{(T)} = \sqrt{(\omega / c)^2 \varepsilon_t(\omega) - k_y^2}$ is the propagation constant along *z* of the transverse wave in the wire medium. The incident wave vector is $\mathbf{k}_0^+ = k_y \hat{\mathbf{y}} + k_z^0 \hat{\mathbf{z}}$ with $k_y = (\omega / c) \sin\theta^{inc}$ and $k_z^0 = \sqrt{(\omega / c)^2 - k_y^2}$. Note that the longitudinal modes have a vanishing magnetic field, and hence $\mathbf{H}$ depends only on the transverse mode in the interlaced wire medium.

In contrast, the electric field depends on both the transverse and longitudinal fields inside the wire medium and is given by,

$$\mathbf{E}=\frac{H_0^{inc}}{\omega\varepsilon_0}e^{ik_y y}\times\begin{cases}\hat{\mathbf{x}}\times\mathbf{k}_0^{+}e^{ik_z^0 z}+\hat{\mathbf{x}}\times\mathbf{k}_0^{-}R\,e^{-ik_z^0 z}, & z\le 0\\ \sum\limits_{\pm}\left(B_{L,1}^{\pm}\mathbf{k}_{L,1}^{\pm}e^{\pm ik_z^{(L,1)}z}+B_{L,2}^{\pm}\mathbf{k}_{L,2}^{\pm}e^{\pm ik_z^{(L,2)}z}+\frac{1}{\varepsilon_t}\hat{\mathbf{x}}\times\mathbf{k}_T^{\pm}A_T^{\pm}e^{\pm ik_z^{(T)}z}\right), & 0\le z\le L\\ \hat{\mathbf{x}}\times\mathbf{k}_0^{+}T\,e^{ik_z^0(z-L)}, & z\ge L\end{cases}, \qquad (3.5)$$

where $k_z^{(L,j)}$ (j=1,2) are the z-propagation constants of the two longitudinal modes (which are found by solving $\varepsilon_l(\omega,k)=0$ with respect to k_z) and $B_{L,j}^{\pm}$ (j=1,2) are the unknown complex amplitudes of the longitudinal modes for the $\pm$ directions of propagation with respect to the z-axis. Furthermore, we defined $\mathbf{k}_0^{\pm}=k_y\hat{\mathbf{y}}\pm k_z^0\hat{\mathbf{z}}$, $\mathbf{k}_T^{\pm}=k_y\hat{\mathbf{y}}\pm k_z^{(T)}\hat{\mathbf{z}}$ and $\mathbf{k}_{L,j}^{\pm}=k_y\hat{\mathbf{y}}\pm k_z^{(L,j)}\hat{\mathbf{z}}$. Note that the transverse part of the electric field can be obtained from the magnetic field using $\mathbf{E}_T=\frac{1}{-i\omega\varepsilon_0\varepsilon_t}\nabla\times\mathbf{H}$.

The unknown coefficients (R, T, $A_T^{\pm}$, $B_{L,j}^{\pm}$) are found by imposing suitable boundary conditions at the $z=0$ and $z=L$ interfaces. As usual, we require the continuity of the tangential electromagnetic fields (H_x and E_y) at the interfaces. However, due to the nonlocal response of the interlaced wire medium, these Maxwellian boundary conditions are insufficient to determine all the unknowns and therefore one needs to enforce additional boundary conditions (ABCs) [3,9 ,24-27]. The standard (Pekar) ABC for a nonlocal plasma imposes that the normal component of the polarization current due to the drift charges ($-i\omega P_z$) vanishes at the interfaces [3,28-30]. As shown in previous works [6,8-9], this ABC can be extended to different

types of wire media with multiple disconnected components. The idea is that the currents flowing in the individual meshes (here *A* and *B*) are independent, and therefore it is required that the contribution of each mesh to the polarization vector vanishes *separately* at the interfaces:

$$P_{z,i}=0, \qquad (i=A,B) \qquad \text{at } z=0 \text{ and } z=L. \tag{3.6}$$

The polarization vector associated with the *l*-th wire mesh (*l*=*A*,*B*) is $\mathbf{P}_l=\left(\bar{\varepsilon}_l-\varepsilon_0\mathbf{1}\right)\cdot\mathbf{E}$, $\bar{\varepsilon}_l=\bar{\varepsilon}_l\left(\omega,-i\nabla\right)$ being the dielectric function of the *l*-th wire mesh alone. The dielectric function $\bar{\varepsilon}_l$ is defined as in Eq. (3.1). Straightforward calculations show that $P_{z,i}$ can be explicitly written as follows:

$$P_{z,i}=\frac{H_0^{inc}}{\omega}e^{ik_y y}\sum_{\pm}\left(\pm k_z^{(L,1)}\left(\varepsilon_{l,i}^{(1)}-1\right)B_{L,1}^{\pm}e^{\pm ik_z^{(L,1)}z}\pm k_z^{(L,2)}\left(\varepsilon_{l,i}^{(2)}-1\right)B_{L,2}^{\pm}e^{\pm ik_z^{(L,2)}z}+\frac{\varepsilon_{t,i}-1}{\varepsilon_t}k_y A_T^{\pm}e^{\pm ik_z^{(T)}z}\right) \tag{3.7}$$

In the above, $\varepsilon_{t,i}\left(\omega\right)=1+\left(\frac{1}{\varepsilon_{m,i}-1}\frac{1}{f_{V,i}}-\frac{\omega^2}{c^2k_{p,i}^2}\right)^{-1}$ is the transverse permittivity of the *i*-th mesh and $\varepsilon_{l,i}^{(j)}=1+\left(\frac{\left|\mathbf{k}_{L,j}\right|^2}{l_{0,i}k_{p,i}^2}+\frac{1}{\varepsilon_{m,i}-1}\frac{1}{f_{V,i}}-\frac{\omega^2}{c^2k_{p,i}^2}\right)^{-1}$ is the corresponding longitudinal permittivity (*i*=*A*,*B*, *j*=1,2). In summary, the transmission and reflection coefficients can be found with the effective medium formalism by imposing the continuity of the tangential fields and two ABCs [Eq. 3.6] per interface.

III.4.4 Transmission properties – Numerical Results

Validation of the effective medium

Using the outlined formalism, we calculated the transmission coefficient as a function of the incidence angle for the example discussed earlier. As shown in Fig. 3.4a, there is a truly remarkable agreement between the analytical model (solid line) and the CST full wave simulations. Figure 3.4b shows the transmission coefficient as function of the normalized thickness (L/a) for $\omega a/c = 1.32$. The analytical results (solid line) follow closely the full wave simulations (discrete symbols), which further validates our effective medium model and confirms the anomalous light tunneling. There are multiple transmission resonances, even for thicknesses as large as $L/a \sim 10$. The position of the transmission peaks is accurately predicted by the analytical model.

Impact of loss

To study the impact of metallic loss on the tunneling anomaly, it is supposed next that the wires have a finite conductivity σ_i (*i=A,B*) and that the lattice constant is $a = 1\,\mathrm{mm}$. Thus, the metal complex permittivity is taken equal to $\varepsilon_{m,i} = 1 + \sigma_i / \left(-i\omega\varepsilon_0\right)$. In general, the effect of metallic loss in the wire networks is negligible provided the radius of the wires is a few times larger than the skin depth of the metal (δ) (which is on the order of the μm at microwaves). This property was verified in many studies, see for example [31]. Figures 3.5a and 3.5b show the amplitude of the transmission coefficient for different values of the conductivity σ_B of the wires in mesh B, considering that the wires in mesh A are perfect conductors ($\sigma_A = \infty$). For the

copper case ($\sigma_{B,\mathrm{Cu}} = 5.96\times10^{7}\,\mathrm{Sm}^{-1}$) the loss effects are negligible, which is expected because the metal skin depth at the considered frequency ($\delta_B = \sqrt{2/(\omega\mu_0\sigma_B)} = 0.26\,\mu\mathrm{m}$) is much smaller than the corresponding wire radius $r_{w,B} = 0.05\,\mathrm{mm}$. For the conductivity $\sigma_B = 10^{3}\,\mathrm{Sm}^{-1}$ ($\delta_B = 0.06\,\mathrm{mm}$), the transmission peaks are evidently damped because a significant fraction of the fields energy can penetrate inside the lossy metal. The transmission level remains significant if $r_{w,i} >> \delta_i$, even when both wire meshes have a finite conductivity. This is illustrated in Fig. 3.5c for the case of copper wires and a lattice period $a = 1\mathrm{cm}$. Note that mesh *A* (with the thinner wires) is more sensitive to the effect of loss.

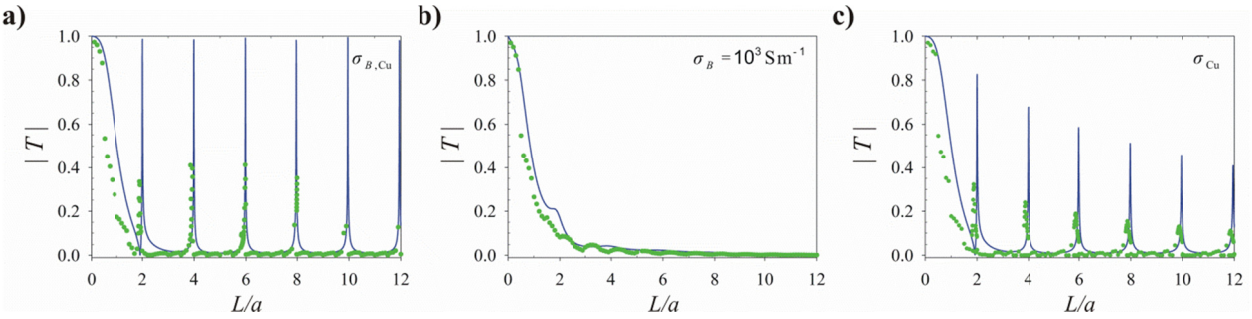

Figure 3.5: (a) and (b) Similar to Fig. 3.4(b) considering that the wires in mesh B have a finite conductivity and $a = 1\mathrm{mm}$. (c) Similar to (a) considering that the wires in both meshes are made of copper and $a = 1\mathrm{cm}$. In all the panels the solid lines represent the analytical results, and the discrete symbols the full wave simulations results.

III.5 Origin of the Tunneling Effect

III.5.1 FP resonance of the propagating longitudinal mode

Figure 3.6a shows a density plot of the transmission coefficient as a function of *L* and θ^{inc} for PEC wires and $\omega a/c = 1.32$. The density plot exhibits multiple sharp bright lines. The transmission is typically negligible for small angles; in fact, for normal incidence the propagating longitudinal mode cannot be excited. The transmission level becomes stronger for large

incidence angles (grazing incidence) and for specific values of the thickness.

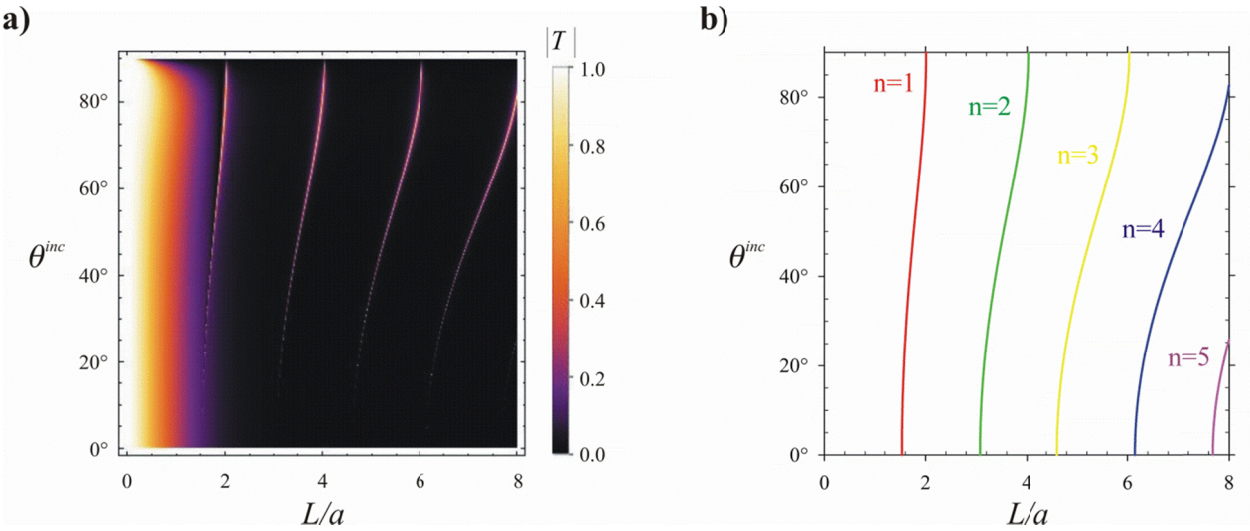

Figure 3.6: (a) Density plot of the transmission coefficient amplitude as a function of the normalized thickness L/a and of the incidence angle θ^{inc} at the fixed frequency of $\omega a/c = 1.32$. (b) Incidence angle θ^{inc} as a function of L/a for the n-th (n=1,2,…) Fabry-Pérot resonance of the propagating longitudinal mode at $\omega a/c = 1.32$.

To understand the origin of the sharp lines, we investigated the Fabry-Pérot (FP) condition for the propagating longitudinal mode ($k_z^{(L,1)} L = n\pi,\ n = 1,2,3,\ldots$). Figure 3.6b represents the combination of parameters L and θ^{inc} required to have a FP resonance of order *n* for a fixed ω. Note that for a fixed frequency, the propagation constant $k_z^{(L,1)}$ is a function of the incidence angle. As seen, there is an obvious coincidence between the FP-resonance lines in Fig. 3.6b and the sharp bright lines in Fig. 3.6a. This clearly proves that the tunneling anomaly is due to a FP resonance of the propagating longitudinal mode.

Figure 3.7 shows results analogous to Fig. 3.6, but for a fixed slab thickness ($L/a \approx 6$) and for varying frequency and incidence angle. The density plot of Fig. 3.7a is characterized by multiple sharp lines, which are especially "bright" for large incidence angles. Figure 3.7b

identifies the combinations of parameters $\omega a / c$ and θ^{inc} associated with a *n*-th order FP resonance of the propagating longitudinal mode. Again, there is a precise matching between the FP-resonance lines in Fig. 3.7b and the sharp bright lines in Fig. 3.7a.

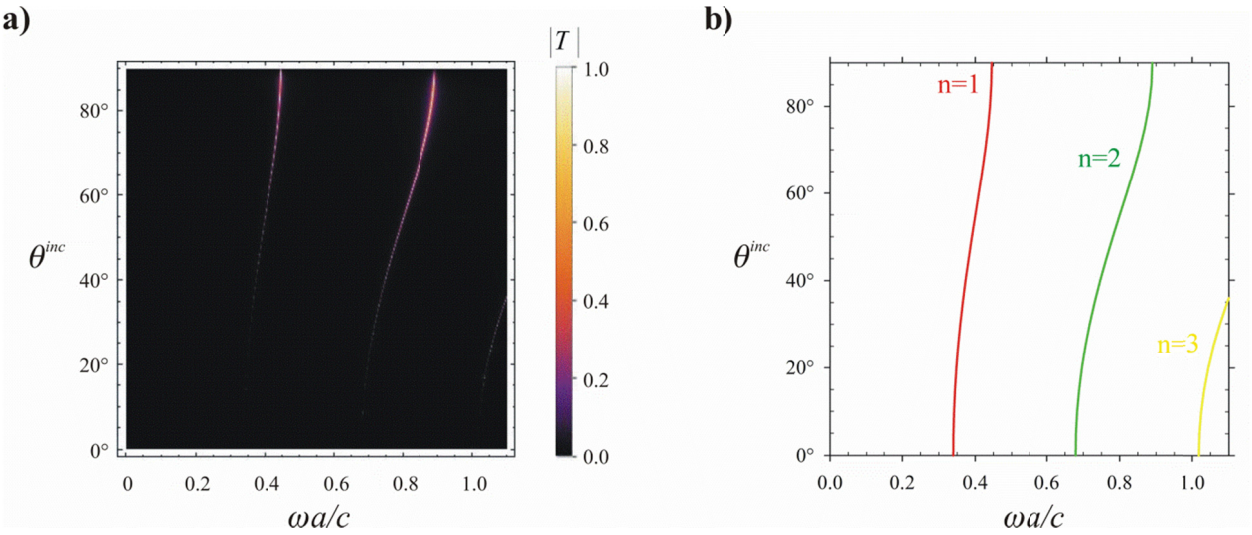

Figure 3.7. (a) Density plot of the transmission coefficient amplitude as a function of the normalized frequency $\omega a / c$ and of the incidence angle θ^{inc} for the fixed slab thickness $L / a \approx 6$. (b) Incidence angle θ^{inc} as a function of the normalized frequency $\omega a / c$ for the nth (n=1,2,…) Fabry-Pérot resonance of the propagating longitudinal mode and $L / a \approx 6$.

Moreover, the results of Fig. 3.7 reveal that the tunneling anomaly can in principle occur for extremely long wavelengths ($\omega a / c << 1$). Indeed, for grazing incidence and for the considered wire radii, the first resonance occurs for $\omega L / c \sim 2.6$, approximately independent of the value of L / a.

III.5.2 Macroscopic polarization

Figure 3.8 depicts the profiles of the polarization currents in each wire mesh ($P_{z,A}$ and $P_{z,B}$) obtained with the effective medium model [see Eq. 3.7] for the first two peaks of the transmission coefficient in Fig. 3.4b. As expected, the field profiles are consistent with FP

resonances of 1st and 2nd order, as well as with full wave simulations of the electric current density (see Figs. 3.8a*ii* and 3.8b*ii*).

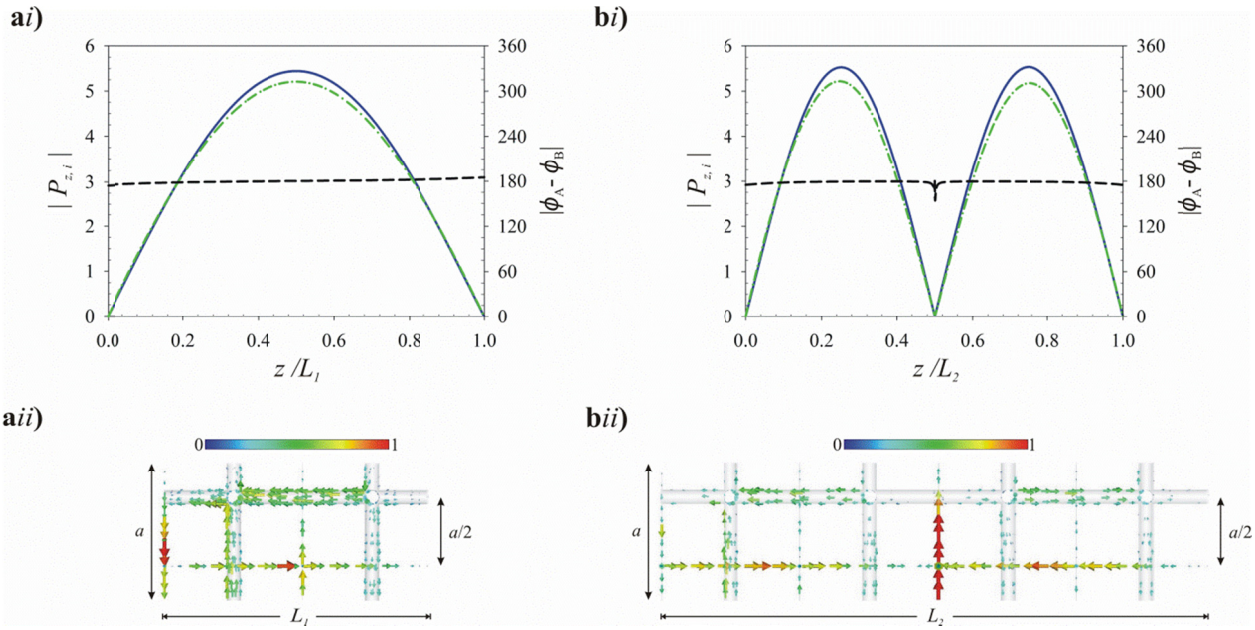

Figure 3.8: (ai, bi) Phase difference (black dashed lines) and normalized amplitude (blue and green lines) of the z-component of the macroscopic polarization $P_{z,A}$ and $P_{z,B}$ [Eq. 3.7] associated with the wire meshes A and B for ai) the 1st FP resonance ($L/a \approx 2$) and bi) the 2nd FP resonance ($L/a \approx 4$). The solid blue (dot-dashed green) lines represent the contribution from the wire mesh A (wire mesh B). The normalized frequency is $\omega a/c = 1.32$ and the incidence angle is 80º. The remaining simulation parameters are as in Fig. 3.4b). (aii, bii) Full wave simulation results of the microscopic current density for the scenarios ai) (1st FP resonance) and bi) (2nd FP resonance), respectively.

However, the most remarkable thing in Fig. 3.8 is that it reveals that at the transmission resonances the polarization vectors $P_{z,A}$ and $P_{z,B}$, and thereby the currents in the *A* and *B* meshes, have nearly identical amplitudes and are phase-shifted by 180º ($\phi_A - \phi_B = 180^\circ$). Thus, the tunneling anomaly is made possible by a *destructive interference* of the fields radiated by the two wire meshes. Indeed, for long wavelengths the scattering by the interlaced wire medium is typically dominated by a strongly radiative dipolar mode (bright mode) due to the in-phase interference of the fields scattered by the two wire meshes. This mode typically

determines the overall scattering of the structure. In particular, for low frequencies it creates a scattered wave that cancels out the incoming wave in the direction of propagation, leading to a near-zero transmission. Crucially, because of the structural asymmetry of the interlaced wire medium ($r_{w,A} \neq r_{w,B}$) the currents excited in meshes *A* and *B* may be different. This enables the formation of a narrow anti-bonding mode (dark mode), such that the current in one of the meshes flips sign for a narrow range of incident angles leading to a sub-radiant regime; i.e. the "dark mode" corresponds to a wave oscillation with the currents in the two sublattices in opposition of phase. Such a dark mode has a precise resonant frequency determined by the Fabry-Pérot condition of the longitudinal mode, and it is therefore inherently a discrete state. The excitation of the dark mode originates the transmission peaks. Thus, the physical origin of the tunneling anomaly is a Fano-type resonance [8,20,21,32] that enables the *cancellation of the scattering* by the two subcomponents of the interlaced wire medium. Remarkably, in our system the two scatterers (i.e. the wire meshes) that create the Fano resonance are infinitely extended in space. Hence, we provide a rather unique example of scattering cancellation based on the interference of two infinitely extended opaque objects.

Note that the original meaning of Fano-resonance phenomenon is related to an interference between a discrete state interacting with a continuum. This original meaning is applicable to our present situation; In fact, the interlaced wire mesh supports two modes: a "bright mode" that couples strongly to the radiation continuum, and a "dark mode" that couples weakly to the radiation continuum, similar to Ugo Fano's original article. The "bright mode" is inherently delocalized in space (the scattered waves are delocalized) and can be

excited in a broad range of frequencies/energies (because the background states form a continuum, i.e. exist for all the frequencies/energies). In contrast, the "dark-state" is strongly localized at the scatterer. It has a high quality factor, and is rooted in a discrete bound-type state of the scatterer.

III.6 Conclusions

In summary, we theoretically predict the counterintuitive effect of light tunneling due to the destructive interference of the scattering by two interlaced 3D wire meshes. The effect is rooted in a sub-radiant Fano-type resonance and was explained with an effective medium theory that models the interlaced wire medium as a spatially dispersive continuum. It was shown that the transmission peaks correspond to FP resonances of a longitudinal propagating mode supported by the metamaterial. It is underlined that the longitudinal mode can be excited by a (slowly varying in space) plane wave only due to the structural asymmetry of the wire meshes. The structural asymmetry is mandatory in order that the currents in the two wire meshes can be 180º out of phase. Since the transmission peaks are very sensitive to changes of the incidence angle, frequency and of other structural parameters, the interlaced wire medium may find interesting applications in sensing and angular filtering.

References

[1] J. B. Pendry, A. J. Holden, W. J. Stewart and I. Youngs, "Extremely Low Frequency Plasmons in Metallic Mesostructures", *Phys. Rev. Lett.,* **76**, 4773, 1996.

[2] D. F. Sievenpiper, M. E. Sickmiller and E. Yablonovitch, "3D Wire Mesh Photonic Crystals", *Phys. Rev. Lett.*, **76**, 2480, 1996.

[3] M. G. Silveirinha, "Artificial plasma formed by connected metallic wires at infrared frequencies", *Phys. Rev. B*, **79**, 035118, 2009.

[4] M. G. Silveirinha, C. A. Fernandes, "Nonresonant structured material with extreme effective parameters", *Phys. Rev. B*, **78**, 033108, 2008.

[5] M. G. Silveirinha, C. A. Fernandes, J. R. Costa, "Superlens made of a metamaterial with extreme effective parameters", *Phys. Rev. B*, **78**, 195121, 2008.

[6] M. G. Silveirinha, "Broadband Negative Refraction with a Crossed Wire Mesh", *Phys. Rev. B*, **79**, 153109, 2009.

[7] M. G. Silveirinha, "Anomalous dispersion of light colors by a metamaterial prism", *Phys. Rev. Lett.*, **102**, 193903, 2009.

[8] D. E. Fernandes, S. I. Maslovski, G. W. Hanson, M. G. Silveirinha, "Fano resonances in nested wire media", *Phys. Rev. B*, **88**, 045130, 2013.

[9] M. G. Silveirinha, "Additional boundary conditions for nonconnected wire media", *New. J. Phys.*, **11**, 113016, 2009.

[10] W. Rotman, "Plasma simulation by artificial dielectrics and parallel-plate media", *IRE Trans. Antennas Propag.*, **10**, 82–84, 1962.

[11] P. A. Belov, S. A. Tretyakov, and A. J. Viitanen "Dispersion and reflection properties of artificial media formed by regular lattices of ideally conducting wires", *J. of Electromagn. Waves and Appl.*, **16**, 1153–1170, 2002.

[12] P. A. Belov, R. Marqués, S. I. Maslovski, I. S. Nefedov, M. Silveirinha, C. R. Simovsky and S. A. Tretyakov, "Strong spatial dispersion in wire media in the very large wavelength limit," *Phys. Rev. B*, **67**, 113103, 2003.

[13] M. G. Silveirinha, "Nonlocal homogenization model for a periodic array of epsilon-negative rods", *Phys. Rev. E*, **73**, 046612, 2006.

[14] S. I. Maslovski, M. G. Silveirinha, "Nonlocal permittivity from a quasistatic model for a class of wire media", *Phys. Rev. B*, **80**, 245101, 2009.

[15] C. R. Simovski, P. A. Belov, A. V. Atrashchenko, Y. S. Kivshar, "Wire metamaterials: physics and applications", *Adv. Mater.*, **24**, 4229-4248, 2012.

[16] R. Petit (Ed), *Electromagnetic Theory of Gratings* (Topics in Current Physics book series Vol. 22), Springer, Berlin, 1980.

[17] R. Ulrich, "Interference filters for the far infrared", *Appl. Opt.*, **7**(10):1987, 1968.

[18] M. G. Silveirinha and C. A. Fernandes, "Homogenization of 3-D-Connected and Nonconnected Wire Metamaterials", *IEEE Trans. on Microw. Theory and Techn.*, **53**, 1418, 2005.

[19] A. Demetriadou and J. B. Pendry, "Taming spatial dispersion in wire metamaterial", *J. Phys.: Condens. Matter*, **20**, 295222, (1–11), 2008.

[20] U. Fano, "Effects of Configuration Interaction on Intensities and Phase Shifts", *Phys. Rev.*, **124**, 1866, 1961.

[21] A. E. Miroshnickenko, S. Flach, and Y. S. Kivshar, "Fano resonances in nanoscale

structures", *Rev. Mod. Phys.*, **82**, 2257, 2010.

[22] CST Microwave Studio 2016 (http://www.cst.com).

[23] J. Shin, J.-T. Shen and S. Fan, "Three-dimensional electromagnetic metamaterials that homogenize to uniform non-Maxwellian media", *Phys. Rev B*, **76**, 113101, 2007.

[24] G. W. Hanson, E. Forati, and M. G. Silveirinha, "Modeling of spatially-dispersive wire media: transport representation, comparison with natural materials, and additional boundary conditions", *IEEE Trans. on Antennas and Propagat.*, **60**, 4219, 2012.

[25] M. G. Silveirinha "Additional boundary condition for the wire medium", *IEEE Trans. Antennas Propag.*, **54**, 1766–1780, 2006.

[26] M. G. Silveirinha, C. A. Fernandes and J. R. Costa "Additional boundary condition for a wire medium connected to a metallic surface", *New J. Phys.*, **10**, 053011, 2008.

[27] S. I. Maslovski, T.A. Morgado, M. G. Silveirinha, C. S. R. Kaipa, A. B. Yakovlev, "Generalized additional boundary conditions for wire media", *New J. Phys.*, **12**, 113047, 2010.

[28] S. I. Pekar, "The Theory of Electromagnetic Waves in a Crystal in which Excitons Are Produced", *Zh. Eksp. Teor Fiz*, **33**, 1022, 1957 [*Sov. Phys. JETP* **6**, 785 (1958)].

[29] A. R. Melnyk and M. J. Harrison, "Theory of optical excitation of plasmons in metals," *Phys. Rev. B*, **2**, 835, 1970.

[30] M. Anderegg, B. Feuerbacher, and B. Fitton, "Optically excited longitudinal plasmons in Potassium," *Phys. Rev. Lett.*, **27**, 1565, 1971.

[31] M. G. Silveirinha, P. A. Belov, and C. R. Simovski, "Ultimate limit of resolution of subwavelength imaging devices formed by metallic rods", *Opt. Lett.*, **33**, 1726, 2008.

[32] B. Luk'yanchuk, N. I. Zheludev, S. A. Maier, N. J. Halas, P. Nordlander, H. Giessen and C. T. Chong, "The Fano resonance in plasmonic nanostructures and metamaterials", *Nat. Mater.* **9**, 707, 2010.

CHAPTER 4 :

Topological light tunneling in a two-phase metamaterial

IV. Topological Light Tunneling in a Two-phase Metamaterial

IV.1 Introduction

Nonreciprocal effects in electromagnetics and nonreciprocal optical platforms have been recently the object of renewed interest and scrutiny, due to their unique and singular properties [1-12]. In particular, nonreciprocal systems enable one-way light flows and optical isolation [2-4, 8-12]. Nonreciprocal effects are typically obtained by tailoring the permittivity or permeability response with a static magnetic field, but alternative solutions have been explored recently [6-8, 10-11, 13-14].

Remarkably, some nonreciprocal systems may have a topological nature [15-21]. Such systems are characterized by a topological integer that determines the number of topologically protected chiral edge states: the "Chern number". Indeed, the topology of a material can have remarkable consequences in the context of the electromagnetic propagation: when a topological material is paired with another material with a trivial topology, unidirectional scattering-immune gapless edge states emerge in a common bulk bandgap, a result known as the "the bulk edge correspondence" principle [18, 19, 21, 22]. Furthermore, it was recently shown that the photonic Chern number has a precise physical meaning: it is the quantum of the light-angular momentum spectral density in a photonic insulator cavity [22, 23].

Building on these previous works, here we theoretically and numerically demonstrate that topological edge modes (magneto-plasmons) may enable an anomalous "transparency effect" in a composite material formed by two topologically distinct fully-reflecting phases. We argue that by mixing two distinct topological material phases it is possible to obtain a material

response that enables an anomalous "transparency effect" in a spectral range wherein the individual material phases are strongly reflecting. In particular, we discuss how such an effect may be directly observed in naturally available materials and, in addition, we propose a realistic physical implementation of the structure based on the metamaterial concept, we show that a metamaterial formed by a metallic wire grid embedded in a magnetized plasma may support the propagation of waves with long wavelengths, notwithstanding the components, when taken separately, block completely the electromagnetic radiation. The effect is explained in terms of the topological properties of the magnetoplasmon. Furthermore, it is highlighted that some naturally available materials may be regarded as a mixture of two topologically distinct phases, and hence may be as well characterized by a similar anomalous transparency effect.

The chapter is organized as follows. In section IV.2, we briefly introduce some basic concepts used in this chapter. In section IV.3 the two phase topological metamaterial is introduced. In section IV.5 the transmission properties of the proposed topological metamaterial are examined. In section IV.4, we propose a realistic physical implementation of the structure. The conclusions are drawn in section IV.5. It is assumed that the electromagnetic fields have a time dependence of the form $e^{-i\omega t}$.

IV.2 Review of basic concepts

The main goal of this section is to provide some theoretical background of gyrotropy, non-reciprocity and topological media.

IV.2.1 Gyrotropic and non-reciprocal media

The word gyrotropy comes from the Greek word gyro meaning rotate so that the polarization plane of the electromagnetic wave rotates as it propagates [24]. Gyrotropic media have attracted interest for a long time, traced back to 1950s and 1960s when the majority studies dealt with the wave propagation in magnetically biased plasma or ferrite type waveguides [25–36]. This is justified by the existence of natural gyrotropic crystals, which ease the realization of artificial composites with a gyrotropic response based on natural mechanisms, e.g., magnetically biased plasma (or ferrite). Ferromagnetic resonance (FMR) [37] is one of the mechanisms that leads to a strong gyrotropic effect: it requires a bias magnetic field on the order of tenth of the Tesla, but is limited to the GHz frequency range. Magnetized plasmas [3] provide gyrotropic response at low optical frequencies, but with a biasing field of several Tesla. A magnetized plasma with a bias magnetic field along the +*z*-axis is characterized by a permittivity tensor of the form $\bar{\varepsilon} = \varepsilon_t \mathbf{1}_t + \varepsilon_a \hat{\mathbf{z}} \otimes \hat{\mathbf{z}} + i\varepsilon_g \hat{\mathbf{z}} \times \mathbf{1}$ ($\mathbf{1}_t = \mathbf{1} - \hat{\mathbf{z}} \otimes \hat{\mathbf{z}}$) with the permittivity elements in the lossless approximation,

$$\varepsilon_t = 1 - \frac{\omega_p^2}{\omega^2 - \omega_c^2}, \qquad \varepsilon_a = 1 - \frac{\omega_p^2}{\omega^2} \qquad \text{and} \qquad \varepsilon_g = \frac{1}{\omega} \frac{\omega_p^2 \omega_c}{\omega_c^2 - \omega^2} \tag{4.1}$$

where ω_p and ω_c are the plasma and cyclotron frequencies, respectively.

A magnetized plasma is a non-reciprocal medium. A nonreciprocal system cannot return back to its original state when the time is reversed. Thus, non-reciprocal systems have a broken the time-reversal symmetry. Besides the magnetized plasma, other examples of nonreciprocal structures are antiferromagnets, magnetized ferrites or magnetized graphene. A linearly

polarized wave propagating in a gyrotropic medium experiences a polarization rotation: the Faraday effect. This effect is exploited to realize optical isolators, i.e., devices that allow the propagation of waves in only one direction.

IV.2.2 Topological media

Topology is a branch of mathematics that concerns the study of the global properties of an object under continuous transformations. For example, from the point of view of the conventional geometry, a sphere is different from an ellipsoid. However, these shapes can transform one into the other under smooth continuous deformation, and hence are considered in topology as equivalent. In theory of surfaces, two objects are topological equivalent if they have the same number of holes. The number of holes is called the genus. The *genus* of an object is a topological invariant since it stays the same under continuous deformation of the object; the topological invariant can change only when a hole is created or removed in the object. This process is a *topological phase transition*. Objects with the same number of holes, e.g. a sphere and an ellipsoid, are identified as being topologically equivalent: they are in the same *topological phase*. In contrast, objects possessing different genus, e.g. a torus (with one hole) and a sphere, are said to be topologically inequivalent and belong to different topological classes requiring a drastic change of some sort to go from one topological class to the other one. The genus [39] of an object provides a simple example which allows for the straightforward determination of the topological invariant without complicated mathematical calculations.

The field of topology concerns many more interesting and global properties that do not

change under continuous deformations (not discernible locally) and has attracted tremendous research attention in many fields of physics, ranging from condensed matter to ultra-cold gases. In particular, in photonic systems, along with the degrees of freedom that are often used in the characterization of their response (frequency, wave-vector, polarization), topology has emerged in the last few years as another indispensable ingredient [15]. The topologies of material-systems in photonics are determined by the band diagram in the wave vector space. The topological bulk invariant, specifically the Chern number, is a quantity that characterizes the quantized collective behavior of the wave functions on the band that can be directly measured for example with the proposals of Refs [40,41]. The Chern number only changes discretely; it will not be affected by continuous small perturbations of the system such as arbitrary continuous changes in the material parameters. The introduction of topology into photonics has opened up a path forward to researches on the discovery of fundamentally new states of light. Much of this research has focused on the experimental observation of topologically protected edge states in systems [16,42-46].

A hallmark insight into the physical meaning of the topological invariant is given by the *bulk-edge correspondence* [47-50]: when two distinct topological materials (i.e. with different topological invariants) are put in contact, there must appear *edge states* that are spatially *localized* at their boundary interface region at frequencies that lie within their common frequency gap. The number of edge states is completely dictated by the Chern number.

Importantly, it was previously known that one-way modes can exist on the surfaces of continuous magnetic media [3,66,51-56], but the topological origin of these modes was only

recently unveiled [20,21,57].

In the next section, we come up with a new situation in the physics of artificial topological media, and demonstrate the odd circumstance of a synthetized topological material experiencing an anomalous wave "transparency effect" in a spectral range wherein the elementary material phases are fully reflecting.

IV.3 Two-Phase topological (meta)materials

IV.3.1 Effective medium response

As a starting point, let us consider a mixture of two materials, characterized by the permittivity tensors $\bar{\varepsilon}_1$ and $\bar{\varepsilon}_2$, respectively. The effective permittivity of the mixture depends on the volume fraction of each material, on the shape of the inclusions, lattice structure, etc [58-59]. As an illustration, for now we use the simple mixing formula [60]:

$$\bar{\varepsilon} \approx \left(1-f_V\right)\bar{\varepsilon}_1 + f_V \bar{\varepsilon}_2 \tag{4.2}$$

Here, f_V is the volume fraction of the 2nd material. Furthermore, we shall focus on the case $f_V << 1$, so that $\bar{\varepsilon} \approx \bar{\varepsilon}_1 + f_V\left(\bar{\varepsilon}_2 - \mathbf{1}\right)$. Then, if 1st material has a gyrotropic response and the 2nd material is isotropic with a Drude dispersion ($\varepsilon_2 = 1-\omega_{p2}^2/\omega^2$), it follows that the composite medium is characterized by a dielectric function of the form $\bar{\varepsilon} = \varepsilon_t \mathbf{1}_t + \varepsilon_a \hat{\mathbf{z}}\otimes\hat{\mathbf{z}} + i\varepsilon_g \hat{\mathbf{z}}\times\mathbf{1}$ ($\mathbf{1}_t = \mathbf{1} - \hat{\mathbf{z}}\otimes\hat{\mathbf{z}}$) with

$$\varepsilon_t = 1 - \frac{\omega_p^2}{\omega^2-\omega_c^2} - \frac{\tilde{\omega}_p^2}{\omega^2}, \qquad \varepsilon_g = \frac{1}{\omega}\frac{\omega_p^2\omega_c}{\omega_c^2-\omega^2} \tag{4.3}$$

and $\tilde{\omega}_p = \sqrt{f_V}\omega_{p2}$. The permittivity component ε_a is not relevant in this study and hence it is not shown. When $\tilde{\omega}_p = 0$ the permittivity dispersion is coincident with that of the 1st material, which is taken as a standard magnetized plasma (with bias magnetic field, $\mathbf{B}_0 = B_0\hat{\mathbf{z}}$), e.g., it is similar to the response of magnetized semiconductors [61-62]. In such a context, ω_p is the plasma frequency of the electron gas and $\omega_c = -qB_0/m$ is the cyclotron frequency determined by the bias field ($q = -e$ is the negative charge of the electrons and *m* is the effective mass) [63]. Magnetized plasmas and other gyrotropic media are generically topologically nontrivial materials [20-21, 64-66]. On the other hand, the second material is characterized by a Drude dispersion model, ($\varepsilon_2 = 1 - \omega_{p2}^2/\omega^2$), which is reciprocal, and thus is topologically trivial. Hence, the global permittivity (4.3) models a composite formed by mixing two different topological phases, specifically a mixture of a topologically nontrivial material (1st phase) with a topologically trivial material (2nd phase).

The dispersion relation of an electric gyrotropic bulk medium for transverse magnetic (TM) polarized waves (wave propagation in the *xoy* plane with $H = H_z(x,y)\hat{\mathbf{z}}$) is given by $k^2 = \varepsilon_{ef}(\omega/c)^2$, with $\varepsilon_{ef} = \left(\varepsilon_t^2 - \varepsilon_g^2\right)/\varepsilon_t$ the equivalent permittivity of the gyrotropic material, $k^2 = k_x^2 + k_y^2$ and k_x, k_y the wave vector Cartesian components.

VI.3.2 Photonic dispersion diagram

Figure 4.1a shows the band diagram of the TM polarized plane waves for a composite medium with $\omega_c/\omega_p = 0.5$ and $\omega_{p2} = \omega_p$, so that $\tilde{\omega}_p = \alpha\omega_p$ with $\alpha = \sqrt{f_V}$ determined by the

volume fraction of the trivial material phase. For $\alpha = 0$, the composite material has a single phase (1st component of the response) and the modes are organized in two branches separated by a band-gap. There are two photonic band-gaps highlighted as shaded regions in Fig. 4.1a. The respective gap Chern numbers are found as explained in Ref. [20] and are given in the insets. The Chern numbers are nonzero and hence the 1st phase is topologically non-trivial. On the other hand, the 2nd phase (with permittivity dispersion $\varepsilon_2 = 1 - \omega_{p2}^2 / \omega^2$) has a topologically trivial low-frequency band-gap determined by $0 < \omega < \omega_{p2}$ (not shown). Strikingly, for $\alpha = 0.5$ $\left(f_V = 0.25\right)$ when the two different phases are mixed, a new low-frequency band $\left(0.10 < \omega / \omega_p < 0.21\right)$ emerges well below the two relevant plasma frequencies ($\omega_p, \tilde{\omega}_p$). This "transparency" window is the focus of our study.

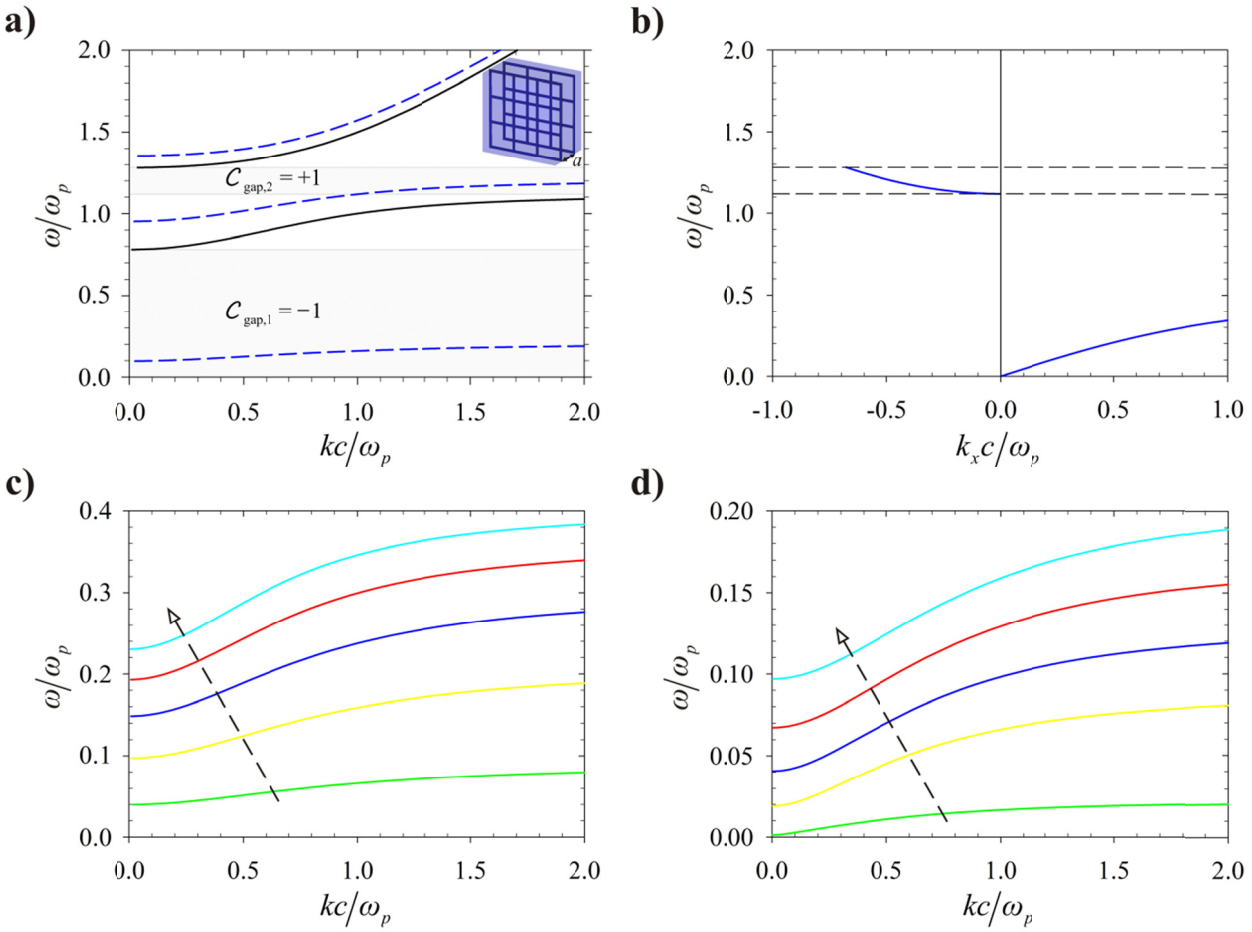

Figure 4.1: (a) Band diagram of the composite material for propagation in the xoy-plane (TM-polarized waves) with $\omega_c = 0.5\omega_p$ *for i)* $\alpha = 0$ *(solid black lines) and ii)* $\alpha = 0.5$ *(dashed blue lines). The inset depicts a possible metamaterial realization, with a stack of metallic wire grids embedded in a magnetized plasma. (b) Dispersion of the topological edge modes supported by a biased plasma (*$\omega_c = 0.5\omega_p$ *in the region* $y > 0$*) and a PEC interface (*$y = 0$*) for propagation along the x-direction. (c) low frequency band for* $\alpha = 0.5$ *and* $\omega_c / \omega_p = 0.2, 0.5, 0.8, 1.1, 1.4$ *(the arrow indicates the direction of increasing* ω_c / ω_p*) (d) low-frequency band for* $\omega_c = 0.5\omega_p$ *and* $\alpha = 0.05, 0.2, 0.3, 0.4, 0.5$ *(the arrow indicates the direction of increasing* α*).*

Figures 4.1c and 4.1d show how the transparency window changes under the variation of either α or ω_c / ω_p. Rather remarkably, the transparency window moves to even lower frequencies as either the volume fraction of the 2nd phase decreases (α decreases) or the bias magnetic field is reduced (lower values of ω_c / ω_p).

IV.4 Analytical Model – Transmission Properties

Next, we theoretically demonstrate that the newly found low-frequency mode can be externally excited, by exploring the wave scattering problem of a slab of the two-phase topological material.

IV.4.1 Scattering Parameters

It is assumed that the material slab is surrounded by air. The air interfaces are at $y=0$ and $y=d$, so that the propagation is along the *y*-direction. The magnetic field can be written as:

$$H_z = H_0^{inc} e^{ik_x x} \times \begin{cases} e^{-\gamma_0 y} + R e^{+\gamma_0 y} & , \quad y \le 0 \\ A_1 e^{-\gamma_g y} + A_2 e^{+\gamma_g y} & , \quad 0 \le y \le d \\ T e^{-\gamma_0 (y-d)} & , \quad y \ge d \end{cases} \tag{4.4}$$

where $\gamma_0 = \sqrt{k_x^2 - (\omega/c)^2}$ and $\gamma_g = \sqrt{k_x^2 - \varepsilon_{ef}(\omega/c)^2}$, *R* and *T* are the reflection and transmission coefficients, H_0^{inc} is the amplitude of the incident wave, $k_x = (\omega/c)\sin\theta_i$, and θ_i is the angle of incidence. The electric field in the gyrotropic material can be found using $\mathbf{E} = \frac{1}{-i\omega\varepsilon_0} \bar{\varepsilon}^{-1} \cdot \left(\partial_y H_z \hat{\mathbf{x}} - \partial_x H_z \hat{\mathbf{y}}\right)$ with $\bar{\varepsilon}^{-1} = \frac{1}{\varepsilon_{ef}} \left(\mathbf{1}_t - i \frac{\varepsilon_g}{\varepsilon_t} \hat{\mathbf{z}} \times \mathbf{1}_t \right) + \frac{1}{\varepsilon_a} \hat{\mathbf{z}} \otimes \hat{\mathbf{z}}$. Imposing the continuity of E_x and H_z at the interfaces one can find the transmission and reflection coefficients and the A_1, A_2 coefficients. In the following, we suppose that the dielectric function of the gyrotropic material is as in Eq. (4.3).

IV.4.2 Transmission properties – Numerical Results

Figure 4.2a shows the amplitude of the transmission coefficient as function of the

normalized thickness $L\omega_p/c$ for $\omega_c/\omega_p = 0.5$, $\alpha = 0.5$ and different values of incidence angle. The frequency of operation is $\omega/\omega_p = 0.15$ and thus lies roughly in the middle of the low-frequency transparency window (see Fig. 4.1a). As seen, the transmission coefficient exhibits a rather standard behavior with transmission peaks at the Fabry-Pérot resonances. Curiously, the transmission level improves for oblique incidence. Furthermore, Fig. 4.2b shows the transmission coefficient as function of the normalized frequency ω/ω_p for different values of the normalized thickness $L\omega_p/c$. Interestingly, independent of the slab thickness, the wave can tunnel through the two-phase material near the frequency $\omega/\omega_p \approx 0.1$, which determines the lower edge of the transparency window in Fig. 4.1a. This property is reminiscent of the super-coupling effect characteristic of structures with near-zero refractive index [67-69]. As illustrated in Fig. 4.2c, the transmission characteristic is relatively robust to the effects of unavoidable material loss.

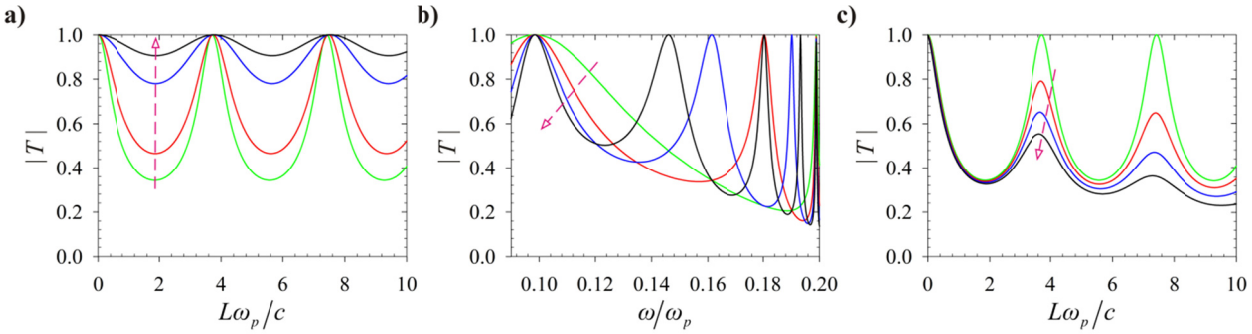

Figure 4.2: (a) Amplitude of the transmission coefficient as function of the normalized thickness $L\omega_p/c$ at the frequency $\omega = 0.15\omega_p$ for $\omega_c = 0.5\omega_p$ and $\alpha = 0.5$ and for the incidence angles: $\theta^{inc} = 0°, 45°, 70°, 80°$ (the arrow indicates the direction of increasing θ^{inc}) (b) Amplitude of the transmission coefficient as function of ω/ω_p for $\omega_c = 0.5\omega_p$, $\alpha = 0.5$ and $\theta^{inc} = 0°$ and for the normalized thicknesses: $L\omega_p/c = 1.0, 2.0, 3.0, 4.0$ (the arrow indicates the direction of increasing L). (c) Similar to (a) with $\theta^{inc} = 0°$ but for the plasma collision frequency: $\Gamma/\omega_p = 0, 0.005, 0.01, 0.015$ (the arrow indicates the direction of increasing Γ/ω_p).

IV.5 Physical implementation

In this section, we propose a realistic physical implementation of the structure based on the metamaterial concept and present detailed numerical full wave simulations confirming that the suggested two phase topological metamaterial does enable an anomalous wave tunneling at extremely low frequencies.

IV.5.1 Proposed metamaterial implementation

We suggest that the two-phase topological material may be implemented relying on a standard magnetized electron gas as the host medium (e.g., a magnetized doped semiconductor), and a metallic wire grid. Evidently, the magnetized electron gas is expected to mimic the response of the nontrivial topological phase, whereas the wire grid is expected to imitate the trivial topological phase. The wire medium is formed by an array of 2D-metallic grids separated (along *z*) by the distance *a* [70,71] (see the inset of Fig. 4.1a). Each metallic grid consists of two perpendicular co-planar arrays of metallic strips oriented along the *x* and *y* directions with period *a*. The width of the strips is $w = 0.1a$. For simplicity, the metal is modeled as a perfect electric conductor (PEC). By generalizing the homogenization approach of Refs. [70,72], we were able to demonstrate that the effective permittivity of the metamaterial satisfies (neglecting spatially dispersive effects),

$$\overline{\overline{\varepsilon}}_{ef} \approx \overline{\overline{\varepsilon}}_{h} - \frac{c^2}{\omega^2}\beta_p^2 \mathbf{1}_t , \tag{4.5}$$

where $\overline{\overline{\varepsilon}}_{h}$ is the relative permittivity of gyrotropic host medium and $\beta_p \approx \frac{1}{a}\left(2\pi / \left(\ln\left(a/p\right) + 0.5275\right)\right)^{1/2}$ with $p = 2w$ for strips with width *w* (for round metallic

wires with radius r_w one should use instead $p = 2\pi r_w$). Equation (4.5) extends the results of [70,72,73] to a gyrotropic host material. Its detailed derivation will be reported elsewhere.

In our design the host medium is taken as a magnetized plasma ($\omega_p / 2\pi = 0.1\text{THz}$) with a +*z*-directed magnetic bias with $\omega_c = 0.5\omega_p$. Interestingly, in this case Eq. (4.5) reduces to Eq. (4.3) with $\tilde{\omega}_p = c\beta_p$. The unavoidable effect of loss is modeled by the collision frequency Γ. Here, we note the inclusion of loss does not necessarily spoil the topological properties of the magnetized plasma [74]. The wire grid period was chosen $a = 1.91\text{mm}$. For $w = 0.1a$ one has $\beta_p \approx 1.7/a$, and therefore $\tilde{\omega}_p = \alpha\omega_p$ with $\alpha \approx 0.42$. Then, from Fig. 4.1d a new band is expected to emerge at $\omega \approx 0.073\omega_p$. In our simulations the metamaterial slab is periodic along the *x* and *z* directions and has thickness L along the *y* direction. We chose a periodic array of short horizontal electric dipoles (oriented along the *x*-direction) as the excitation. The dipole array emits a plane wave that illuminates the metamaterial slab along the normal direction.

IV.5.2 Numerical results

Figure 4.3a (black symbols) shows that similar to the continuum model, the metamaterial structure enables an anomalous wave tunneling at very low frequencies ($\omega = 0.095\omega_p$), where one would expect the electron gas and the wire grid to completely block the wave propagation. The effect occurs even in presence of realistic loss values ($\Gamma = 0.1\omega_p$). However, the transmission level with the metamaterial realization is weaker than in Fig. 4.2, in part due to the larger values of Γ and in part due spatial dispersion effects that are not captured by Eq.

(4.5). The matching between the metamaterial slab and the air regions can be noticeably improved with quarter-wavelength transformers at the input and output interfaces (blue symbols in Fig. 4.3a). In this case, the transmission amplitude may reach 15% for the thickness $L = 3a$. Figure 33b shows that the transmission level depends significantly on the thickness, due to the excitation of Fabry-Pérot resonances, further supporting that the metamaterial really supports a propagating mode.

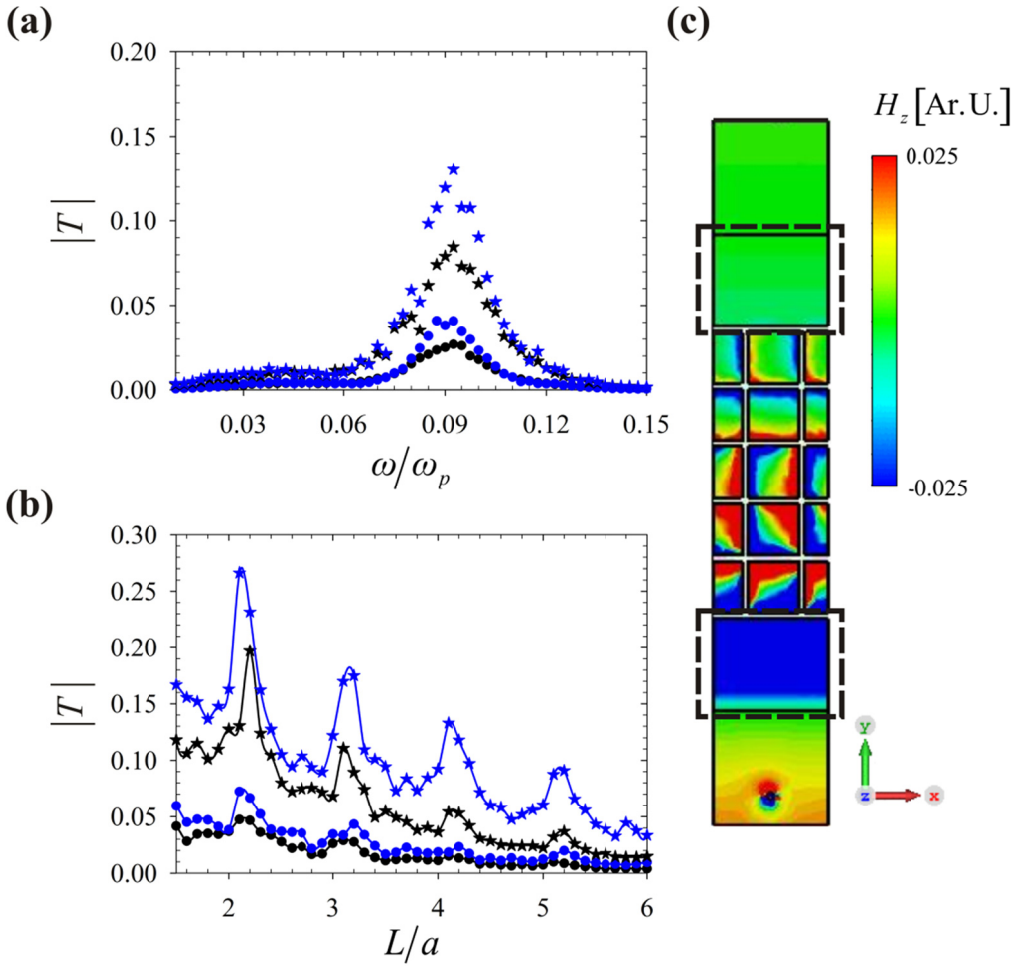

Figure 4.3: (a) Amplitude of the transmission coefficient as function of the normalized frequency ω/ω_p *for* $\omega_p/(2\pi) = 0.1$ THz, $\omega_c = 0.5\omega_p$, $a = 1.91$ mm, $\theta^{inc} = 0°$, *and* $L = 3a$ *for* $\Gamma = 0.1\omega_p$ *(black symbols) and for* $\Gamma = 0.05\omega_p$ *(blue symbols), without impedance transformers (circle symbols) and with* $\lambda/4$ *transformers with* $\varepsilon_{trans} = 6.7$ *(star symbols). (b) Amplitude of the transmission coefficient as function of the normalized thickness* L/a *at the frequency* $\omega = 0.095\omega_p$. *The legend and the remaining structural parameters are as in (a). (c) Time*

snapshot of the magnetic field (H_z) emitted by the dipole array at the frequency $\omega = 0.095\omega_p$, for $L = 5a$, $\Gamma = 0.1\omega_p$, and $\varepsilon_{\text{trans}} = 6.7$. The remaining structural parameters are same as in panel (a). The black dashed rectangles indicate the location of the $\lambda/4$ transformers. The results are obtained with a full wave simulator [76].

Figure 4.3c shows a time snapshot of the magnetic field at the frequency $\omega = 0.095\omega_p$ and for a thickness $L = 5a$. The time animation of the fields is available in Ref.[75] and reveals that in each metal loop the wave follows a rotating motion, such that the energy tends to circulate in closed orbits and the fields have a nontrivial angular momentum [23, 64]. This property can be understood as a consequence of the excitation of topological edge modes (magneto-plasmons) at the wire grid-gyrotropic material interface, due to the different topological nature of the two material phases. The dispersion of the magneto-plasmon mode is depicted in Fig. 4.1b for the case of a planar interface (*y*=0) between the gyrotropic host material and a PEC. The edge mode dispersion is found as explained in Refs. [9, 20, 21]. As seen, the low-frequency unidirectional edge mode propagates exclusively towards the +*x*-direction in the spectral range $0 < \omega < \omega_c$. When, the gyrotropic material fills a closed metallic cavity the low-frequency edge-mode will go around the cavity walls following an anti-clockwise motion [23], consistent with the winding motion of the magneto-plasmons in each loop of the wire grid. Thus, the anomalous transparency effect can be understood as a consequence of the excitation of topological modes that create coupled vortices of the electromagnetic field (see Fig. 4.3c and the time animation in Ref.[75]). Indeed, due to the different Chern numbers of the bulk materials, the bulk-edge correspondence indicates that localized surface states may emerge on metal structures embedded in a gyrotropic material (strictly speaking the bulk edge correspondence can be applied to planar interfaces, and hence the argument is semi-heuristic).

The new "transparency band" is due to the near-field coupling of the states supported by different cells.

IV.6 "Natural" Two-Phase Topological Materials

Incidentally, some natural materials may already have a permittivity response qualitatively similar to that of Eq. (4.3). For example, one can imagine a situation where the microscopic drift current of a plasma is dictated by two species of current carriers (e.g., with different effective mass or different density), i.e., the electron gas is formed by two distinct current "channels". Each species of carriers reacts differently to a bias field, and thereby the combined response of the two-channels may originate the different terms of the dielectric function (4.3). For instance, semiconductors may be good candidates for this concept.

An illustration of this concept is provided by the Gallium Arsenide (GaAs) semiconductor. The dielectric function of this semiconductor has three contributions: (i) the bound charges and (ii) the free electrons and (iii) the electron-holes. The response of the bound charges is insensitive to a bias magnetic field and may be described by a static permittivity term $\varepsilon_s = 12.8$. On the other hand, both the electrons and the holes originate drift-currents, yielding a multi-component plasma. The dielectric function of GaAs is of the type:

$$\varepsilon_t = \varepsilon_s - \frac{\omega_{pe}^2}{\omega^2 - \omega_{ce}^2} - \frac{\omega_{ph}^2}{\omega^2 - \omega_{ch}^2}, \qquad \varepsilon_g = \frac{1}{\omega}\frac{\omega_{pe}^2 \omega_{ce}}{\omega_{ce}^2 - \omega^2} + \frac{1}{\omega}\frac{\omega_{ph}^2 \omega_{ch}}{\omega_{ch}^2 - \omega^2} \tag{4.6}$$

with ω_{pe} and ω_{ph} (ω_{ce} and ω_{ch}) the plasma (cyclotron) frequencies for electrons and holes. Interestingly, comparing with Eq. (4.2), one sees that the dielectric function of the semiconductor is the same as for a mixture of two gyrotropic materials with parameters

$\left(\omega_{pe},\omega_{ce}\right)$ and $\left(\omega_{ph},\omega_{ch}\right)$. For GaAs the effective masses of electrons and holes are related as $m_e^* = 0.134 m_h^*$ [77,78]. Hence, the cyclotron frequencies of the two species are linked as $\omega_{ch} = -0.134\omega_{ce}$, and hence have *opposite signs*. Since the sign of the gap Chern number is linked to the sign of the cyclotron frequency [20], the material phases determined by each of the current carriers (electrons or holes) are topologically inequivalent. Indeed, for a +*z*-directed bias magnetic field, the band structure determined by the gyrotropic response with parameters ω_{pe},ω_{ce} (ω_{ph},ω_{ch}) has a low-frequency band-gap with gap Chern number -1 ($+1$).

Figure 4.4a shows the band diagram of GaAs with and without a bias magnetic field. The plasma frequency ($\omega_p = \left(e^2 n/\varepsilon_0 m^*\right)^{1/2}$) depends on the concentration (n) and effective mass (m^*) of each carrier species. For an intrinsic semiconductor the concentration of electrons and holes is identical, and for the GaAs case $\omega_{ph} = 0.37\omega_{pe}$. As seen, when $\omega_{ce} = 0 = \omega_{ch}$ (unbiased semiconductor) the dispersion of the modes (black solid line in Fig. 4.4a; the flat band associated with longitudinal modes is not shown) has a single band-gap near $\omega \approx \omega_{pe}/\sqrt{\varepsilon_s}$. Note that without the bias magnetic field both the electron and hole phases are trivial. In contrast, with a bias magnetic field the electron and hole phases become topologically distinct due to the different sign of the cyclotron frequencies. Hence, similar to the permittivity model (4.3), the combination of the two distinct topologically phases (which can be observed simply by applying a static bias magnetic field) determines the emergence of a low-frequency transparency window. The transparency window moves to lower frequencies as the bias magnetic field is reduced (ω_{ce}/ω_{pe} decreases) as shown in Fig. 4.4b, analogous to Fig. 4.1d. It is

interesting to note that the "electrons" and "holes" determine two independent current channels, somewhat analogous to the metamaterial design wherein the two material components (metal and magnetized plasma) also determine different paths for the electric current.

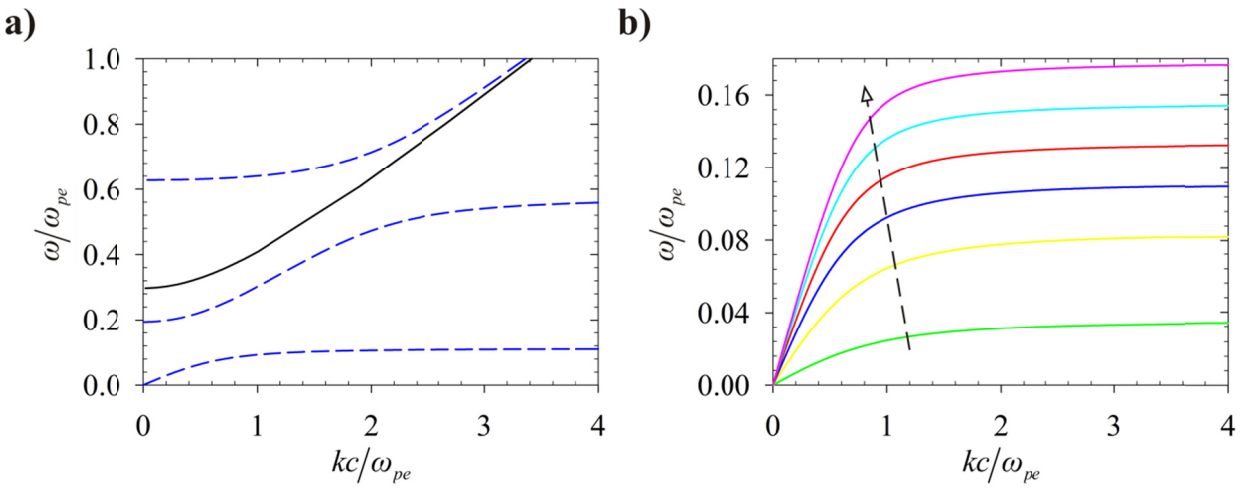

Figure 4.4: Band diagram of GaAs for propagation in the xoy-plane. (a) Unbiased (black solid line) and biased (blue dashed lines) GaAs with $\omega_{ce}/\omega_{pe}=0.5$. *(b) the low frequency band for different values of the field bias* $\omega_{ce}/\omega_{pe}=0.1,0.3,0.5,0.7,0.9,1.1$ *(the arrow indicates the direction of increasing* ω_{ce}/ω_{pe}*).*

IV.7 Conclusions

In summary, we theoretically demonstrated that by mixing two distinct topological material phases it is possible to create unusual conditions for wave propagation in a spectral range wherein the two phases are impenetrable by light. An electron gas with two current channels (e.g., intrinsic semiconductors) may provide an ideal platform to implement such a structure. In addition, we proposed a realistic metamaterial implementation of the suggested system. Detailed numerical simulations confirm that a material with two distinct topological phases enables, indeed, an anomalous wave tunneling at extremely low frequencies, and opens thus

new inroads and opportunities for topological effects in the terahertz and microwave ranges.

References

[1] A. Figotin, I. Vitebsky, "Nonreciprocal magnetic photonic crystals," *Phys. Rev. E*, **63**, 066609, 2001.

[2] Z. Wang, Y. D. Chong, J. D. Joannopoulos, M. Soljačić, "Refection-free one-way edge modes in a gyromagnetic photonic crystal", *Phys. Rev. Lett.*, **100**, 013905, 2008.

[3] Z. Yu, G. Veronis, Z. Wang, S. Fan, "One-way electromagnetic waveguide formed at the interface between a plasmonic metal under a static magnetic field and a photonic crystal", *Phys. Rev. Lett.*, **100**, 023902, 2008.

[4] K. Fang, Z. Yu, V. Liu, S. Fan, "Ultracompact nonreciprocal optical isolator based on guided resonance in a magneto-optical photonic crystal slab", *Opt. Lett.*, **36**, 4254-4256, 2011.

[5] D. L. Sounas and C. Caloz, "Gyrotropy and nonreciprocity of graphene for microwave applications," *IEEE Trans. Microw. Theory Tech.*, **60**, 901, 2012.

[6] T. Kodera, D. L. Sounas, C. Caloz, "Artificial Faraday rotation using a ring metamaterial structure without static magnetic field," *Appl. Phys. Lett*., **99**, 031114, 2011.

[7] D. L. Sounas, T. Kodera, C. Caloz, "Electromagnetic modeling of a magnetless and nonreciprocal gyrotropic metasurface", *IEEE Trans. Antennas Propag*., **61**, 221-231, 2013.

[8] Z. Yu, S. Fan, "Complete optical isolation created by indirect interband photonic transitions", *Nat. Photonics*, **3**, 91–94, 2009.

[9] A. R. Davoyan and N. Engheta, "Theory of Wave Propagation in Magnetized Near-Zero-Epsilon Metamaterials: Evidence for One-Way Photonic States and Magnetically Switched Transparency and Opacity", *Phys. Rev. Lett.*, **111**, 257401, 2013.

[10] A. M. Mahmoud, A. R. Davoyan, N. Engheta, "All-passive nonreciprocal metastructure", *Nat. Communications*, **6**, 8359, 2015.

[11] F. R. Prudêncio, M. G. Silveirinha, "Optical isolation of circularly polarized light with a spontaneous magnetoelectric effect", *Phys. Rev. A*, **93**, 043846, 2016.

[12] M. G. Silveirinha, "PTD Symmetry Protected Scattering Anomaly in Optics", *Phys. Rev. B*, **95**, 035153, 2017.

[13] D. L. Sounas, A. Alù, "Non-reciprocal photonics based on time modulation", *Nat. Photon.*, **11**, 774, 2017.

[14] T. A. Morgado, M. G. Silveirinha, "Drift-induced Unidirectional Graphene Plasmons", arXiv:1711.08367.

[15] F. D. M. Haldane, S. Raghu, "Possible realization of directional optical waveguides in photonic crystals with broken time-reversal symmetry", *Phys. Rev. Lett.*, **100**, 013904, 2008.

[16] Z. Wang, Y. Chong, J. D. Joannopoulos and M. Soljačić, "Observation of unidirectional backscattering immune topological electromagnetic states", *Nature*, **461**, 772, 2009.

[17] D. Jin, L. Lu, Z. Wang, C. Fang, J. D. Joannopoulos, M. Soljacic, L. Fu, and N. X. Fang, "Topological magnetoplasmon," *Nat. Commun.*, **7**, 13486, 2016.

[18] L. Lu, J. D. Joannopoulos, and M. Soljačić, "Topological photonics", *Nat. Photon.*, **8**, 821, 2014.

[19] T. Ozawa, H. M. Price, A. Amo, N. Goldman, M. Hafezi, L. Lu, M. C. Rechtsman, D. Schuster, J. Simon, O. Zilberberg, I. Carusotto, "Topological Photonics", arXiv:1802.04173, 2018.

[20] M. G. Silveirinha, "Chern Invariants for Continuous Media", *Phys. Rev. B*, **92**, 125153, 2015.

[21] M. G. Silveirinha, "Bulk edge correspondence for topological photonic continua", *Phys. Rev. B*, **94**, 205105, 2016.

[22] M. G. Silveirinha, "Proof of the bulk-edge correspondence through a link between topological photonics and fluctuation-electrodynamics", arXiv:1804.02190, 2018.

[23] M. G. Silveirinha, "Quantized Angular Momentum in Topological Optical Systems", (under review), 2018.

[24] L. D. Landau and E. M. Lifshitz, "Electrodyamics of Continuous Media", Pergamon Press, 1984.

[25] H. Suhl, and L. R. Walker, "Topics in guided-wave propagation through gyromagnetic media: Part I — The completely filled cylindrical guide", *Bell Syst. Tech. Journal*, **33**, 579–659, 1954.

[26] W. P. Allis, S. J. Buchsbaum, and A. Bers, "Waves in Anisotropic Plasmas", *MIT Press*, Cambridge, Mass., 1963.

[27] M. Toda, "Propagation in a solid state plasma waveguide in a transverse magnetic field," *J. Phys. Soc. Japan*, **19**, 1126– 1130, 1964.

[28] R. Hirota, "Theory of a solid state plasma waveguide in a transverse magnetic field," *J. Phys. Soc. Japan*, **19**, 1130–1134, 1964.

[29] R. E. Collin, "Electromagnetic potentials and field expansions for plasma radiation in waveguide", *IEEE Trans. Microw. Theory Tech.*, **12**, 413–420, 1965.

[30] G. J. Gabriel, and M. E. Brodwin, "The solution of guided waves in inhomogeneous anisotropic media by perturbation and variational methods", *IEEE Trans. Microw. Theory and Tech*, **13**, 364–370, May 1965.

[31] G. J. Gabriel, and M. E. Brodwin, "Distinctions between gyroelectric and gyromagnetic

media in rectangular waveguide", *IEEE Trans. Microw Theory and Tech*, **14**, 292–293, 1966.

[32] R. Hirota, and K. Suzuki, "Propagation of waves in a bounded solid state plasma in transverse magnetic fields", *J. Phys. Soc. Japan*, **21**, 1112–1118, 1996.

[33] H. J. Kuno, and W. D. Hershberger, "Microwave faraday effect and propagation in a circular solid-state plasma waveguide", *IEEE Trans. Microwave Theory Tech.*, **15**, 661-668, 1967.

[34] K. S. Champlin, G. H. Glover, and D. E. O'Connor, "Plasma filled waveguide with axial magnetization: I — Variational determination of normal modes", *J. Appl. Phys*, **40**, 3532–3538, 1969.

[35] K. S. Champlin, and G. H. Glover, ""twist" modes in magnetoplasma-filled circular waveguides", *IEEE Trans. Microw. Theory Tech.*, **18**, No. 9, 566–570, 1970.

[36] R. Hirota, and K. Suzuki, "Field distribution in a magnetoplasma-loaded waveguide at room temperature", *IEEE Trans. Microw. Theory Tech.*, **18**, No. 4, 188–195, 1970.

[37] A. Gurevich, "Magnetization Oscillations and Waves", 1st Ed. Boca Raton: CRC Press; 1996.

[38] M. Faraday, Faraday's Diary, T. M. Martin, Ed. George Bell and Sons, Ltd., 1932, vol. IV: Nov. 12, 1839-June 26, 1847.

[39] A. Gray, "Modern differential geometry of curves and surfaces with Mathematica", (CRC Press, Boca Raton, 1999).

[40] T. Ozawa and I. Carusotto, "Anomalous and Quantum Hall Effects in Lossy Photonic Lattices", *Phys. Rev. Lett.*, **112**, 133902, 2014.

[41] C.-E. Bardyn, S.D. Huber, and O. Zilberberg, "Measuring topological invariants in small photonic lattices", *New J. Phys.*, **16**, 123013, 2014.

[42] Y. E. Kraus, Y. Lahini, Z.Ringel, M.Verbin and O. Zilberberg, "Topological states and adiabatic pumping in quasicrystals", *Phys. Rev. Lett.*, **109**, 106402, 2012.

[43] M. Verbin, O. Zilberberg, Y. Lahini, Y. E. Kraus, and Y. Silberberg, "Topological pumping over a photonic Fibonacci quasicrystal", *Phys. Rev. B*, **91**, 064201, 2015.

[44] M. Rechtsman et al., "Photonic Floquet topological insulators", *Nature*, **496**, 196–200, 2013.

[45] M. Hafezi, S. Mittal, J. Fan, A. Migdall and J. Taylor, "Imaging topological edge states in silicon photonics", *Nat. Photon.*, **7**, 1001–1005, 2013.

[46] X. Cheng et al., "Robust reconfigurable electromagnetic pathways within a photonic topological insulator", *Nat. Mater.*, **15**, 542–548, 2016.

[47] Hatsugai, Yasuhiro, "Chern number and edge states in the integer quantum hall effect", *Phys. Rev. Lett.*, **71**, 3697–3700, 1993.

[48] Hatsugai, Yasuhiro, "Edge states in the integer quantum hall effect and the Riemann

surface of the Bloch function", *Phys. Rev. B*, **48**, 11851–11862, 1993.

[49] R. Jackiw, and C. Rebbi, "Solitons with fermion number 1/2", *Phys. Rev. D*, **13**, 3398–3409, 1976.

[50] X.-L. Qi, Y.-S. Wu, and S.-C. Zhang, "General theorem relating the bulk topological number to edge states in two-dimensional insulators", *Phys. Rev. B*, **74**, 045125, 2006.

[51] X. Deng, L. Hong, X. Zheng, and L. Shen, "One-way regular electromagnetic mode immune to backscattering", *Applied optics*, **54** (14), 4608– 4612, 2015.

[52] A. Hartstein, E. Burstein, A. A. Maradudin, R. Brewer, and R. F. Wallis, "Surface polaritons on semi-infinite gyromagnetic media", *Journal of Physics C: Solid State Physics*, **6** (7), 1266, 1973.

[53] T. Ochiai, "Non-reciprocity and topology in optics: one-way road for light via surface magnon polariton", *Sci. Technol. Adv. Mater.*, **16** (1), 014401, 2015.

[54] Shen, Linfang, Yun You, Zhuoyuan Wang, and Xiaohua Deng, "Backscattering-immune one-way surface magnetoplasmons at terahertz frequencies", *Optics express*, **23** (2), 950–962, 2015.

[55] Yu, Zaihe, Zhuoyuan Wang, Linfang Shen, and Xiaohua Deng, "One-way electromagnetic mode at the surface of a magnetized gyromagnetic medium", *Electronic Materials Letters*, **10** (5), 969–973, 2014.

[56] Zhang, Xiaogang, Wei Li, and Xunya Jiang, "Confined one-way mode at magnetic domain wall for broadband high-efficiency one-way waveguide, splitter and bender", *Appl. Phys. Lett.*, **100** (4), 041108, 2012.

[57] M. G. Silveirinha, "Z_2 topological index for continuous photonic materials", *Phys. Rev. B*, **93** (7), 075110, 2016.

[58] M. G. Silveirinha, "A Metamaterial Homogenization Approach with Application to the Characterization of Microstructured Composites with Negative Parameters", *Phys. Rev. B*, **75**, 115104, 2007.

[59] M. Xiao and S. Fan, "Photonic Chern insulator through homogenization of an array of particles", *Phys. Rev. B*, **96**, 100202(R), 2017.

[60] A. H. Sihvola, *Electromagnetic Mixing Formulas and Applications*, IET (London), 1999.

[61] E. D. Palik, R. Kaplan, R. W. Gammon, H. Kaplan, R. F. Wallis, and J. J. Quinn II, "Coupled surface magnetoplasmon-optic-phonon polariton modes on InSb", *Phys. Rev. B*, **13**, 2497, 1976.

[62] E. Moncada-Villa, V. Fernández-Hurtado, F. J. García-Vidal, A. García-Martín and J. C. Cuevas, "Magnetic field control of near-field radiative heat transfer and the realization of highly tunable hyperbolic thermal emitters", *Phys. Rev. B*, **92**, 125418, 2015.

[63] J. A. Bittencourt, *Fundamentals of Plasma Physics*, 3rd Ed. Springer-Verlag, NY, 2010.

[64] M. G. Silveirinha, "Topological Angular Momentum and Radiative Heat Transport in Closed Orbits", *Phys. Rev. B*, **95**, 115103, 2017.

[65] S. A. H. Gangaraj, A. Nemilentsau, G. W. Hanson, "The effects of three-dimensional defects on one-way surface plasmon propagation for photonic topological insulators comprised of continuum media", *Sci. Rep.*, 6, 30055, 2016.

[66] S. A. H. Gangaraj, G. W. Hanson, "Topologically protected unidirectional surface states in biased ferrites: duality and application to directional couplers", *IEEE Antennas Wireless Propag. Lett.*, **16**, 449, 2016.

[67] M. Silveirinha, N. Engheta, "Tunneling of electromagnetic energy through sub-wavelength channels and bends using near-zero-epsilon materials", *Phys. Rev. Lett.*, **97**, 157403, 2006.

[68] M. G. Silveirinha, and N. Engheta, "Theory of Supercoupling, Squeezing Wave Energy, and Field Confinement in Narrow Channels and Tight Bends Using Epsilon-Near-Zero Metamaterials", *Phys. Rev. B*, **76**, 245109, 2007.

[69] N. Engheta, "Pursuing Near-Zero Response", *Science*, **340**, pp. 286-287, 2013.

[70] M. G. Silveirinha, C. A. Fernandes, "Homogenization of 3D- Connected and Non-Connected Wire Metamaterials", *IEEE Trans. on Microwave Theory and Tech.*, **53**, 1418, 2005.

[71] M. G. Silveirinha, C. A. Fernandes, "Transverse Average Field Approach for the Characterization of Thin Metamaterial Slabs", *Phys. Rev. E*, **75**, 036613, 2007.

[72] M. G. Silveirinha, "Artificial plasma formed by connected metallic wires at infrared frequencies", *Phys. Rev. B*, **79**, 035118(1-15), 2009.

[73] P.A. Belov, R. Marqués, S. I. Maslovski, I.S. Nefedov, M. Silveirinha, C. R. Simovsky, S. A. Tretyakov, "Strong spatial dispersion in wire media in the very large wavelength limit", *Phys. Rev. B*, **67**, 113103, 2003.

[74] H. Shen, B. Zhen, and L. Fu, "Topological Band Theory for Non-Hermitian Hamiltonians", *Phys. Rev. Lett.* **120**, 146402, 2018.

[75] Supplementary online materials with a time animation of Fig. 3c.

[76] CST Microwave Studio 2017 (http://www.cst.com).

[77] M. R. Amin, "Quantum effects on compressional Alfven waves in compensated semiconductors", Physics of Plasmas, **22**, 032303, 2015.

[78] A. Moradi, "Surface and bulk plasmons of electron-hole plasma in semiconductor nanowires", *IEEE Antennas Wireless Propag. Lett.*, **23**, 114503, 2016.

CHAPTER 5 :

Exotic light-matter interactions in a tilted wire medium

V. Exotic light-matter interactions in a tilted wire medium

V.1 Introduction

The optical manipulation of small particles is important for the laser cooling of neutral atoms, particle transport, optical sorting, just to name a few applications [1]-[7]. The optical trapping operation relies on tightly focused laser beams (optical tweezers), which allow one to precisely position and displace neutral particles using gradient-type optical forces [8-14].

Furthermore, fluctuation-induced optical (Casimir-Polder) forces acting on atoms near the surface of a material are of considerable interest due to their relevance in a variety of processes in physics, biology and chemistry [15]-[17]. In such a context, in translation-invariant scenarios, e.g., when an atom stands nearby a perfectly smooth material surface, the ground-state Casimir-Polder force acting on the atom is along the direction normal to interface. Typically, the quantum vacuum fluctuations result in an attractive force that pulls the atom towards the surface. Interestingly, despite the translation invariance property, for an excited atom the Casimir-Polder force gains an extra resonant term [18], which can have a lateral component. The lateral force is a consequence of the directional nature of the fields emitted by the excited atom in a spontaneous emission process. Similar lateral forces emerge even when one adopts a purely classical treatment, wherein the atom is modeled as a polarizable particle. In particular, lateral forces have been predicted for chiral particles standing above a metal surface and related platforms [19]-[26], and in a few non-reciprocal systems [27]-[30]. In fact, intuitively one may expect that whenever the radiation pattern of the emitter is asymmetric, let us say

when it radiates more energy to the “right” as compared to the “left”, then the conservation of momentum should imply the emergence of a lateral (recoil-type) optical force. This is precisely what happens when a chiral emitter loses its energy in a spontaneous emission process above a metallic surface [20]-[22]. In this case, the atom will couple selectively to plasmons with a certain handedness, and hence due to the spin momentum locking property [31], it will emit more strongly in certain directions of space.

Motivated by this result, one may wonder if linearly polarized dipoles standing above a reciprocal material half-space can experience similar lateral forces. For example, heuristically one may expect the emergence of lateral forces when an atom or classical particle relaxes from an excited state to the ground near a standard uniaxial material half-space with the optical axis tilted with respect to the interface (see Ref. [32] for a related problem), for example a tilted wire medium. Furthermore, since an excited chiral-particle above a dielectric substrate can experience a non-trivial lateral force [20]-[21], one may wonder if the chiral property can be “swapped” with the substrate, i.e., if an excited linearly polarized particle above a chiral substrate may experience a nontrivial recoil-force. Surprisingly, we prove here that for a linearly-polarized particle with a purely electric response (electric dipole approximation) the lateral force vanishes for any reciprocal translation-invariant substrate, independent of the orientation of the optical axes or of the bianisotropy (chirality) of the involved materials. In particular, it follows that the chiral response of the atom cannot be “transferred” to the substrate. Interestingly, we propose a new mechanism to have non-trivial lateral forces with linearly-polarized particles with nontrivial electric and magnetic responses. For the sake of

simplicity, we adopt a classical picture wherein the particle is regarded as superposition of electric and magnetic dipoles.

V.2 Force on a Single Electric Dipole

To begin with, it is supposed that the particle has purely electric response and can be approximated by an electric dipole. It is assumed that the dipole oscillations are either pumped by an incident wave (e.g., a plane wave) that does not impress on its own a lateral force along the relevant test direction, or, alternatively, the oscillations may be the result of the relaxation of some natural mode of oscillation with complex-valued frequency $\omega = \omega' - i\omega''$, with $\omega'' > 0$. The decay rate of the dipole oscillations is determined by ω''.

V.2.1 Lateral force on a linearly polarized dipole

Let us suppose that a generic electric dipole with dipole moment $\mathbf{p}_e$ stands in air near the flat surface of an arbitrary smooth translation-invariant reciprocal substrate. The direction normal to the substrate is along *z* (see a generic geometry in Fig. 5.1a). For now, we consider the scenario wherein the dipole oscillations are driven by an incident beam so that the oscillation frequency ω is real-valued. The case wherein the dipole oscillations are damped (ω is complex-valued) and the emitted radiation is due to the decay from an excited state is discussed in Sect. V.2.3. The time-averaged optical force acting on the electric dipole for a time harmonic oscillation is (the time harmonic variation $e^{-i\omega t}$ is implicit),

$$\mathscr{F} = \frac{1}{2}\mathrm{Re}\left\{\nabla\left[\mathbf{p}_e^* \cdot \mathbf{E}_{\mathrm{loc}}\right]\right\}_{\mathbf{r}=\mathbf{r}_0}, \tag{5.1}$$

where $\mathbf{r}_0$ is the position of the dipole center of mass. In the above, $\mathbf{E}_{\mathrm{loc}}$ represents the complex

amplitude of the local field at the particle position,

$$\mathbf{E}_{\mathrm{loc}} = \mathbf{E} - \mathbf{E}^{\mathrm{self}}, \tag{5.2}$$

with $\mathbf{E}$ the total electric field and $\mathbf{E}^{\mathrm{self}}$ the self-field of the dipole in free-space. It can be decomposed as:

$$\mathbf{E}_{\mathrm{loc}} = \mathbf{E}^{\mathrm{ext}} + \mathbf{E}^{\mathrm{s}}, \tag{5.3}$$

where $\mathbf{E}^{\mathrm{ext}}$ is the external electric field that drives the oscillations and $\mathbf{E}^{\mathrm{s}}$ is the field back-scattered by the substrate due to the dipole oscillations. Specifically, $\mathbf{E}^{\mathrm{ext}}$ is the field distribution created by the incident beam in the absence of the dipolar particle, whereas $\mathbf{E}^{\mathrm{self}} + \mathbf{E}^{\mathrm{s}}$ is the field radiated by a particle with the dipole moment $\mathbf{p}_e$ standing above the substrate. Note that $\mathbf{E}^{\mathrm{ext}}$ is the superposition of the incident wave and of the wave reflected on the substrate in the absence of the particle. The dipole moment $\mathbf{p}_e$ is itself a function of $\mathbf{E}_{\mathrm{loc}}$ and of the electric polarizability of the particle and its precise value must be determined self-consistently.

From the previous discussion, the optical force can be decomposed as:

$$\mathscr{F} = \mathscr{F}^{\mathrm{ext}} + \mathscr{F}^{\mathrm{s}}, \tag{5.4}$$

with $\mathscr{F}^{\mathrm{ext}} = \frac{1}{2}\mathrm{Re}\left\{\nabla\left[\mathbf{p}_e^{*}\cdot\mathbf{E}^{\mathrm{ext}}\right]\right\}_{\mathbf{r}=\mathbf{r}_0}$ the force component due to a gradient in the external field and $\mathscr{F}^{\mathrm{s}} = \frac{1}{2}\mathrm{Re}\left\{\nabla\left[\mathbf{p}_e^{*}\cdot\mathbf{E}^{\mathrm{s}}\right]\right\}_{\mathbf{r}=\mathbf{r}_0}$ the force component due to the dipole oscillations.

We will consider throughout the chapter that the gradient of the external field vanishes along the relevant lateral test direction $\partial_i \mathbf{E}^{\mathrm{ext}} = 0$ with $\partial_i = \partial/\partial x_i$ and *i=1* or *i=2* ($x_1 \equiv x$ and

$x_2 \equiv y$). In these conditions, the lateral force is determined simply by $\mathscr{F}^{\mathrm{s}}$. It is shown in Appendix A, that the back-scattered field can be written as $\mathbf{E}^{\mathrm{s}}(\mathbf{r}) = \mathbf{C}_{\mathrm{int}}^{\mathrm{ee}}(\mathbf{r},\mathbf{r}_0)\cdot\mathbf{p}_e/\varepsilon_0$ with $\mathbf{C}_{\mathrm{int}}^{\mathrm{ee}}$ a 3×3 dyadic expressed in terms of the reflection coefficient matrix $\mathbf{R}$ for plane wave incidence [Eq. (5.A1b)]. Therefore, in the outlined conditions the time-averaged lateral force acting on the dipole along the *i-th* direction is,

$$\mathscr{F}_i^{\mathrm{s}} = \mathrm{Re}\left\{\frac{1}{2\varepsilon_0}\mathbf{p}_e^{*}\cdot\left.\frac{\partial\mathbf{C}_{\mathrm{int}}^{\mathrm{ee}}}{\partial x_i}\right|_{\mathbf{r}=\mathbf{r}_0}\cdot\mathbf{p}_e\right\}, \qquad (i=1,2). \tag{5.5}$$

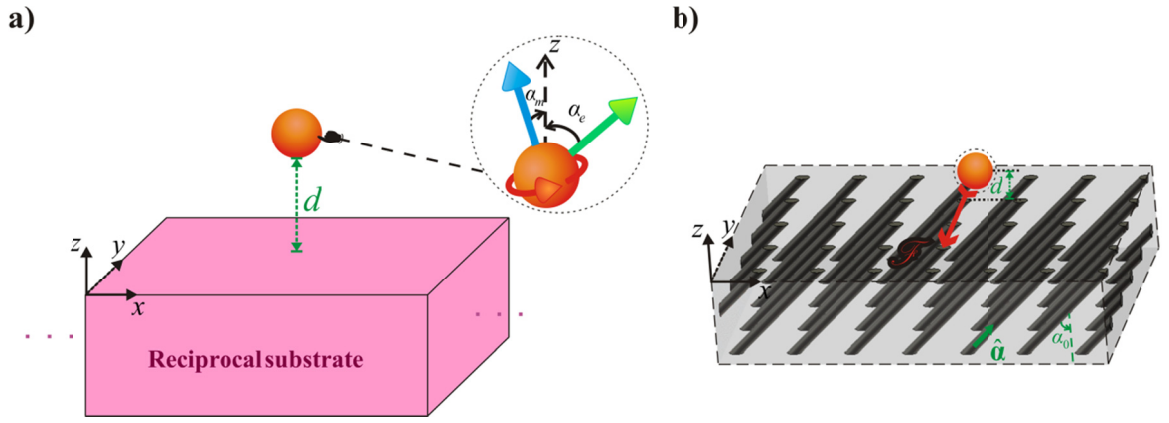

Figure 5.1: (a) Geometry of the problem: The particle is formed either by a single electric dipole or by two linearly polarized electric and magnetic dipoles. The particle stands in the air region at a distance d from a reciprocal material (half-space $z<0$). (b) Illustration of the uniaxial material substrate with tilted optical axis. The substrate can be visualized as a "tilted wire medium" and is treated in our model as a continuous medium with no granularity.

V.2.2 Electric dipole standing above a uniaxial material with tilted optical axes

To illustrate the application of the described theory, we consider some particle that can be modeled as an electric dipole moment oriented along the *z*-direction: $\mathbf{p}_e = p_e\hat{\mathbf{z}}$. It is supposed that the particle stands above a uniaxial dielectric material with relative permittivity tensor $\boldsymbol{\varepsilon} = \varepsilon_{\alpha\alpha}\hat{\boldsymbol{\alpha}}\otimes\hat{\boldsymbol{\alpha}} + \varepsilon_{\parallel}(\mathbf{1}-\hat{\boldsymbol{\alpha}}\otimes\hat{\boldsymbol{\alpha}})$, with optical axis in the *xoz* plane along $\hat{\boldsymbol{\alpha}} = \sin\alpha_0\,\hat{\mathbf{x}} + \cos\alpha_0\,\hat{\mathbf{z}}$ (see

Fig. 5.1b). For now, the permittivity components are taken equal to $\varepsilon_{\alpha\alpha} = -\infty$ and $\varepsilon_{\|} = 1$, which corresponds to a regime of extreme anisotropy. The tilt angle is chosen equal to $\alpha_0 = 45°$. To ease the visualization of the structure, in Fig. 5.1b the substrate is represented as a "tilted wire medium", formed by an array of tilted metallic wires [33-36]. Note that in our analysis the substrate is regarded as perfectly smooth with no intrinsic granularity. Furthermore, spatial dispersion effects are neglected. The interaction dyadic $\mathbf{C}_{\text{int}}^{\text{ee}}$ is determined by Eq. (5.A1b) with the reflection matrix $\mathbf{R}$ determined as explained in Appendix B.

Figure 5.2a shows the radiation pattern of the scattered electric field at $z = d$ plane (dashed line) for a dipole at the normalized distance $d\omega / c = 1$ from the interface. As seen, the fields are scattered more to the +*x*-direction than to the –*x* direction. The asymmetry of the radiation pattern and the conservation of linear momentum suggests that the emitter should experience a lateral recoil force directed towards the –*x*-direction.

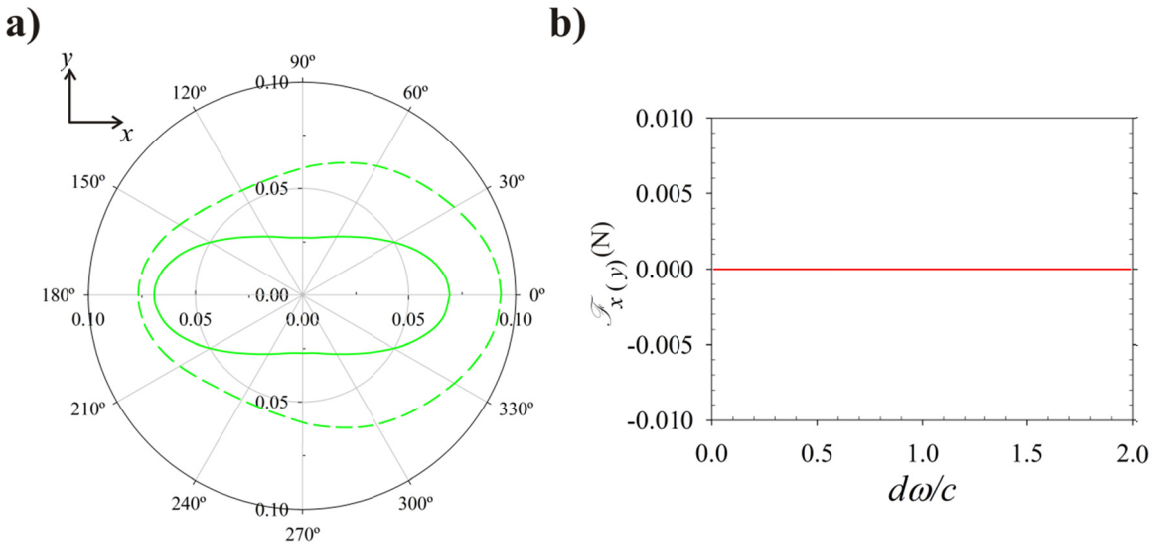

Figure 5.2: (a) Polar plot of the intensity of the field back-scattered by the substrate (arbitrary normalization) calculated at the distance λ_0 from the vertical dipole. Dashed line: total field ($|\mathbf{E}^s|^2$) intensity. Solid line: intensity of the z-component ($|\mathbf{E}_z^s|^2$) of the electric field. The substrate is a uniaxial dielectric half-space ($\varepsilon_{\|} = 1$ and $\varepsilon_{\alpha\alpha} = -10^6$) with tilted optical axes ($\alpha_0 = 45°$) at the normalized distance is $d\omega / c = 1$. (b) Plot of the lateral force $\mathcal{F}_i^s$

$\left(i=\{x,y\}\right)$ *as a function of* $d\omega/c$ *for the same configuration as in (a).*

Surprisingly, by evaluating Eq. (5.5) using numerical methods we find that up to machine precision the lateral force $\mathscr{F}_i^{\mathrm{s}}$ is precisely zero (Fig. 5.2b). We numerically verified that this result is rather general and does not depend on any of the structural parameters of the problem (e.g., the direction α_0 of the optical axis or the distance to the interface).

V.2.3 Reciprocity constraints

Next, it is shown that the result reported in the previous subsection is rather universal and that independent of the anisotropy or chirality of the reciprocal substrate, for a linearly-polarized electric dipole the lateral force $\mathscr{F}_i^{\mathrm{s}}$ invariably vanishes. The substrate may be non-uniform along the *z*-direction (e.g., it can have finite thickness) and it is assumed to be invariant to translations along *x* and *y*.

The proof is based on the reciprocity theorem, $\int \mathbf{E}'\cdot\mathbf{j}''dV=\int \mathbf{E}''\cdot\mathbf{j}'dV$, which applies to generic solutions (primed and unprimed) of Maxwell's equations that satisfy radiation boundary conditions. We take $\mathbf{E}'$ ($\mathbf{E}''$) as the field radiated by a generic electric dipole $\mathbf{j}'=-i\omega\mathbf{p}_e'\delta\left(\mathbf{r}-\mathbf{r}'\right)$ ($\mathbf{j}''=-i\omega\mathbf{p}_e''\delta\left(\mathbf{r}-\mathbf{r}''\right)$) standing above the reciprocal substrate. Since the reciprocity relation is also satisfied by the self-fields in free-space, it follows that it must also be satisfied by the back-scattered fields: $\int \mathbf{E}'^{\mathrm{s}}\cdot\mathbf{j}''dV=\int \mathbf{E}''^{\mathrm{s}}\cdot\mathbf{j}'dV$. Using now $\mathbf{E}^{\mathrm{s}}\left(\mathbf{r}\right)=\mathbf{C}_{\mathrm{int}}^{\mathrm{ee}}\left(\mathbf{r},\mathbf{r}_0\right)\cdot\mathbf{p}_e/\varepsilon_0$ we conclude that for two generic electric dipoles $\mathbf{p}_e'$, $\mathbf{p}_e''$ positioned at $\mathbf{r}'$, $\mathbf{r}''$, respectively, one has,

$$\mathbf{p}_e'' \cdot \mathbf{C}_{\text{int}}^{\text{ee}}\left(\mathbf{r}'', \mathbf{r}'\right) \cdot \mathbf{p}_e' = \mathbf{p}_e' \cdot \mathbf{C}_{\text{int}}^{\text{ee}}\left(\mathbf{r}', \mathbf{r}''\right) \cdot \mathbf{p}_e''. \tag{5.6}$$

Suppose now that the *z*-coordinate (perpendicular to the substrate) of the two dipoles is the same: $z' = z'' \equiv z_0$. Then, because the substrate is invariant to translations along the *x* and *y* directions the interaction dyadic is necessarily of the form: $\mathbf{C}_{\text{int}}^{\text{ee}}\left(\mathbf{r}_2, \mathbf{r}_1\right) = \mathbf{C}_{\text{int}}^{\text{ee}}\left(\mathbf{r}_2 - \mathbf{r}_1, z_0\right)$. Hence, taking first the derivative of both sides of Eq. (5.6) with respect to x_i' (*i*=1,2) and then setting $\mathbf{r}_1 = \mathbf{r}_2 \equiv \mathbf{r}_0$ it follows that:

$$\mathbf{p}_e'' \cdot \left[\partial_i \mathbf{C}_{\text{int}}^{\text{ee}}\right]_{\mathbf{r}=\mathbf{r}_0} \cdot \mathbf{p}_e' = -\mathbf{p}_e' \cdot \left[\partial_i \mathbf{C}_{\text{int}}^{\text{ee}}\right]_{\mathbf{r}=\mathbf{r}_0} \cdot \mathbf{p}_e'', \tag{5.7}$$

i.e., $\left[\partial_i \mathbf{C}_{\text{int}}^{\text{ee}}\right]_{\mathbf{r}=\mathbf{r}_0}$ is an anti-symmetric tensor. In particular, if one chooses $\mathbf{p}_e' = \mathbf{p}_e'' \equiv \mathbf{p}_e$ it follows that $\mathbf{p}_e \cdot \partial_i \mathbf{C}_{\text{int}} \cdot \mathbf{p}_e = 0$, and this proves that for linear polarization (when $\mathbf{p}_e$ can be taken as a real-valued vector) the lateral force $\mathscr{F}_i^{\text{s}}$ [Eq. (5.5)] vanishes, in agreement with the numerical results of subsection V.2.2. This concludes of the proof that the lateral force vanishes.

It is worth noting that the reciprocity property [Eq. (5.6)] implies that for a dipole oriented along the *z*-direction the radiation pattern of the *z*-component of the electric field $\left|E_z^{\text{s}}\right|$ must have the parity-symmetry $\left(x, y, z\right) \to \left(-x, -y, z\right)$. Our numerical simulations (see the solid line in Fig. 5.2a) confirm this property. However, the reciprocity property does not enforce any particular symmetry on the *total* radiation pattern $\left|\mathbf{E}^{\text{s}}\right|^2$ (dashed line in Fig. 5.2a).

More generally, the reciprocity implies that the lateral force acting on a particle with dipolar moment $\mathbf{p}_e$ differs from a minus sign from of the lateral force acting on a particle with dipole moment $\mathbf{p}_e^*$, i.e., with the opposite handiness: $\mathscr{F}_{L,\mathbf{p}_e}^{\text{s}} = -\mathscr{F}_{L,\mathbf{p}_e^*}^{\text{s}}$. This property implies, for

example, that the $\mathscr{F}_i^{\mathrm{s}}$ component of the lateral force acting on a left-circularly polarized dipole is always the additive symmetric of the force acting on a right-circularly polarized dipole when the substrate is reciprocal.

A straightforward generalization of the above proof shows that when a particle can be modeled as a linearly polarized magnetic dipole the lateral force ($\mathscr{F}_i^{\mathrm{s}}$) also vanishes.

V.2.4 Relaxation problem

The analysis of the previous subsections can be readily generalized to the case of free-damped oscillations of a classical dipole with no external excitation. Indeed, due to the light-matter coupling (and because the system is open) the natural modes of oscillation of the dipole are characterized by a complex-valued frequency $\omega = \omega_0' - i\omega_0''$, with $\omega_0'' > 0$, so that the time variation is of the form $e^{-i\omega_0' t} e^{-\omega_0'' t}$. In this case, the total optical force acting on the dipole is simply

$$\mathscr{F} = \underbrace{\frac{1}{2}\mathrm{Re}\left\{\nabla\left[\mathbf{p}_e^* \cdot \mathbf{E}^{\mathrm{s}}\right]\right\}_{\mathbf{r}=\mathbf{r}_0}}_{\mathscr{F}^{\mathrm{s}}} e^{-2\omega_0'' t}. \tag{5.8}$$

The force $\mathscr{F}^{\mathrm{s}}$ is still determined by Eq. (5.5) but now $\mathbf{C}_{\mathrm{int}}^{\mathrm{ee}}$ is evaluated at the complex frequency $\omega = \omega_0' - i\omega_0''$. Note that in a relaxation problem $\omega_0' - i\omega_0''$ and $\mathbf{p}_e$ depend on the microstructure of the particle and are generally found from the solution of an eigenvalue problem.

By analytical continuation arguments, the reciprocity result (Eq. (5.6)) still holds for complex-valued values of ω. Therefore, proceeding as in subsection V.2.3 one can readily prove that when $\mathbf{p}_e$ is linearly-polarized the lateral (*x* and *y*) components of the lateral force ($\mathscr{F}^{\mathrm{s}}$) must

vanish when the substrate is reciprocal. In other words, when an excited linearly-polarized particle relaxes above a reciprocal translation-invariant substrate the optical force is always directed along the normal (*z*) direction, so that the lateral components are precisely zero.

V.3 Optical Force on a Composite Linearly-Polarized Dipole

Next, we identify a new opportunity to generate a lateral force from the radiation emitted by a generic *linearly polarized* particle. Specifically, we will focus on the case wherein the particle response has both electric and magnetic components described by linearly-polarized collinear electric and magnetic dipoles $\mathbf{p}_e$ and $\mathbf{p}_m$. Without loss of generality, it is assumed in the following that similar to Sect. V.2.1 the oscillations are driven by some external excitation.

V.3.1 General case

Let us first consider the general case wherein the particle is described by arbitrary electric and magnetic dipoles $\mathbf{p}_e$ and $\mathbf{p}_m$ (our $\mathbf{p}_m$ is related to the standard magnetic dipole moment with units of $\mathrm{A}\times\mathrm{m}^2$ as $\mathbf{p}_m = \mu_0 \mathbf{m}$). Then, the time-averaged force can be written as [6, 37, 38]:

$$\mathscr{F} = \frac{1}{2}\mathrm{Re}\left\{\nabla\left[\mathbf{p}_g^* \cdot \mathbf{F}_{\mathrm{loc}}\right]\right\}_{\mathbf{r}=\mathbf{r}_0} - \frac{1}{12\pi}\frac{\omega^4}{c^3}\mathrm{Re}\left\{\mathbf{p}_e \times \mathbf{p}_m^*\right\}, \tag{5.9}$$

where $\mathbf{p}_g = \begin{pmatrix}\mathbf{p}_e & \mathbf{p}_m\end{pmatrix}^T$ and $\mathbf{F}_{\mathrm{loc}} = \begin{pmatrix}\mathbf{E}_{\mathrm{loc}} & \mathbf{H}_{\mathrm{loc}}\end{pmatrix}^T$ are six-vectors. As before, the subscript "loc" refers to the local fields. Similar to Sect. V.2.1, it is possible to decompose the local field as $\mathbf{F}_{\mathrm{loc}} = \mathbf{F}^{\mathrm{ext}} + \mathbf{F}^{\mathrm{s}}$ with $\mathbf{F}^{\mathrm{ext}} = \begin{pmatrix}\mathbf{E}^{\mathrm{ext}} & \mathbf{H}^{\mathrm{ext}}\end{pmatrix}^T$ the external field distribution and $\mathbf{F}^{\mathrm{s}} = \begin{pmatrix}\mathbf{E}^{\mathrm{s}} & \mathbf{H}^{\mathrm{s}}\end{pmatrix}^T$ the field back-scattered by the substrate due to the dipole radiation. Hence, for a composite dipole

the total force can be written as:

$$\mathscr{F} = \mathscr{F}^{\text{ext}} + \mathscr{F}^{\text{s}} + \mathscr{F}^{\text{self}}, \tag{5.10}$$

with $\mathscr{F}^{\text{ext}} = \frac{1}{2}\text{Re}\left\{\nabla\left[\mathbf{p}_g^* \cdot \mathbf{F}^{\text{ext}}\right]\right\}_{\mathbf{r}=\mathbf{r}_0}$, $\mathscr{F}^{\text{s}} = \frac{1}{2}\text{Re}\left\{\nabla\left[\mathbf{p}_g^* \cdot \mathbf{F}^{\text{s}}\right]\right\}_{\mathbf{r}=\mathbf{r}_0}$ and $\mathscr{F}^{\text{self}} = -\frac{1}{12\pi}\frac{\omega^4}{c^3}\text{Re}\left\{\mathbf{p}_e \times \mathbf{p}_m^*\right\}$

The component $\mathscr{F}^{\text{self}}$ can be nonzero even when the dipole stands alone in free-space due to the asymmetric radiation pattern of Huygens-type emitters [39].

As in Sect. V.2.1, we will focus on the $\mathscr{F}^{\text{s}}$ component of the force due to the radiation by the dipole. Evidently, the field back-scattered by the substrate $\mathbf{F}^{\text{s}}$ can be linked to the generalized dipole moment $\mathbf{p}_g$ through a 6×6 interaction dyadic $\mathbf{C}_g$ as $\mathbf{F}^{\text{s}}(\mathbf{r}) = \mathbf{C}_g(\mathbf{r}, \mathbf{r}_0) \cdot \mathbf{p}_g$. The interaction dyadic can be decomposed as

$$\mathbf{C}_g = \begin{pmatrix} \mathbf{C}_{\text{int}}^{\text{ee}} / \varepsilon_0 & \mathbf{C}_{\text{int}}^{\text{em}} c \\ \mathbf{C}_{\text{int}}^{\text{me}} c & \mathbf{C}_{\text{int}}^{\text{mm}} / \mu_0 \end{pmatrix} \tag{5.11}$$

with $\mathbf{C}_{\text{int}}^{\text{ij}}$ (*i,j=e,m*) being 3×3 tensors with dimensions of m^{-3}. The explicit formulas of $\mathbf{C}_{\text{int}}^{\text{ee}}$ (defined as in Sect. V.2.1) and $\mathbf{C}_{\text{int}}^{\text{mm}}$ can be found in Appendix A [Eqs. (5.A1b) and (5.A2b)]. The tensors with crossed indices can be found from the Maxwell equations (the composite dipole stands in air):

$$\mathbf{C}_{\text{int}}^{\text{me}} = \frac{1}{i(\omega/c)} \nabla \times \mathbf{C}_{\text{int}}^{\text{ee}}, \qquad \mathbf{C}_{\text{int}}^{\text{em}} = \frac{-1}{i(\omega/c)} \nabla \times \mathbf{C}_{\text{int}}^{\text{mm}}. \tag{5.12}$$

The force $\mathscr{F}^{\text{s}}$ is written is terms of $\mathbf{C}_g$ as follows:

$$\begin{aligned}\mathscr{F}_i^{\mathrm{s}} &= \frac{1}{2}\mathrm{Re}\left\{\mathbf{p}_g^* \cdot \left[\partial_i \mathbf{C}_g\right]_{\mathbf{r}=\mathbf{r}_0} \cdot \mathbf{p}_g\right\} \\ &= \frac{1}{2}\mathrm{Re}\left\{\mathbf{p}_e^* \cdot \frac{1}{\varepsilon_0}\partial_i \mathbf{C}_{\mathrm{int}}^{\mathrm{ee}} \cdot \mathbf{p}_e + \mathbf{p}_m^* \cdot \frac{1}{\mu_0}\partial_i \mathbf{C}_{\mathrm{int}}^{\mathrm{mm}} \cdot \mathbf{p}_m + c\mathbf{p}_e^* \cdot \partial_i \mathbf{C}_{\mathrm{int}}^{\mathrm{em}} \cdot \mathbf{p}_m + c\mathbf{p}_m^* \cdot \partial_i \mathbf{C}_{\mathrm{int}}^{\mathrm{me}} \cdot \mathbf{p}_e\right\}_{\mathbf{r}=\mathbf{r}_0}\end{aligned} \tag{5.13}$$

When the external driving field has zero gradient along the lateral direction of interest, the lateral force is completely determined by $\mathscr{F}^{\mathrm{s}} + \mathscr{F}^{\mathrm{self}}$.

V.3.2 Reciprocity constraints

The general form of the reciprocity theorem when the electromagnetic sources have both electric and magnetic components is [40]:

$$\int \mathbf{j}'' \cdot \boldsymbol{\sigma}_z \cdot \mathbf{F}' dV = \int \mathbf{j}' \cdot \boldsymbol{\sigma}_z \cdot \mathbf{F}'' dV \tag{5.14}$$

with $\mathbf{F} = \begin{pmatrix}\mathbf{E} & \mathbf{H}\end{pmatrix}^T$ the six-vector that determines the electromagnetic field, $\mathbf{j} = \begin{pmatrix}\mathbf{j}_e & \mathbf{j}_m\end{pmatrix}^T$ the six-vector formed by the electric and magnetic current densities and $\boldsymbol{\sigma}_z = \begin{pmatrix}\mathbf{1} & 0 \\ 0 & -\mathbf{1}\end{pmatrix}$ is a six-matrix. Thus, considering the distributions of fields ($\mathbf{F}', \mathbf{F}''$) created by the current distributions $\mathbf{j}' = -i\omega \mathbf{p}_g' \delta(\mathbf{r} - \mathbf{r}')$ and $\mathbf{j}'' = -i\omega \mathbf{p}_g'' \delta(\mathbf{r} - \mathbf{r}'')$ and proceeding as in Sect. V.2.2 it is possible to prove that:

$$\mathbf{p}_g'' \cdot \boldsymbol{\sigma}_z \cdot \mathbf{C}_g(\mathbf{r}'', \mathbf{r}') \cdot \mathbf{p}_g' = \mathbf{p}_g' \cdot \boldsymbol{\sigma}_z \cdot \mathbf{C}_g(\mathbf{r}', \mathbf{r}'') \cdot \mathbf{p}_g''. \tag{5.15}$$

Following the same steps as in Sect. V.2.2, still considering that the structure is invariant to translations along *x* and *y*, one may find that for arbitrary $\mathbf{p}_g'$, $\mathbf{p}_g''$ the following identity holds,

$$\mathbf{p}_g'' \cdot \boldsymbol{\sigma}_z \cdot \left[\partial_i \mathbf{C}_g\right]_{\mathbf{r}=\mathbf{r}_0} \cdot \mathbf{p}_g' = -\mathbf{p}_g' \cdot \boldsymbol{\sigma}_z \cdot \left[\partial_i \mathbf{C}_g\right]_{\mathbf{r}=\mathbf{r}_0} \cdot \mathbf{p}_g'', \qquad (i=x,y) \tag{5.16}$$

Picking $\mathbf{p}_g' = \mathbf{p}_g'' = \begin{pmatrix} \mathbf{p}_e & 0 \end{pmatrix}^T$ we see that $\mathbf{p}_e \cdot \frac{1}{\varepsilon_0} \partial_i \mathbf{C}_{\text{int}}^{\text{ee}} \cdot \mathbf{p}_e = 0$ and picking $\mathbf{p}_g' = \mathbf{p}_g'' = \begin{pmatrix} 0 & \mathbf{p}_m \end{pmatrix}^T$ we get $\mathbf{p}_m \cdot \frac{1}{\mu_0} \partial_i \mathbf{C}_{\text{int}}^{\text{mm}} \cdot \mathbf{p}_m = 0$. Furthermore, choosing $\mathbf{p}_g' = \begin{pmatrix} \mathbf{p}_e & 0 \end{pmatrix}^T$ and $\mathbf{p}_g'' = \begin{pmatrix} 0 & \mathbf{p}_m \end{pmatrix}^T$ one finds that $\mathbf{p}_m \cdot \partial_i \mathbf{C}_{\text{int}}^{\text{me}} \cdot \mathbf{p}_e = \mathbf{p}_e \cdot \partial_i \mathbf{C}_{\text{int}}^{\text{em}} \cdot \mathbf{p}_m$.

Let us now suppose that both the electric and magnetic dipoles are *linearly-polarized* so that $\mathbf{p}_e = |p_e| e^{i\phi_e} \hat{\mathbf{u}}_e$ and $\mathbf{p}_m = |p_m| e^{i\phi_m} \hat{\mathbf{u}}_m$ with the unit vectors $\hat{\mathbf{u}}_e, \hat{\mathbf{u}}_m$ real-valued. Using the reciprocity constraints derived in the previous paragraph in Eq. (5.13), it follows that, the lateral force $\mathscr{F}_i^{\text{s}}$ reduces to:

$$\mathscr{F}_i^{\text{s}} = \cos(\Delta) c |p_e| |p_m| \text{Re}\left\{ \hat{\mathbf{u}}_m \cdot \partial_i \mathbf{C}_{\text{int}}^{\text{me}} \cdot \hat{\mathbf{u}}_e \right\}_{\mathbf{r}=\mathbf{r}_0} \qquad \text{(lin. pol. dipoles)} \qquad (5.17)$$

with $\Delta = \phi_e - \phi_m$ the phase difference between the two dipole moments. Therefore, for a composite dipole the lateral force $\mathscr{F}_i^{\text{s}}$ may be nonzero, even when the dipoles are linearly polarized. The lateral force has maximal strength when the two dipoles oscillate in phase $(\Delta = 0)$ or in opposition of phase $(\Delta = 180^{\text{o}})$, and vanishes when they are in quadrature $(\Delta = \pm 90^{\text{o}})$.

V.3.3 Collinear linearly-polarized dipoles

The case of collinear dipoles ($\hat{\mathbf{u}}_e = \hat{\mathbf{u}}_m$) is particularly interesting because the corresponding self-force $\mathscr{F}^{\text{self}}$ vanishes. Thus, when the gradient of the external field along the lateral direction of interest is zero, the lateral force is fully determined by $\mathscr{F}^{\text{s}}$ [Eq. (5.17)]. Using $\mathbf{C}_{\text{int}}^{\text{me}} = \frac{1}{i(\omega/c)} \nabla \times \mathbf{C}_{\text{int}}^{\text{ee}}$ and Eq. (5.A1b) it is possible to obtain an explicit formula for the lateral

force, but it is a bit too cumbersome to show here. When both dipoles are perpendicular to the interface ($\hat{\mathbf{u}}_e = \hat{\mathbf{u}}_m = \hat{\mathbf{z}}$) and the composite particle is positioned at a distance *d* from the substrate we get:

$$\frac{\mathscr{F}_L^s}{\mathscr{F}_0} = \cos(\Delta)\,\mathrm{Re}\left\{\frac{d^4}{(2\pi)^2}\int\int dk_x dk_y \frac{1}{2}\frac{-\mathbf{k}_t}{(\omega/c)} e^{-\gamma_0 2d}\,(\hat{\mathbf{z}}\times\mathbf{k}_t)\cdot\mathbf{R}(\omega,k_x,k_y)\cdot\mathbf{k}_t\right\} \quad (5.18)$$

with $\mathscr{F}_0 = c|p_e||p_m|/d^4$ a normalizing factor with units of force (N), $\mathbf{R}(\omega,k_x,k_y)$ the reflection matrix for plane wave incidence, and $\mathbf{k}_t = k_x\hat{\mathbf{x}} + k_y\hat{\mathbf{y}}$ the transverse wave vector (see Appendix A).

V.3.4 Uniaxial dielectric substrate

To illustrate the possibilities, next we consider a composite particle formed by the superposition of two collinear linearly polarized electric and magnetic dipoles positioned at a distance d above the same uniaxial dielectric substrate as in Sect. V.2.2. For simplicity, we take the transverse permittivity of the uniaxial dielectric equal to $\varepsilon_{\parallel} = 1$ in all the simulations.

Even though the reciprocity constraints do not forbid a lateral force for a superposition of electric and magnetic dipoles, surprisingly, it turns out that the force component along the *x*–direction vanishes. Even more puzzling, we find that the lateral force can be non-zero along the *y*-direction. Figures 5.3a and 5.3b show how the *y*-component of the lateral optical force $\mathscr{F}_y^s$ varies with the normalized distance $d\omega/c$ and with the tilt angle of the optical axis α_0. As seen in Fig. 5.3a, the sign of the lateral force can be tuned by varying the height of the particle with respect to the substrate, so that the force can be either positive or negative. The lateral force

depends strongly on the value of $\varepsilon_{\alpha\alpha}$, and most notably its sign changes when $\varepsilon_{\alpha\alpha}$ crosses the point $\varepsilon_{\alpha\alpha}=-1$. Furthermore, the lateral force depends on the tilt angle of the substrate optical axis (Fig. 5.3b), and vanishes when the optical axis is either normal or parallel to the interface. The lateral force sign is locked to the tilt angle sign.

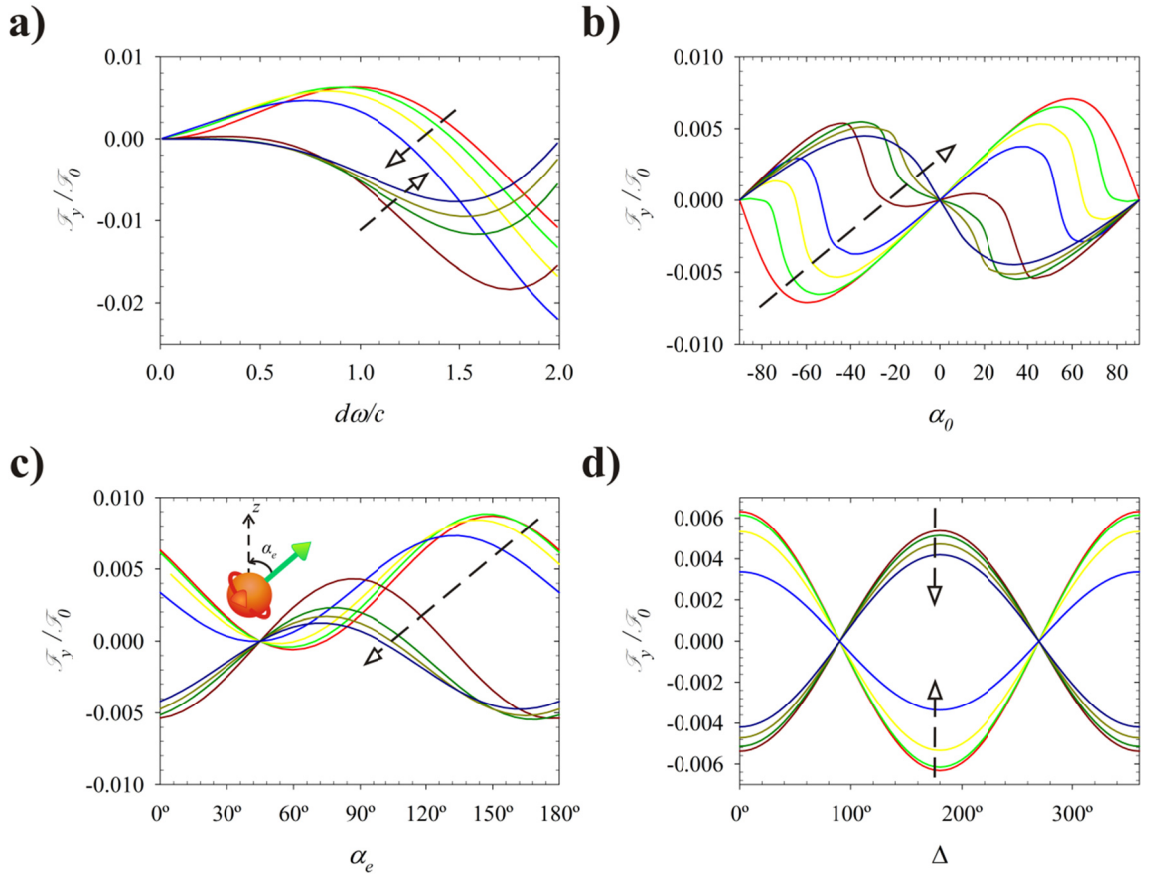

Figure 5.3: Plot of the (y-component of the) lateral force $\mathcal{F}_y^s$ for a uniaxial material with $\varepsilon_{\|}=1$ for $\varepsilon_{\alpha\alpha}=-10^6,-10,-4,-2,-0.5,-0.2,-0.1,-0.01$ (a) as a function of $d\omega/c$ for $\alpha_0=45^o$, $\alpha_m=\alpha_e=0$ and $\Delta=0^o$. (b) as function of the optical axis tilt angle α_0 for $d\omega/c=1$, $\alpha_m=\alpha_e=0$ and $\Delta=0^o$. (c) as a function of α_e with $\alpha_0=45^o$, $d\omega/c=1$, $\alpha_m=\alpha_e$ and $\Delta=0^o$. (d) as a function of Δ with $\alpha_0=45^o$, $d\omega/c=1$ and $\alpha_m=\alpha_e=0$. In all panels the arrow indicates the direction of increasing $\varepsilon_{\alpha\alpha}$ (from the red color towards the dark blue color).

Figure 5.3c illustrates how the lateral force varies with the orientation of the two collinear dipoles $\alpha_e=\alpha_m$ for the normalized distance $d\omega/c=1$ and for $\alpha_0=45^o$. Curiously, when $\varepsilon_{\|}=1$ as considered here, the lateral force vanishes when the dipole moment is parallel to the optical

axis direction $\alpha_e = \alpha_m = \alpha_0$. In agreement with Eq. (5.17), Fig. 5.3d shows that the lateral force depends on the phase difference, $\Delta = \phi_e - \phi_m$, between the two dipole moments, and has the largest value when the dipole moments are either in phase or in opposition of phase.

Hereafter, we consider the case where the two dipole moments are vertical ($\alpha_e = \alpha_m = 0$) and oscillate in phase ($\Delta = 0$). Furthermore, it is assumed that the normalized distance satisfies $d\omega / c = 1$, and that the substrate has $\alpha_0 = 45^{\circ}$ and $\varepsilon_{\alpha\alpha} = -\infty$ (extreme anisotropy, as in the wire medium), corresponding to a positive lateral force (Fig. 5.3) along the +*y*-direction.

Figure 5.4 shows a polar plot of the back-scattered electric field pattern $|\mathbf{E}^s|^2$ in the half-space $z > 0$ at one wavelength distance from the composite particle (red line). For the sake of completeness, we also show the back-scattered field patterns when the particle is a simple electric dipole (green line) or a simple magnetic dipole (blue line).

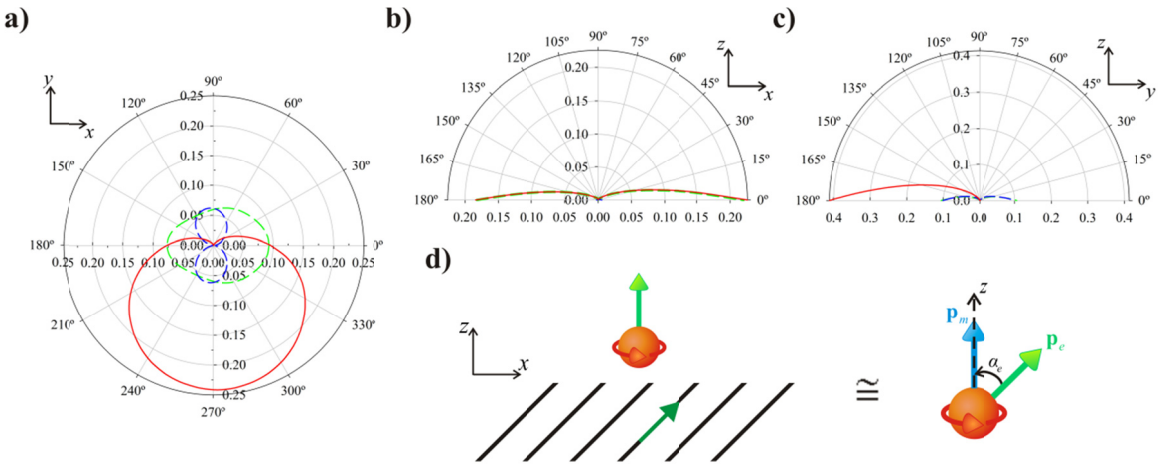

Figure 5.4: (a) Polar plot of the scattered field intensity ($|\mathbf{E}^s|^2$) (arbitrary normalization) in the $z = d$ plane calculated at the λ_0 - distance from the particle for $\alpha_0 = 45^{\circ}$ at the normalized distance $d\omega / c = 1$ for i) a single vertical electric dipole (green color), ii) single vertical magnetic dipole (blue color) and iii) vertical collinear electric and magnetic dipoles (red color). The amplitudes of the electric and magnetic dipoles are related as $p_e = (1/\eta_0)\, p_m$. (b) Same as (a) in the $y = 0$ plane. (c) Same as (a) in the $x = 0$ plane. (d) Two collinear electric and magnetic dipoles standing above a uniaxial substrate with tilted optical axes behave effectively as two non-collinear electric

and magnetic dipoles (Huygens source), leading to an asymmetric radiation pattern and a lateral recoil force.

The composite particle has a radiation pattern that is quasi-symmetric in the *y=0* plane (Fig. 5.4b). On the other hand, in the $x=0$ plane the radiation from the particle is strongly scattered to the negative *y* direction (Fig. 5.4c) as expected from the lateral force being positive ($\mathscr{F}_y^{\,s}>0$). This property is further highlighted in Fig. 5.4a, which shows that in the *xoy* plane the fields are scattered almost equally to the right and left but mainly to the negative *y* semi-plane. Figure 5.5 shows the near-field density plots of $\left|\mathbf{E}^s\right|^2$ in different cut-planes. In agreement with Fig. 5.4, the density plots are strongly asymmetric in the *yoz* plane.

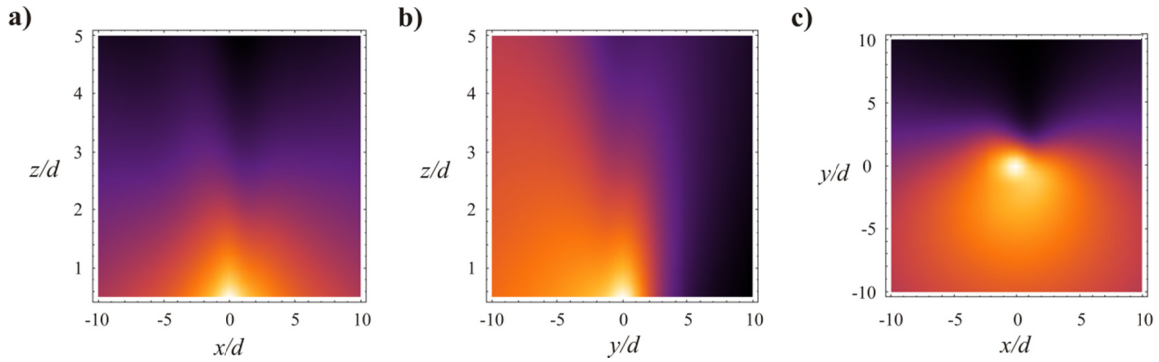

Figure 5.5: (a) Density plot of the scattered field intensity ($\left|\mathbf{E}^s\right|^2$) (in arbitrary units) at the xoz plane for a composite particle with $\mathbf{p}_e=(1/\eta_0)\,p_m\hat{\mathbf{z}}$ and $\mathbf{p}_m=p_m\hat{\mathbf{z}}$. The tilt angle is $\alpha_0=45^o$ and $d\omega/c=1$. (b) Same as (a) but in the yoz plane. (c) Same as (a) but in the $z=d$ plane.

To unveil the reason why the force is directed along *y*, it is convenient to visualize the uniaxial material as a tilted wire medium (Fig. 5.4d). In these conditions, when the two collinear (vertical) dipoles are placed above the substrate, they induce a current along the metallic wires. The combined effect of the dipoles and of the current induced along the wires is arguably analogous to a Huygens radiator with the effective electric and magnetic dipoles in the *xoz* plane (Fig. 5.4d). This elementary analogy explains in a simple manner why the radiation

pattern is strongly asymmetric along the *y*-direction, despite the structural symmetry of the substrate. A more sophisticated explanation is that the dipole-emitter is not invariant under the parity transformation $(x, y, z) \to (x, -y, z)$ because this transformation flips the magnetic dipole but not the electric dipole. This breach of symmetry explains the asymmetric radiation patterns along the *y*-direction.

V.5 Conclusions

In summary, we theoretically studied the lateral (recoil) forces acting on generic dipole type particles placed nearby a reciprocal translation-invariant substrate. It was shown that counter-intuitively the scattering from electric-dipoles above a smooth reciprocal planar substrate does not lead to recoil-type forces, even if the substrate is chiral or has tilted optical axes. A nontrivial lateral force can only be generated when the external field excitation has a gradient along a direction parallel to the interface.

We proposed a novel mechanism to create lateral forces using a composite dipolar particle formed by collinear linearly polarized electric and magnetic dipoles. We discussed in detail the physical mechanisms that enable the emergence of the anomalous recoil force when the composite particle stands above a uniaxial material with tilted optical axes, for example a wire medium. Our results may enable exotic optical manipulations and may find applications in particle sorting and delivery.

Appendix A: The back-scattered field

In this Appendix, we obtain the fields back-scattered by a material substrate for a dipole-

type excitation. We consider separately the cases of electric and magnetic dipoles. The fields radiated by a composite dipole (with electric and magnetic components) can be simply obtained using the superposition principle.

Electric dipole

Next, we characterize the fields radiated by an electric dipole that oscillates with frequency ω in air (region $z>0$) in the vicinity of a planar material structure (region $z<0$) (Fig. 5.1a). The electromagnetic fields in the $z>0$ region are the superposition of the field radiated by the dipole in free-space ($\mathbf{E}^{\text{self}}$) and the field back-scattered by the material slab ($\mathbf{E}^{\text{s}}$), $\mathbf{E}=\mathbf{E}^{\text{self}}+\mathbf{E}^{\text{s}}$. The self-electric field is given by $\mathbf{E}^{\text{self}}=\nabla\times\nabla\times\left(\frac{\mathbf{p}_e}{\varepsilon_0}\Phi_0\right)$ for $\mathbf{r}\neq\mathbf{r}_0$, where $\mathbf{r}_0=\left(x_0,y_0,z_0\right)$ determines the coordinates of the electric dipole, $\mathbf{p}_e$ is the electric dipole moment, $\Phi_0=\frac{e^{ik_0|\mathbf{r}-\mathbf{r}'|}}{4\pi|\mathbf{r}-\mathbf{r}'|}$ is the Hertz potential, and $k_0=\omega/c$ is the free-space wave number.

Let us consider the problem of plane wave incidence on the material slab with the incident wave propagating in the air region ($z>0$). Let $\mathbf{k}_t=k_x\hat{\mathbf{x}}+k_y\hat{\mathbf{y}}$ be the transverse (parallel to the interface) wave vector of the incident plane wave that determines the variation of the fields $\left(e^{i\mathbf{k}_t\cdot\mathbf{r}}\right)$ along the *x* and *y* directions. We introduce $\mathbf{R}=\mathbf{R}\left(\omega,k_x,k_y\right)$ as the (2×2) reflection matrix such that the transverse electric field ($\mathbf{E}_t^{\text{ref}}=E_x^{\text{ref}}\hat{\mathbf{x}}+E_y^{\text{ref}}\hat{\mathbf{y}}$) associated with the plane wave reflected on the material slab is related to the transverse electric field associated with the incident plane wave ($\mathbf{E}_t^{\text{inc}}=E_x^{\text{inc}}\hat{\mathbf{x}}+E_y^{\text{inc}}\hat{\mathbf{y}}$) as $\mathbf{E}_t^{\text{ref}}=\mathbf{R}\cdot\mathbf{E}_t^{\text{inc}}$.

Following Refs. [28-32, 40-42], the electric field back-scattered by the material slab, $\mathbf{E}^{\mathrm{s}}$, can be written in the air region in terms of $\mathbf{R}$ through a Sommerfeld-type integral:

$$\mathbf{E}^{\mathrm{s}}\left(\mathbf{r}\right)=\mathbf{C}_{\mathrm{int}}^{\mathrm{ee}}\cdot\mathbf{p}_{e}/\varepsilon_{0} \tag{5.A1a}$$

$$\begin{aligned}\mathbf{C}_{\mathrm{int}}^{\mathrm{ee}}\left(\mathbf{r},\mathbf{r}_{0}\right)=&\frac{1}{\left(2\pi\right)^{2}}\int\int dk_{x}dk_{y}\,\frac{1}{2\gamma_{0}}e^{-\gamma_{0}\left(z+z_{0}\right)}e^{ik_{x}\left(x-x_{0}\right)}e^{ik_{y}\left(y-y_{0}\right)}\times\\&\left(\mathbf{1}_{t}+\hat{\mathbf{z}}\otimes\frac{i\mathbf{k}_{t}}{\gamma_{0}}\right)\cdot\mathbf{R}\cdot\left(i\gamma_{0}\mathbf{k}_{t}\otimes\hat{\mathbf{z}}+k_{0}^{2}\mathbf{1}_{t}-\mathbf{k}_{t}\otimes\mathbf{k}_{t}\right)\end{aligned} \tag{5.A1b}$$

Here, $\gamma_{0}=-ik_{z0}$ with $k_{z0}=\sqrt{\omega^{2}/c^{2}-k_{x}^{2}-k_{y}^{2}}$ is the propagation constant in the air region and $\mathbf{1}_{t}=\hat{\mathbf{x}}\otimes\hat{\mathbf{x}}+\hat{\mathbf{y}}\otimes\hat{\mathbf{y}}$. Equation (5.A1) is completely general and applies to any planar substrate that is invariant to translations along the *x* and *y* directions. The magnetic field radiated by the electric dipole in the air region can be written as $\mathbf{H}=\mathbf{H}^{\mathrm{self}}+\mathbf{H}^{\mathrm{s}}$ with $\mathbf{H}^{i}=\frac{1}{i\omega\mu_{0}}\nabla\times\mathbf{E}^{i}$ (*i*=s, self).

Magnetic dipole

The fields radiated by a magnetic dipole (with dipole moment $\mathbf{p}_{m}$) can be easily found using "duality" arguments. Specifically, in the air region it is possible to write $\mathbf{H}=\mathbf{H}^{\mathrm{self}}+\mathbf{H}^{\mathrm{s}}$ with $\mathbf{H}^{\mathrm{self}}=\nabla\times\nabla\times\left(\frac{\mathbf{p}_{m}}{\mu_{0}}\Phi_{0}\right)$ for $\mathbf{r}\neq\mathbf{r}_{0}$ and $\mathbf{H}^{\mathrm{s}}$ given by

$$\mathbf{H}^{\mathrm{s}}\left(\mathbf{r}\right)=\mathbf{C}_{\mathrm{int}}^{\mathrm{mm}}\cdot\mathbf{p}_{m}/\mu_{0} \tag{5.A2a}$$

$$\mathbf{C}_{\text{int}}^{\text{mm}}\left(\mathbf{r},\mathbf{r}_0\right)=\frac{1}{\left(2\pi\right)^2}\int\int dk_x dk_y\,\frac{1}{2\gamma_0}e^{-\gamma_0\left(z+z_0\right)}e^{ik_x\left(x-x_0\right)}e^{ik_y\left(y-y_0\right)}\times \left(\mathbf{1}_t+\hat{\mathbf{z}}\otimes\frac{i\mathbf{k}_t}{\gamma_0}\right)\cdot\mathbf{R}^H\cdot\left(i\gamma_0\mathbf{k}_t\otimes\hat{\mathbf{z}}+k_0^2\mathbf{1}_t-\mathbf{k}_t\otimes\mathbf{k}_t\right) \tag{5.A2b}$$

Note that the tensor $\mathbf{C}_{\text{int}}^{\text{mm}}$ is defined in the same manner as the tensor $\mathbf{C}_{\text{int}}^{\text{ee}}$, except that the reflection coefficient matrix is different: $\mathbf{R}\rightarrow\mathbf{R}^H$. The reflection coefficient matrix $\mathbf{R}^H$ is such that for plane wave incidence the transverse components of the incident and reflected magnetic fields are linked as $\mathbf{H}_t^{\text{ref}}=\mathbf{R}^H\cdot\mathbf{H}_t^{\text{inc}}$. Using the Maxwell equations, it is straightforward to check that for a plane wave propagating in free-space the transverse electric and magnetic fields are related by:

$$\mathbf{E}_t^{\pm}=-\frac{\pm 1}{\omega\varepsilon_0 k_{z0}}\begin{pmatrix}-k_xk_y & -\left(k_y^2+k_{z0}^2\right)\\ k_x^2+k_{z0}^2 & k_xk_y\end{pmatrix}\cdot\mathbf{H}_t^{\pm}. \tag{5.A3}$$

The $\pm$ sign determines if the wave propagates towards +*z* or –*z* semispace. From this result it is straightforward to show that the reflection coefficient matrix for the magnetic field can be written as,

$$\mathbf{R}^H\left(\omega,k_x,k_y\right)=-\begin{pmatrix}-k_xk_y & -\left(k_y^2+k_{z0}^2\right)\\ k_x^2+k_{z0}^2 & k_xk_y\end{pmatrix}^{-1}\cdot\mathbf{R}\cdot\begin{pmatrix}-k_xk_y & -\left(k_y^2+k_{z0}^2\right)\\ k_x^2+k_{z0}^2 & k_xk_y\end{pmatrix}. \tag{5.A4}$$

In the air region, the electric field radiated by the magnetic dipole is given by $\mathbf{E}=\mathbf{E}^{\text{self}}+\mathbf{E}^{\text{s}}$ with $\mathbf{E}^i=-\frac{1}{i\omega\varepsilon_0}\nabla\times\mathbf{H}^i$ (*i*=s, self).

Appendix B: Reflection matrix for a uniaxial substrate with a tilted optical axis

Next, we derive the reflection matrix $\mathbf{R}$ (defined as in Appendix A) for the case in which the

region $z<0$ is a nonmagnetic uniaxial dielectric with optical axis directed along the unit vector $\hat{\boldsymbol{\alpha}}$. The relative permittivity of the uniaxial dielectric is of the form:

$$\boldsymbol{\varepsilon} = \varepsilon_{\parallel}\left(\mathbf{1}-\hat{\boldsymbol{\alpha}}\otimes\hat{\boldsymbol{\alpha}}\right)+\varepsilon_{\alpha\alpha}\hat{\boldsymbol{\alpha}}\otimes\hat{\boldsymbol{\alpha}}\,. \tag{5.B1}$$

Reflection matrix

Here, we obtain a general formula for $\mathbf{R}$ in terms of wave admittance matrices. We follow closely the ideas of Ref. [43, Ap. A], and define the transverse fields,

$$\mathbf{E}_t=\begin{pmatrix}E_x\\E_y\end{pmatrix} \qquad \text{and} \qquad \mathbf{J}\cdot\mathbf{H}_t=\begin{pmatrix}0&1\\-1&0\end{pmatrix}\begin{pmatrix}H_x\\H_y\end{pmatrix}=\begin{pmatrix}H_y\\-H_x\end{pmatrix}. \tag{5.B2}$$

For some generic bulk material, we introduce two admittance matrices, $\mathbf{Y}^{\pm}$, such that for plane waves propagating along the +*z* and –*z* directions with transverse wave vector $\mathbf{k}_t$, the corresponding transverse fields are related by,

$$\mathbf{J}\cdot\mathbf{H}_t^{+}=\mathbf{Y}^{+}\cdot\mathbf{E}_t^{+}, \qquad\qquad \mathbf{J}\cdot\mathbf{H}_t^{-}=-\mathbf{Y}^{-}\cdot\mathbf{E}_t^{-}. \tag{5.B3}$$

The matrices $\mathbf{Y}^{\pm}$ depend on the material (which can be totally arbitrary), on the frequency ω, and on the transverse wave vector $\mathbf{k}_t$. For an isotropic dielectric with permittivity ε, one easily finds that,

$$\mathbf{Y}^{+}\eta_0=\mathbf{Y}^{-}\eta_0=\frac{1}{k_0k_z^{+}}\begin{bmatrix}k_0^2\varepsilon-k_y^2 & k_xk_y\\ k_xk_y & k_0^2\varepsilon-k_x^2\end{bmatrix} \quad \text{(isotropic dielectric).} \tag{5.B4}$$

where $k_z^{+}=\sqrt{k_0^2\varepsilon-k_x^2-k_y^2}$, $k_0=\omega/c$ is the free-space wave number, and η_0 is the vacuum impedance.

The reflection coefficient matrix for an interface between air ($z>0$) and a uniaxial material

$(z<0)$ can be found by imposing the continuity of $\mathbf{E}_t$ and $\mathbf{J}\cdot\mathbf{H}_t$ at the interface. This procedure yields [43]:

$$\mathbf{R}\left(\omega,k_x,k_y\right)=\left(\mathbf{Y}_d+\mathbf{Y}_u^-\right)^{-1}\cdot\left(\mathbf{Y}_d-\mathbf{Y}_u^-\right). \tag{5.B5}$$

where $\mathbf{Y}_d=\mathbf{Y}_d^{\pm}$ is the admittance matrix of the air region [Eq. (5.B4)] with $\varepsilon=1$], and $\mathbf{Y}_u^-$ is the admittance matrix of the uniaxial medium. Note that in general the matrices $\mathbf{Y}_d$ and $\mathbf{Y}_u^-$ do not commute. In the next subsections, we obtain an explicit formula for $\mathbf{Y}_u^-$.

Admittance matrices

The admittance matrices $\mathbf{Y}^{\pm}\left(\omega,k_x,k_y\right)$ can be constructed from the plane wave modes of the bulk medium. Specifically, let $\left(\mathbf{E}_i^{\pm}\quad\mathbf{H}_i^{\pm}\right)$ (*i*=1,2) be the fields associated with the plane waves with a wave vector of the form $\mathbf{k}_i=\left(k_x,k_y,k_{z,i}^{\pm}\right)$ and $\frac{1}{2}\mathrm{Re}\left\{\mathbf{E}_i^{\pm}\times\mathbf{H}_i^{\pm,*}\right\}\cdot\left(\pm\hat{\mathbf{z}}\right)>0$ so that the energy flows towards the ±*z*-direction depending on the superscript. Then, from Eq. (5.B3) we can write:

$$\left[\mathbf{J}\cdot\mathbf{H}_{t,1}^{\pm}\quad\mathbf{J}\cdot\mathbf{H}_{t,2}^{\pm}\right]=\pm\mathbf{Y}^{\pm}\cdot\left[\mathbf{E}_{t,1}^{\pm}\quad\mathbf{E}_{t,2}^{\pm}\right]. \tag{5.B6}$$

where the subscript "t" indicates that only the transverse components are considered. Thereby, the admittance matrices are given by:

$$\mathbf{Y}^{\pm}=\pm\left[\mathbf{J}\cdot\mathbf{H}_{t,1}^{\pm}\quad\mathbf{J}\cdot\mathbf{H}_{t,2}^{\pm}\right]\cdot\left[\mathbf{E}_{t,1}^{\pm}\quad\mathbf{E}_{t,2}^{\pm}\right]^{-1} \tag{5.B7}$$

For nonmagnetic structures, the plane wave fields satisfy $\mathbf{H}=\frac{1}{\omega\mu_0}\mathbf{k}\times\mathbf{E}$. Using this property it

is possible to show that,

$$\mathbf{Y}^{+}\eta_0 = \frac{1}{k_0}\frac{1}{\left(\mathbf{E}_1^{+}\times\mathbf{E}_2^{+}\right)\cdot\hat{\mathbf{z}}}\begin{bmatrix}\mathbf{E}_1^{+}\cdot\left[\hat{\mathbf{y}}\left(\mathbf{k}_2^{+}\times\hat{\mathbf{y}}\right)-\left(\mathbf{k}_1^{+}\times\hat{\mathbf{y}}\right)\hat{\mathbf{y}}\right]\cdot\mathbf{E}_2^{+} & \mathbf{E}_1^{+}\cdot\left[\left(\mathbf{k}_1^{+}\times\hat{\mathbf{y}}\right)\hat{\mathbf{x}}-\hat{\mathbf{x}}\left(\mathbf{k}_2^{+}\times\hat{\mathbf{y}}\right)\right]\cdot\mathbf{E}_2^{+}\\ \mathbf{E}_1^{+}\cdot\left[\left(\mathbf{k}_1^{+}\times\hat{\mathbf{x}}\right)\hat{\mathbf{y}}-\hat{\mathbf{y}}\left(\mathbf{k}_2^{+}\times\hat{\mathbf{x}}\right)\right]\cdot\mathbf{E}_2^{+} & \mathbf{E}_1^{+}\cdot\left[\hat{\mathbf{x}}\left(\mathbf{k}_2^{+}\times\hat{\mathbf{x}}\right)-\left(\mathbf{k}_1^{+}\times\hat{\mathbf{x}}\right)\hat{\mathbf{x}}\right]\cdot\mathbf{E}_2^{+}\end{bmatrix} \quad (5.B8a)$$

A similar formula is obtained for $\mathbf{Y}^{-}$ with a minus sign in front of the right-hand side expression and with $\mathbf{E}_i^{+}$ (the waves that propagate along *+z*) replaced by $\mathbf{E}_i^{-}$ (the waves that propagate along *–z*):

$$\mathbf{Y}^{-}\eta_0 = -\frac{1}{k_0}\frac{1}{\left(\mathbf{E}_1^{-}\times\mathbf{E}_2^{-}\right)\cdot\hat{\mathbf{z}}}\begin{bmatrix}\mathbf{E}_1^{-}\cdot\left[\hat{\mathbf{y}}\left(\mathbf{k}_2^{-}\times\hat{\mathbf{y}}\right)-\left(\mathbf{k}_1^{-}\times\hat{\mathbf{y}}\right)\hat{\mathbf{y}}\right]\cdot\mathbf{E}_2^{-} & \mathbf{E}_1^{-}\cdot\left[\left(\mathbf{k}_1^{-}\times\hat{\mathbf{y}}\right)\hat{\mathbf{x}}-\hat{\mathbf{x}}\left(\mathbf{k}_2^{-}\times\hat{\mathbf{y}}\right)\right]\cdot\mathbf{E}_2^{-}\\ \mathbf{E}_1^{-}\cdot\left[\left(\mathbf{k}_1^{-}\times\hat{\mathbf{x}}\right)\hat{\mathbf{y}}-\hat{\mathbf{y}}\left(\mathbf{k}_2^{-}\times\hat{\mathbf{x}}\right)\right]\cdot\mathbf{E}_2^{-} & \mathbf{E}_1^{-}\cdot\left[\hat{\mathbf{x}}\left(\mathbf{k}_2^{-}\times\hat{\mathbf{x}}\right)-\left(\mathbf{k}_1^{-}\times\hat{\mathbf{x}}\right)\hat{\mathbf{x}}\right]\cdot\mathbf{E}_2^{-}\end{bmatrix} \quad (5.B8b)$$

When the medium is either reciprocal or invariant under a parity transformation ($\mathbf{r}\rightarrow-\mathbf{r}$), the admittance matrices have the symmetries discussed in Ref. [43].

Uniaxial dielectric

Let us now focus on uniaxial dielectrics with relative permittivity tensor as in Eq. (5.B1). In this case, the relevant plane waves are the usual ordinary ($\mathbf{E}_1$) and extraordinary ($\mathbf{E}_2$) waves, with electric field of the form (apart from an arbitrary multiplication factor):

$$\mathbf{E}_1 = \mathbf{k}_1\times\hat{\boldsymbol{\alpha}}, \qquad \mathbf{k}_1\equiv\mathbf{k}_O, \quad (5.B9a)$$

$$\mathbf{E}_2 = \boldsymbol{\varepsilon}^{-1}\cdot\left[\mathbf{k}_2\times\left(\mathbf{k}_2\times\hat{\boldsymbol{\alpha}}\right)\right] = \frac{\left(\mathbf{k}_2\cdot\hat{\boldsymbol{\alpha}}\right)}{\varepsilon_{\parallel}}\mathbf{k}_2-\hat{\boldsymbol{\alpha}}\frac{\omega^2}{c^2}, \mathbf{k}_2\equiv\mathbf{k}_E. \quad (5.B9b)$$

The ordinary wave satisfies the dispersion equation:

$$\mathbf{k}_O\cdot\mathbf{k}_O = \left(\frac{\omega}{c}\right)^2\varepsilon_{\parallel}, \quad (5.B10a)$$

while the extraordinary wave satisfies,

$$\frac{1}{\varepsilon_{\|}}\left(\mathbf{k}_E\cdot\hat{\boldsymbol{\alpha}}\right)^2+\frac{1}{\varepsilon_{\alpha\alpha}}\left[\left(\mathbf{k}_E\cdot\mathbf{k}_E\right)-\left(\mathbf{k}_E\cdot\hat{\boldsymbol{\alpha}}\right)^2\right]=\left(\frac{\omega}{c}\right)^2. \tag{5.B10b}$$

The second identity in Eq. (5.B9b) is obtained with the help of Eq. (5.B10b). The wave vectors of the ordinary and extraordinary waves are the form:

$$\mathbf{k}_O=k_x\hat{\mathbf{x}}+k_y\hat{\mathbf{y}}+k_{O,z}\hat{\mathbf{z}}, \qquad \mathbf{k}_E=k_x\hat{\mathbf{x}}+k_y\hat{\mathbf{y}}+k_{E,z}\hat{\mathbf{z}} \tag{5.B11}$$

with the *z*-component of the wave vectors determined by Eqs. (5.B10a) and (5.B10b), respectively. Straightforward calculations show that:

$$k_{O,z}=\pm\sqrt{\left(\frac{\omega}{c}\right)^2\varepsilon_{\|}-k_x^2-k_y^2} \tag{5.B12a}$$

$$k_{E,z}=\frac{1}{\varepsilon_{\|}+\left(\hat{\mathbf{z}}\cdot\hat{\boldsymbol{\alpha}}\right)^2\left(\varepsilon_{\alpha\alpha}-\varepsilon_{\|}\right)}\Bigg[-\left(\varepsilon_{\alpha\alpha}-\varepsilon_{\|}\right)\left(\mathbf{k}_t\cdot\hat{\boldsymbol{\alpha}}\right)\left(\hat{\mathbf{z}}\cdot\hat{\boldsymbol{\alpha}}\right)$$
$$\pm\left[\left(\left(\varepsilon_{\alpha\alpha}-\varepsilon_{\|}\right)\left(\mathbf{k}_t\cdot\hat{\boldsymbol{\alpha}}\right)\left(\hat{\mathbf{z}}\cdot\hat{\boldsymbol{\alpha}}\right)\right)^2+\left(\frac{\omega^2}{c^2}\varepsilon_{\alpha\alpha}\varepsilon_{\|}-\varepsilon_{\|}k_t^2+\left(\mathbf{k}_t\cdot\hat{\boldsymbol{\alpha}}\right)^2\left(\varepsilon_{\|}-\varepsilon_{\alpha\alpha}\right)\right)\left(\varepsilon_{\|}+\left(\hat{\mathbf{z}}\cdot\hat{\boldsymbol{\alpha}}\right)^2\left(\varepsilon_{\alpha\alpha}-\varepsilon_{\|}\right)\right)\right]^{1/2}\Bigg] \tag{5.B12b}$$

with $\mathbf{k}_t=k_x\hat{\mathbf{x}}+k_y\hat{\mathbf{y}}$ the transverse (parallel to the interface with air) wave vector. The $\pm$ sign is chosen depending on the desired propagation direction ($\pm z$). In particular, the matrix $\mathbf{Y}_u^-$ is calculated using Eq. (5.B8b) with $\mathbf{E}_i^-$ defined as in Eq. (5.B9) with the wave vectors determined by Eq. (5.B12) with the "$-$" sign.

References

[1] A. Ashkin, "Acceleration and Trapping of Particles by Radiation Pressure", *Phys. Rev. Lett.,* **24**, 4, 156, 1970.

[2] S. Chu, "Nobel Lecture: The manipulation of neutral particles", *Rev. Mod. Phys.,* **70**, 3, 685,

1998.

[3] M. M. Wang, E. Tu, D. E. Raymond, J. M. Yang, H. Zhang, N. Hagen, B. Dees, E. M. Mercer, A. H. Forster, I. Kariv, P. J Marchand, and W. F. Butler, "Microfluidic sorting of mammalian cells by optical force switching", *Nat. Biotechnol*., **23**, 83, 2005.

[4] W. D. Phillips, "Laser cooling and trapping of neutral atoms", *Rev. Mod. Phys.*, **70**, 3, 721–741, 1998.

[5] D. E. Fernandes, M. G. Silveirinha, "Optical Tractor Beam with Chiral Light", *Phys. Rev. A*, **91**, 061801(R), 2015.

[6] D. E. Fernandes and M. G. Silveirinha, "Single-Beam Optical Conveyor Belt for Chiral Particles", *Phys. Rev. A*, **6**, 014016, 2016.

[7] M. Dienerowitz, M. Mazilu and K. Dholakia, "Optical manipulation of nanoparticles: a review", *J. Nanophoton.*, **2**, 021875, 2008.

[8] A. Ashkin, J. M. Dziedzic, J. E. Bjorkholm, and S. Chu, "Observation of a single-beam gradient force optical trap for dielectric particles", *Opt. Lett.* **11**, 288–290, 1986.

[9] A. Ashkin, "Optical trapping and manipulation of neutral particles using lasers", *PNAS*, **13**, 94 (10) 4853-4860, 1997.

[10] D. G. Grier, "A revolution in optical manipulation", *Nature*, **424**, 810–816, 2003.

[11] A. Ivinskaya, M. I. Petrov, A. A. Bogdanov, I. Shishkin, P. Ginzburg and A. S. Shalin, "Plasmon-assisted optical trapping and anti-trapping", *Light: Science & Applications*, **6**, 1-6, 2017.

[12] M. I. Petrov, S. V. Sukhov, A. A. Bogdanov, A. S. Shalin, and A. Dogariu, "Surface plasmon polariton assisted optical pulling force", *Laser Photonics Rev.*, **10**, 1, 116–122, 2016.

[13] A. Ivinskaya, N. Kostina, M. I. Petrov, A. A. Bogdanov, S. Sukhov, A. S. Shalin, and P. Ginzburg, "Optical pulling forces, mediated by hyperbolic metasurfaces", submitted to ACS Photonics.

[14] N. Kostina, A. Ivinskaya, S. Sukhov, A. Bogdanov, I. Toftul, M. Nieto-Vesperinas, P. Ginzburg, M.Petrov, and A. Shalin, "Optical binding via surface plasmon polariton interference", arXiv:1708.05471.

[15] H. B. G. Casimir, and D. Polder, "The Influence of Retardation on the London-van der Waals Forces", *Phys. Rev.*, **73**, 4, 360, 1948.

[16] H. B. G. Casimir, "Sur les forces van der Waals-London", *J. Chim. Phys.*, **46**, 407-410, 1949.

[17] S. K. Lamoreaux, "Casimir forces: still surprising after 60 years", *Physics today*, **60**, 2, 40,

2007.

[18] S. Y. Buhmann, L. Knoll, and D.-G. Welsch, H. T. Dung, "Casimir-Polder forces: A nonperturbative approach", *Phys. Rev. A,* **70**, 052117, 2004.

[19] S. Scheel, S.Y. Buhmann, C. Clausen, and P. Schneeweiss, "Directional spontaneous emission and lateral Casimir-Polder force on an atom close to a nanofiber", *Phys. Rev. A*, **92**, 043819, 2015.

[20] F. J. Rodriguez-Fortuño, G. Marino, P. Ginzburg, D. O'Connor, A. Martinez, G. A. Wurtz, A. V. Zayats, "Near Field Interference for the Unidirectional Excitation of Electromagnetic Guided Modes", *Science*, **340**, 6130, 328, 2013.

[21] F. J. Rodriguez-Fortuño, N. Engheta, A. Martinez, A. V. Zayats, "Lateral forces on circularly polarizable particles near a surface", *Nat. Commun.*, **6**, 8799, 2015.

[22] A. Hayat, J. P. B. Mueller and F. Capasso, "Lateral chirality-sorting optical forces", *PNAS*, **112** (43) 13190-13194, 2015.

[23] S. B. Wang and C. T. Chan, "Lateral optical force on chiral particles near a surface", *Nat. Commun.*, **5**, 3307, 2014.

[24] I. S. Sinev, A. A. Bogdanov, F. E. Komissarenko, k. S. Frizyuk, M. I. Petrov, I. S. Mukhin, S. V. Makarov, A. K. Samusev, A. V. Lavrinenko and I. V. Iorsh, "Chirality driven by magnetic dipole response for demultiplexing of surface waves", *Laser Photonics Rev.*, **11**, 1700168, 2017.

[25] A. Manjavacas, F. J. Rodríguez-Fortuño, F. J. García de Abajo, and A. V. Zayats, "Lateral Casimir Force on a Rotating Particle near a Planar Surface", *Phys. Rev. Lett.*, **118**, 133605, 2017.

[26] F. L. Kien and A. Rauschenbeutel, "Spontaneous emission of a two-level atom with an arbitrarily polarized electric dipole in front of a flat dielectric surface", *Phys. Rev. A*, **93**, 043828, 2016.

[27] S. Lannebere, M. G. Silveirinha, "Negative spontaneous emission by a moving two-level atom", *J. Opt.,* **19**, 014004, 2017.

[28] M. G. Silveirinha, S. A. H. Gangaraj, G. W. Hanson, M. Antezza, "Fluctuation-induced forces on an atom near a photonic topological material", *Phys. Rev. A*, **97**, 022509, 2018.

[29] S. A. H. Gangaraj, G. W. Hanson, M. Antezza, M. G. Silveirinha, "Spontaneous lateral atomic recoil force close to a photonic topological material", *Phys. Rev. B*, **97**, 201108(R), 2018.

[30] R. R. Q. P. T. O. Weernink, P. Barcellona, S. Y. Buhmann, "Lateral Casimir-Polder forces by breaking time-reversal symmetry", *Phys. Rev. A*, **97**, 032507, 2018.

[31] K. Y. Bliokh, F. J. Rodriguez-Fortuño, F. Nori, and A. V. Zayats, "Spin-orbit interactions of

light", *Nat. Photon.,* **9**, 796, 2015.

[32] I. S. Nefedov and J. M. Rubi, "Lateral-drag propulsion forces induced by anisotropy", *Sci. Rep.*, **7**, 6155, 2017.

[33] M. G. Silveirinha, C. A. Fernandes, J. R. Costa, "Additional Boundary Condition for a Wire Medium Connected to a Metallic Surface", *New J. Phys.*, **10**, 053011(1-17), 2008.

[34] T. A. Morgado and M. G. Silveirinha "Transport of an arbitrary near-field component with an array of tilted wires", *New J. Phys.*, **11**, 083023, 2009.

[35] T. A. Morgado, J. S. Marcos, M. G. Silveirinha, S. I. Maslovski, "Experimental verification of full reconstruction of the near-field with a metamaterial lens", *Appl. Phys. Lett.*, **97**, 144102, 2010.

[36] H. Latioui, M. G. Silveirinha, "Near-field transport by a bent multi-wire endoscope". *J. Appl. Phys.* **120**, 063103, 2016.

[37] M. Nieto-Vesperinas, J. J. Sáenz, R. Gómez-Medina, and L. Chantada, "Optical forces on small magnetodielectric particles"*, Opt. Express*, **18**, 11, 11428-11443, 2010.

[38] P. C. Chaumet and A. Rahmani, "Electromagnetic force and torque on magnetic and negative-index scatterers"*, Opt. Express*, **17**, 4, 2224-2234, 2009.

[39] P. Jin, R. W. Ziolkowski, "Metamaterial-inspired, electrically small Huygens sources", *IEEE Antennas and Wireless Prop. Lett.*, **9**, 501, 2010.

[40] S. A. H. Gangaraj, M. G. Silveirinha, G. W. Hanson, "Berry Phase, Berry Connection, and Chern Number for a Continuum Bianisotropic Material From a Classical Electromagnetics Perspective", *IEEE J. Multiscale and Multiphysics. Comput. Techn*, **2**, 3-17, 2017.

[41] M. F. Picardi, A. V. Zayats, and F. J. Rodríguez-Fortuño, "Janus and Huygens Dipoles: Near-Field Directionality Beyond Spin-Momentum Locking", *Phys. Rev. Lett.*, **120**, 117402, 2018.

[42] M. G. Silveirinha, "Optical Instabilities and Spontaneous Light Emission by Polarizable Moving Matter"*, Phys. Rev. X,* **4**, 031013, 2014.

[43] T. A. Morgado and M. G. Silveirinha, "Single-interface Casimir torque", *New J. Phys.*, **18**, 103030, 2016.

CHAPTER 6 : Conclusions

VI. Conclusions

Main Achievements and Contributions Statement

In this thesis, I studied novel exotic phenomena related to wire metamaterials, with potential applications in medical imaging, sensing and optical manipulation of small particles. I presented a detailed analytical and numerical investigation of the relevant electromagnetic problems. A brief summary of the main results is presented next.

In chapter II, I showed that wire metamaterials can be used in medical imaging applications, e.g. as endoscopes. I developed a theoretical approach to characterize the scattering by a bent wire medium slab and derived novel additional boundary conditions required to solve the scattering problem. My research extends the results of several previous works to the case of bent wires, and proves that in general the wire medium is quite tolerant to the effect of bending in the context of near field transport based on the canalization principle, assuming a good ohmic contact at the bent interface. I presented full wave simulations of realistic multi-wire endoscopes with finite number of wires. The results confirm their robustness to the effect of bending and the possibility of near-field transport with subwavelength resolution.

In chapter III, I predicted the counterintuitive effect of light tunneling through two interlaced wire networks. I developed a theoretical model for the wave scattering problem based on an effective medium theory that models the interlaced wire medium as a spatially dispersive continuum. The light tunneling anomaly was interpreted as due to the destructive interference of the scattering by two interlaced 3D wire meshes and is rooted in a subradiant Fano-type resonance. I highlighted that a structural asymmetry of the metamaterial is a

mandatory condition in order to have such an effect.

In chapter IV, I investigated a “two phase topological metamaterial”, formed by a mixture of two topologically distinct material phases. It was shown that the metamaterial becomes transparent in a spectral range wherein the individual material phases are completely impenetrable by light. I proposed a wire metamaterial formed by metallic wires embedded in a magnetized plasma as a realistic implementation of the suggested system. Detailed numerical simulations show that the metamaterial enables an anomalous wave tunneling at extremely low frequencies. Furthermore, I suggested that magnetically-biased intrinsic semiconductors may also be regarded as two-phase topological materials.

In chapter V, I explored a new mechanism to optically manipulate linearly-polarized particles with nontrivial electric and magnetic responses. In a first stage, I showed that for linearly-polarized electric dipoles and a reciprocal substrate the lateral optical force invariably vanishes, independent of the anisotropy or chirality of the substrate. I theoretically demonstrated that when a linearly polarized particle with electric and magnetic responses stands above a uniaxial dielectric half-space with tilted optical axes, e.g. a tilted wire medium, it may experience a recoil force directed along the direction perpendicular to the interface normal and to the optical axis. My findings have applications in the optical manipulation of linearly polarized particles, for example in optical sorting and optical delivery.